Rational Design of Silicon-Carbon Composite Anode Materials for Lithium Ion Batteries

Yeonguk Son

Department of Energy Engineering

(Battery Science and Technology)

Graduate School of UNIST

2018

Rational Design of Silicon-Carbon Composite Anode Materials for Lithium Ion Batteries

Yeonguk Son

Department of Energy Engineering
(Battery Science and Technology)

Graduate School of UNIST

Rational Design of Silicon-Carbon Composite Anode Materials for Lithium Ion Batteries

A thesis/dissertation
submitted to the Graduate School of UNIST
in partial fulfillment of the
requirements for the degree of
Doctor of Philosophy in Energy Engineering

Yeonguk Son

6. 11. 2018
Approved by

Advisor
Jaephil Cho

Rational Design of Silicon-Carbon Composite Anode Materials for Lithium Ion Batteries

Yeonguk Son

This certifies that the thesis/dissertation of Yeonguk Son is approved.

6. 11. 2018

Advisor: Jaephil Cho

Youngsik Kim

Nam-Soon Choi

Seok Ju Kang

Hyun-Wook Lee

Abstract

Si dominant anode has been considered as a promising anode material for next levels of lithium ion batteries because of its high theoretical gravimetric capacity (3579 mAh/g). Specifically, increasing areal and volumetric capacity with commercial graphite anode is limited nowadays, but if Si is used for anode materials, there could be potentially solution for higher energy density of LIBs. However, Si anode suffers large volume expansion during lithiation. This large volume expansion could induce diverse fading mechanism in Si anode. Firstly, the volume expansion could induce physical loss of Si materials from electrode. Secondly, continuous SEI formation caused by the volume expansion could induce electrochemically isolated Si materials, which id dead particles. Therefore, the strategies alleviating Si volume expansion technologies should be developed. There have been numerous reported strategies such as size control, surface coating, active/inactive alloy, void space engineering, and composite. However, electrochemical performances of reported publications are not sufficient to accelerate extensive usage of Si materials in LIBs industry. In this context, herein my thesis will provide characterization methods and physical/chemical properties of Si dominant anode and present customized strategies for 650 mAh/g and 1200 mAh/g of Si dominant anode. Moreover, expected challenges of future anode materials will be discussed.

In chapter 1, demands and principles of LIBs, fair comparison of future anode materials; Si and Li metal anode, properties of Si anode, and reported strategies for Si anode will be considered. In following chapter 2 and 3, rational strategies for for 650 mAh/g and 1200 mAh/g of Si dominant anode will be introduced. In final chapter 4, potential challenges and perspetives of future anode materials will be discussed. I believe this thesis will be of benefit to researchers working on Si and future anode materials and I hope that the development of anode materials will advance the date to use lithium ion batteries with higher energy and power density.

Blank page

Contents

List of figures

1 and 2 representing low resident Li extent on SEI layer after long-term cycling.

Figure 10. Recent progress of investigating phase transformation on Si dominant anode (A) Lithiation extent into Si and phase transformation of Si during lithiation (a) Chemical element STEM-EELS mapping of Si anode after 10th lithiation. (b) crystalline change of Si via STEM-EELS mapping. (B) Persisted Li in LixSi after delithiation, the scattering length density graphs after (a) 2nd charge and (b) 2nd discharge and the x axis is distance from the interface (c-Si (green), the electrolyte (yellow), surface lithiation (red/dark-red), and deep lithiation (red-yellow)).

Figure 11. Representatives of the size control strategy (a-e: silicon nanofilm, and f, g: silicon nanowire). (a) TEM image and electron diffraction pattern of silicon nanocrystals. (b) high-resolution TEM image of silicon nanocrystal. (c) TEM image and electron diffraction pattern of silicon nanofilm. (d) TEM cross section image of silicon nanofilm. (e) half-cell cycle performance of silicon nanocrystals and nanofilm with theoretical capacity of graphite and experimental reference result of bulk silicon. (f) SEM images of pristine silicon nanowires. (g) half-cell cycling performance of silicon nanowire (Si NW) and silicon nanocrystal (Si NC) with theoretical capacity of graphite

Figure 12. Representatives of the surface coating strategy (a-d: silicon carbide free graphene coating, and e-h: graphene cage coating). (a) TEM image of Graphene coated Si NP (Gr-Si). The line profiles from the two red boxes indicate that the interlayer spacing between graphene layers is ~ 3.4 Å. (b) magnified TEM image of graphene layers visualizing the origins (red arrows) from which individual they grow. (c) A schematic illustration showing the sliding process of the graphene coating layers that can buffer the volume expansion of Si. (d) Half-cell cycling performance of Gr-Si depending on the weight ratio of graphene. (e) SEM image of a graphene-encapsulated Si microparticle (SiMP@Gr). (f) TEM image of an individual particle of SiMP@Gr. (g) High-resolution TEM image of the graphene cage's layered structure. The intensity plot shows that ten layers span a distance of 3.34nm (average inter-layer distance: 0.334 nm).

Figure 13. Representative of the active/inactive alloy strategy. (a-d: Fe-Cu-Si ternary composite). (a) SEM image of FeCuSi. (b) Magnified cross-sectional SEM image of FeCuSi. (c) HAADF-STEM image and EDS mapping of FeCuSi in cross sectional view. (d) Half-cell cycling performance of FeCuSi with C-SiO and $FeSi_2$ references.

Figure 14. Representatives of the void space engineering strategy. (a-h: silicon nanotubes and i-k: yolk-shell structures). (a) SEM images of Si nanotubes. (b) Top view SEM images of Si nanotubes. (c) Side view SEM images of Si nanotubes. (d) TEM images of Si nanotubes (e) Half-cell voltage profiles of Si nanotubes anode from 0.2 to 5C. (f) Half-cell voltage profiles of Si nanotubes anode after 2nd, 40th, and 80th cycle. (g) Full-cell voltage profiles of Si nanotubes anode from 0.2 to 5C. (h) Full-cell cycling performance of Si nanotubes anode at 1C (cathode

List of tables

Chapter 1

Introduction of anode materials for lithium ion batteries

1.1 Demands of energy storages

Human beings live in a rapidly changing society, and as a result human life patterns are constantly changing. It is the development of science and technology that has led these changes. In 1876, Bell developed a phone that allows us to talk to people who are far away, and James Watt's steam engine, developed in 1765, allowed us to travel long distances. These developments have had a profound impact on human life. In the past, the direction of such science and technology development was focused to make things that were not able to possible, and now sustainable development is also considered important. In other words, another challenge in the development of science and technology is to give our descendants the clean earth.

Most of the world's energy production currently takes place through the combustion of fossil fuels and continued use of fossil fuels will bring fueling exhaustion and serious environmental pollution. Therefore, the world faces the problem of alternative energy development. The possible candidates are wind, solar and geothermal energy resources. Since these resources produce energy intermittently depending on influences of environmental factors, the importance of energy storage devices is emerging.

The most widely used energy storage device is lithium ion battery (LIB) because it has high energy density and no memory effect, and there is little self-discharge [1-3]. Almost all mobile and smart phone batteries are LIB and it is also the most promising candidate for energy storage of electrical vehicles and Energy Storage System (ESS) applications. However, we feel the battery capacity shortage during smartphone use time, and the moving distance is not enough for an electric car to replace the internal combustion engine car. Therefore, people are demanding the energy storage devices having higher energy density.

Sodium ion battery or metal-air battery are being developed as next-generation energy storage devices [4-8]. However, the energy density of sodium ion batteries is challenging to exceed that of LIBs, and there are too many technical obstacles to overcome for commercialization of metal-air batteries such as depth of discharge and cost of noble metal electrocatalysts. In this regard, the most likely way to bring about an increase in energy density is on the development of new electrode materials for LIBs, such as nickel and lithium rich and sulfur cathode materials and silicon and lithium metal anode materials. These candidates for next electrode materials of LIBs

have been studying extensively and have been used in some cutting edge batteries with tiny quantities because of rapid capacity fading. Therefore, it is necessary to develop a technology capable of maintaining a high energy density for long-term cycles even in electrodes only composed with these new materials.

1.2 Principle of lithium ion batteries

Basic Principle

The electrical energy is stored via redox reactions on **cathode** and **anode** parts. The reason why LIBs can have a high energy density is because the weight of Li ions which act as charge carriers is light and the host material can store large amounts of Li ions. In order to increase the energy density of LIB, it is necessary to increase the capacity of the host materials which receive Li ions. The **electrolyte** provides ionic path way between cathode and anode materials. Due to Li ion flow between cathode and anode, electron flow in external circuit occurs to maintain charge balance. Hence, electrons should not flow between the anode and the cathode through electrolyte, and this role is provided by the **separator**. The four main components of LIB are cathode, anode, separator, and electrolyte as shown in figure 1.

Cathode

In charge process, oxidation reaction takes place on cathode. For example; $LiCoO_2 \rightarrow xLi^+ + xe^- + Li_{1-x}CoO_2$. Here the produced electrons are transferred to the anode through external circuit and the produced Li ions are transferred to the anode through the electrolyte. In discharge process, the opposite directional reaction takes place on cathode. The balance of charge due to electron and lithium ion transfer during charging and discharging is adjusted by changing the oxidation number of transition metal.

The conventional cathode materials have been lithium cobalt oxide; $LiCoO_2$. However, nickel rich materials have been replaced $LiCoO_2$ because of energy density limitations of $LiCoO_2$ and increasing raw material prices of cobalt. The chemical formula of nickel rich materials could be $LiN_xC_yM_zO_2$ depending on ratio of transition metals. Currently nickel rich materials containing 60% of nickel are partially used, and battery companies such as Samsung SDI, LG chemical, and SK innovation are trying to use nickel rich materials containing 80% of nickel in a few years [9]. Another promising lithium transition metal oxide cathode is over lithiated oxide so called Li rich cathode materials, whose Li atomic ratio is over 1. Thus, it can theoretically have a larger gravimetric capacity than any lithium transition metal oxide cathode, however low initial coulombic efficiency and unstable cycle life are remained challenges [10].

The cathode with the highest theoretical gravimetric capacity is sulfur as 1672 mAh/g. However, working potential of sulfur cathode is lower than lithium transition metal oxide and there are various technical obstacles for commercial use of sulfur, such as polysulfide dissolution and low electrical conductivity [11-14]. Moreover, sulfur cathode needs lithium containing anode materials such as lithiated graphite or silicon, and lithium metal anode, which

also have several challenges. Nonetheless, the highest gravimetric capacity of sulfur cathode is very attractive feature, and many research groups have proceeded to address these problems of sulfur cathode with various approaches.

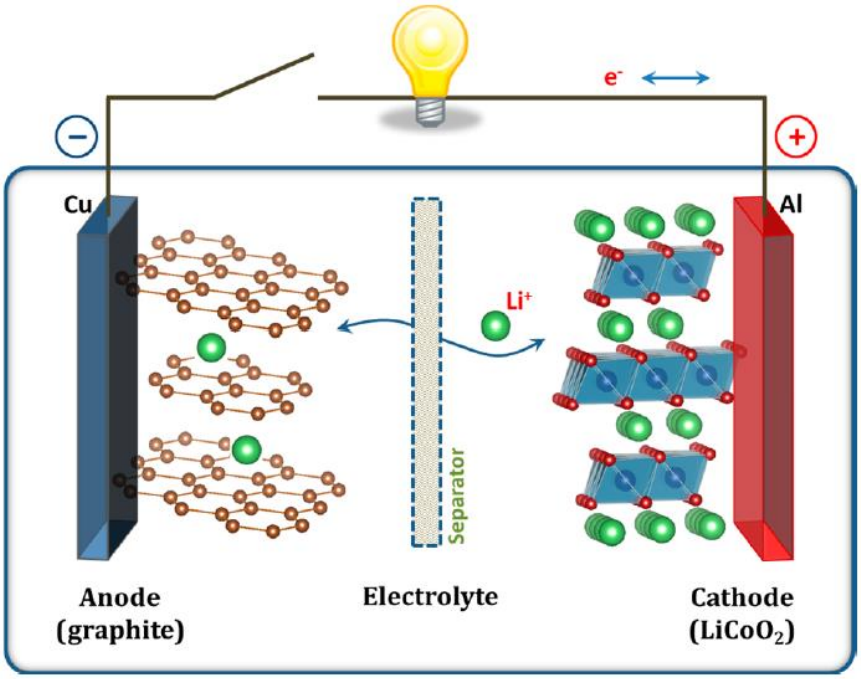

Figure 1. Basic principle of conventional LIBs. *Reprinted with permission from reference [15].*

Copyright 2013 American Chemical Society.

Anode

In charge process, reduction reaction takes place on anode. For example; C (graphite) + xLi^+ + xe^- → Li_xC (lithiated graphite). Here the electrons come from cathode materials through external circuit and the Li ions come from cathode materials through the electrolyte. In discharge process, the opposite directional reaction takes place on anode.

The conventional anode material has been graphite since commercial LIBs were invented. Graphite anode stores Li ions with a very stable structure, that is, Li ions are placed between graphene layers. During charging and discharging, Li ion moves along the graphene, and it is surrounded by six carbons in the charged state. There are two types of graphite: natural graphite and artificial graphite. Natural graphite could be mined in nature, and artificial graphite could be obtained by heat treatment of coal or petroleum pitch over 2500 ℃ [16]. Although price merits are in natural graphite, natural graphite requires post-processing because of its high surface area, and it shows performance degradation in long-term cycles compared to artificial graphite even after post-processing. Moreover, packing density of artificial graphite is better than natural graphite. In this respect, artificial graphitization of natural graphite is one of subjects that are expected to be developed in the anode industry.

The theoretical capacity of Si is 3579 mAh/g, whereas the theoretical capacity of graphite is 372 mAh/g. Hence, many researchers have been studying silicon anode to overcome the capacity limit of graphite anode. However Si anode suffers large volume expansion during lithiation which induces pulverization and continuous SEI formation [17-19]. The reported successful strategies alleviating volume expansion are void space control, matrix construction, stronger binder system and etc [20]. The strategy of void space control is designing void space in Si based materials and direction of volume expansion is oriented into that void space. Thus, Si based materials involving void space could remove volume expansion however it has issues regarding permeation of electrolyte into void space. The strategy of matrix construction could be classified by Li active and inactive matrix; SiO_x is one example of active matrix which alleviates volume expansion as reacting with Li ions [21,22]. $FeSi_2$ is one example of inactive matrix which alleviates volume expansion without reaction with Li ions [23-25]. The strategy of stronger binder system is to develop a binder having elasticity capable of withstanding volume expansion of Si. Despite these various strategies, the electrochemical performance of Si based anode is degraded if pressing for extent of commercial graphite electrode density. Thus, currently only 5 wt% or less of Si is added to graphite anode in industry.

Another promising next anode material is lithium metal anode, which has the highest gravimetric capacity. However there are some misconceptions regarding lithium metal anode. This topic will be discussed in detail on next section.

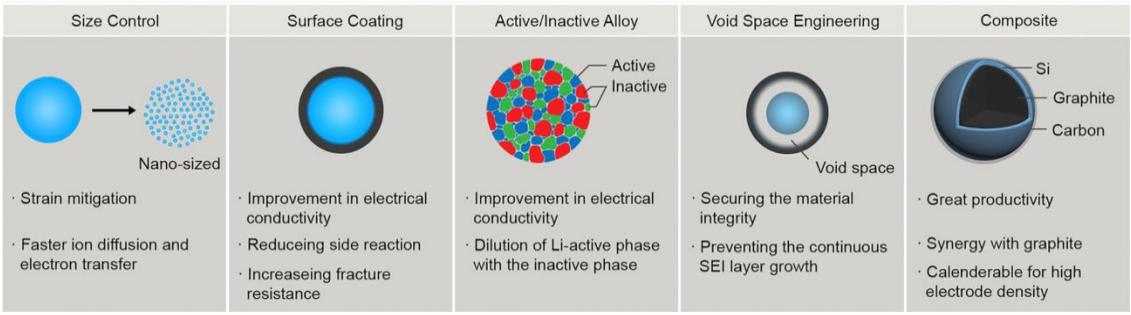

Figure 2. Possible strategies for Si anode. *Reprinted with permission from reference* [20]. *Copyright 2017 Joule*

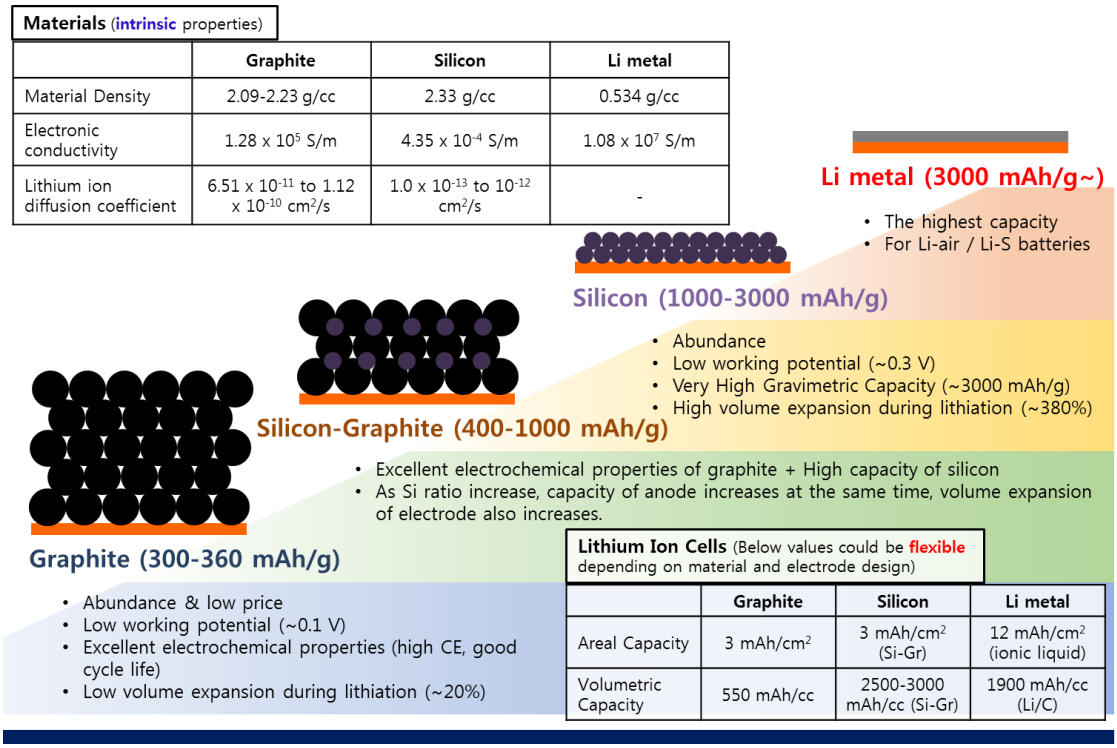

Figure 3. Development of anode materials

References of values

Li ion diffusion coefficient of graphite: [26]

Li ion diffusion coefficient of silicon: [27]

Areal capacity of graphite: [28]

Areal capacity of silicon: [28]

Areal capacity of Li metal: [29]

Volumetric capacity of graphite: [28]

Volumetric capacity of silicon: [28]

Volumetric capacity of graphite: [30]

Electrolyte

The role of electrolyte is charge carrier. The electrolyte is composed with lithium salt and solvent. Depending on kinds of solvent, the electrolyte could be classified by liquid electrolyte, gel polymer electrolyte, polymer electrolyte, and ionic liquid. In addition ceramic solid electrolyte is also used in all solid state batteries. The most popular electrolyte is nonaqueous electrolyte usually composed with $LiPF_6$ salt and mixture of carbonate solvent; for example 1.3 M $LiPF_6$ in Ethylene carbonate (EC): diethylene carbonate (DEC) = 3: 7 (w/w). The requirement of electrolyte is high ionic conductivity. For that, high dielectric constant and low viscosity are required for electrolyte solvents and broaden voltage window, low melting and high boiling point are also crucial for maintaining liquid state of electrolyte.

Separator

The role of separator is physically blocking between cathode and anode to prevent electron passing between cathode and anode via direct physical contact. Thus, the separator materials should be electronically insulator and provide pathway for ion conduction. Moreover, it has role of thermal shutdown for battery safety.

1.3 Which will be the next generation of anode material, Si vs. Li metal?

Introduction

Si and Li metal anode are two very promising anode materials for next generation LIBs. However, many people have misunderstandings and prejudices about these two promising anode materials. Both materials may have higher energy densities than graphite, but they need to be a little more careful in calculating the energy density. Therefore, I make a fair comparison of Si and Li metal anode in this section.

Prerequisites for Si and Li metal anode

Although, Si and Li metal have attractive feature of high gravimetric capacities, they also have immense obstacles inducing dramatic capacity fading. The origin of dramatic capacity fading is on volume expansion. Both Si and Li metal anode suffers volume expansion during lithiation process and the volume expansion induces physically detachment and electrochemically isolation of active materials with solid electrolyte interphase (SEI) formation (figure 4). Moreover, Li metal anode has another problem of Li dendrite growth, which could induce short circuit penetrating separator (figure 5). Therefore, failure mechanisms regarding volume expansion, SEI formation, and Li dendrite growth should be solved to use Si and Li metal anode for commercial LIBs anode materials.

Assuming that the deterioration of the two anode materials is now resolved, let's consider the lithium ion cell configuration of the two anode materials individually. In the case of Si anode, commercial cathode materials such as lithium cobalt oxide and nickel rich materials used with graphite anode could be used as it is. However, in the case of Li metal anode, it should be considered that which type of lithium metal anode is utilized in cells. There are two types of lithium metal anode. The first one is lithium metal as it is. In other words, before cell operating, anode part contains lithium metal. In this type, if conventional cathode material such as lithium cobalt oxide is used for counter electrode of lithium metal anode, then lithium plating occurs on lithium metal at first charging process. Thus, existed lithium metal before charging is just substrate rather than active materials, causing decrease of gravimetric capacity of lithium.

Therefore, sulfur or air electrode should be utilized for the first type of lithium metal anode because sulfur and air electrode are initially charged state so it need Li ion flow from anode to cathode in the first operation. The second type is actually lithium-free anode. In this case, there isn't lithium metal before the first charging, the lithium flowed from cathode materials is plated on anode substrate during charging. This type could be utilized with conventional cathode materials but its performance could be diverse depending on substrate design. Hence, the weight of substrate should be considered for fair comparison.

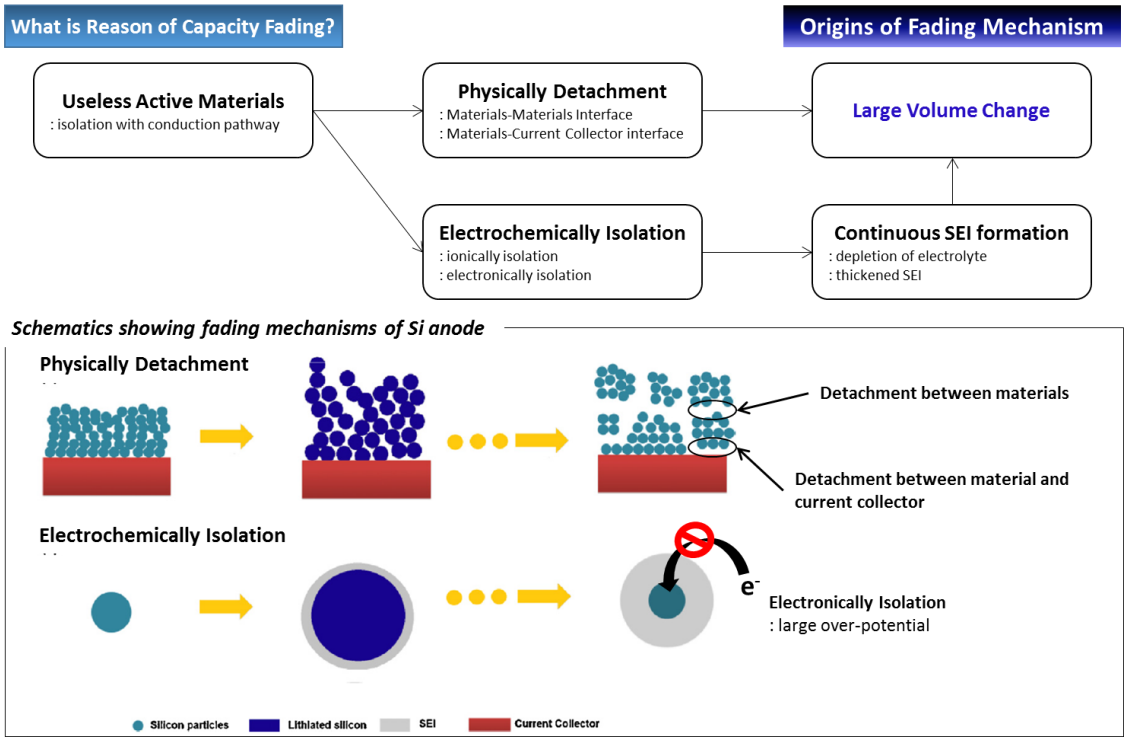

Figure 4. Fading mechanism of Si anode. *Reprinted with permission from reference*[18]. *Copyright 2012 Nano today*

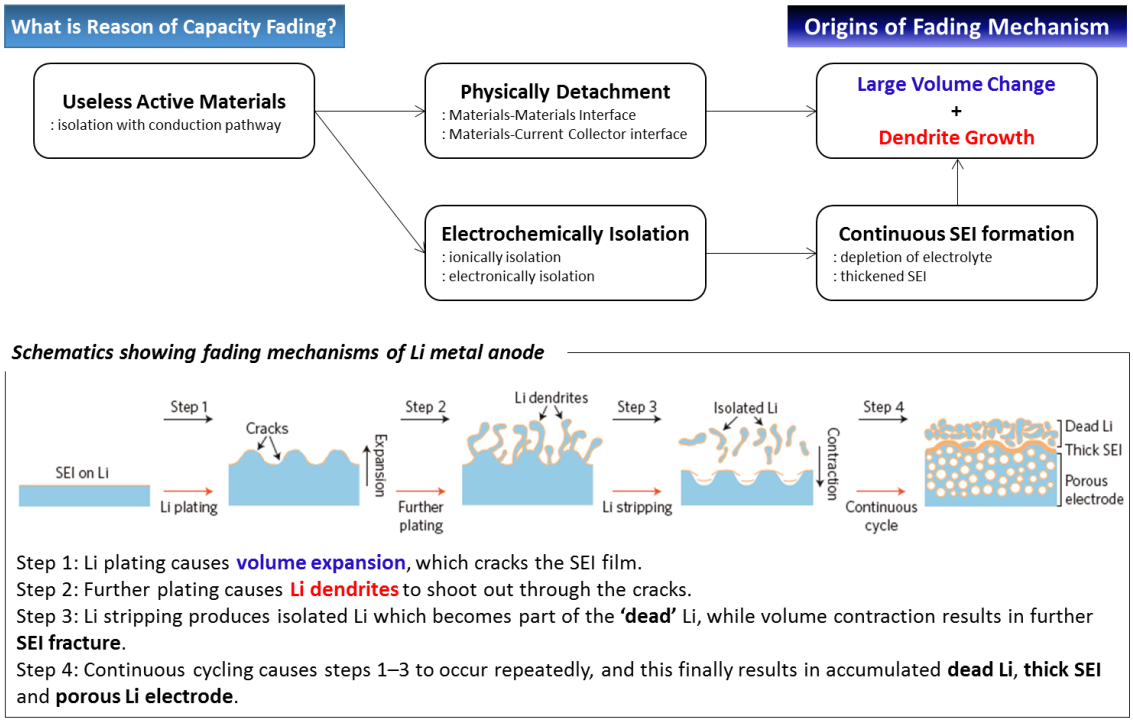

Figure 5. Fading mechanism of Li metal anode *Reprinted with permission from reference*[31]. *Copyright 2017 Nature Nanotechnology*

Theoretical Gravimetric Capacities; Si vs. Li metal

To calculate gravimetric capacities of electrode materials, we have to know molecular weight of the materials and reactive lithium moles per moles of electrode materials. Based on that, I calculated theoretical gravimetric capacities of Si and Li metal anode (figure 6). The gravimetric capacity of lithium free anode is infinite, so I calculated only lithium metal anode based on charged materials. Based on the discharged materials, gravimetric capacity of Si anode is 3579 mAh/g and based on the charged materials, gravimetric capacity of $Li_{3.75}Si$ (Si anode) and Li metal anode are 1857 mAh/g and 3862 mAh/g respectively. Hence, Li metal anode has possibility to assemble lighter batteries compared to batteries with Si anode theoretically.

Volumetric Capacities; Si vs. Li metal

To calculated volumetric capacities of electrode materials, we have to know gravimetric capacities and density of electrode materials. I used calculated gravimetric capacities based on charged materials and material density rather than electrode density. Note that electrode density could be diverse depending on the electrode design so I used material density to compare intrinsic materials properties. The volumetric capacities based on charged materials of $Li_{3.75}Si$ and Li metal are 2247 mAh/cc and 2062 mAh/cc respectively. Hence, Si anode has possibility to assemble denser batteries compared to batteries with Li metal anode theoretically.

In this context, Si or Li metal anode could be more favored depending on the purpose of batteries; denser or lighter and the counter cathode materials should be also considered. I calculated the theoretical capacities supposing that there are no deteriorations of Si and Li metal anode. However, the fancy strategies to overcome fading mechanism of Si and Li metal anode should be firstly developed for commercial use of Si and Li metal anode. In this thesis, I will focus on presenting unique strategies to overcome obstacles of Si anode and bridging these strategies to Li metal anode because the fading mechanisms of Si and Li metal anode are similar. Before presenting my strategies, I will review in the next section how degradation phenomena of Si anode have been observed so far.

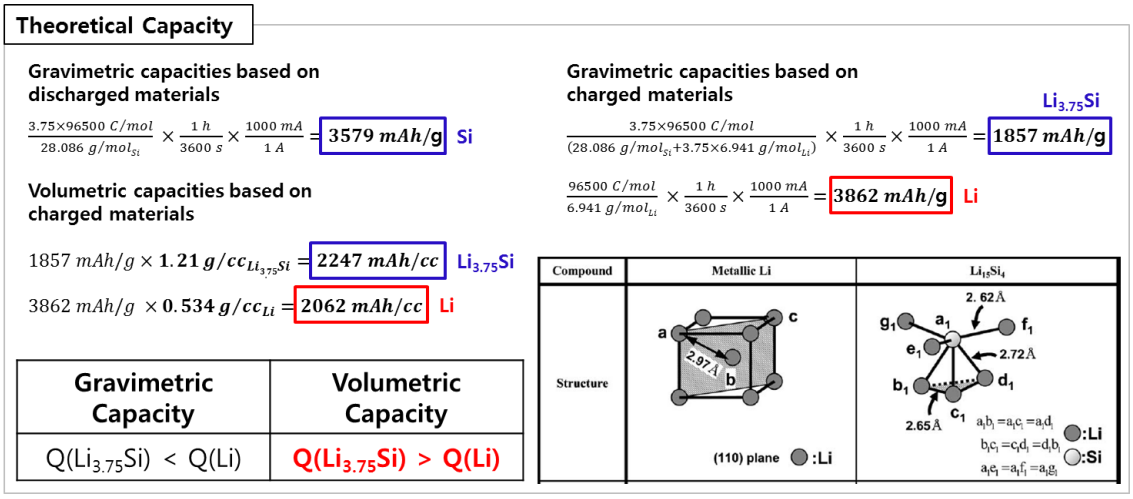

Figure 6. Calculation of theoretical capacities of Si and Li metal anodes. *Reprinted with permission from reference[32]. Copyright 2007 Journal of Applied Physics*

1.4 Critical phenomenon and analytical methods for Si anode

There have been many researches suggesting effective approaches for silicon (Si) based anodes for LIBs, but the use of Si anode materials in marketable LIBs is still narrow due to poor electrochemical outcomes based on commercial level test conditions of 3.0 mAh/cm^2, 1.6 g/cc and a minimum quantity of binder material of less than 4 wt%. There have been well-meaning studies showing stable cycling characteristics comparable to commercial graphite anodes, but no research has been done to overcome the performance of commercial graphite anodes in more than a thousand long-term battery cell tests[33-36]. In this context, understanding the Si-based anode phenomenon during the charge and discharge process is needed for improved electrochemical performance and development of advanced strategies to overcome the problem.

Investigating what happens on an electrode is a very difficult technique. Transferring a sample taken from a cycled electrode of a lithium-ion cell to analytical equipment without exposing it to oxygen, water, or any contaminants is a very tricky and complex task[37]. Although cautiously moved to equipment, organic materials on electrodes such as binders and SEI can be impaired during analysis, such as electron microscopy with high energy sources. Hence *in situ* research techniques has been developed with various analysis instruments; Raman, X-ray diffraction (XRD), transmission electron microscopy (TEM), nuclear magnetic resonance (NMR) [6]. Compared to ex situ method with transferring problem, in situ technique has obvious advantages. Nevertheless, there are approximately variances between the *in situ* system and the actual LIB. For instance, in field TEM, volatile electrolytes can't be used because of their vacuum condition. Therefore, ionic liquids and solid electrolytes have been generally used[38]. Nonetheless, the conductivity of these electrolytes is worse than that of usual carbonate electrolytes and the SEI composition will change. Therefore, we must constantly strive to develop *in situ* measurement systems with actual LIB conditions or to solve problems with *in situ* measurement systems. In addition, the analysis should be performed with logical assumptions and reasons. Thus, I have summarized the progress of the investigation tools for the Si anode over the past two years. This section shows how to analyze the phenomena on the Si electrode and how it can be helpful to researchers working on Si-based anode development

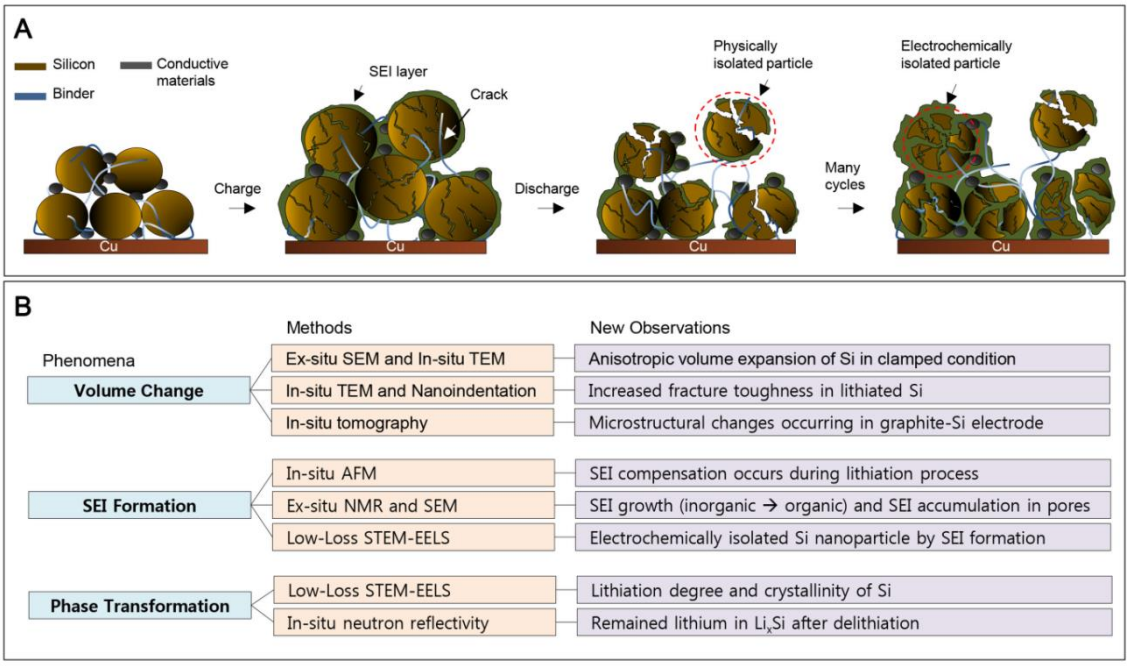

Figure 7. (A) Schematic view of Si anode fading mechanism (B) Summary of recent Si anode phenomena analysis method and results. *Reprinted with permission from reference*[39]. *Copyright 2017 Current Opinion in Electrochemistry*

Critical issues in analyzing Si-based anode

Massive volume changes and SEI formation are the origin of the fading mechanism at the Si dominant anode. Massive volume changes lead to electrode crushing and cracking. The newly exposed surface induces fresh SEI formation and repeated cycling creates growth of the SEI layer (Figure 7A). This phenomenon leads to enormous volumetric changes and SEI formation leads to a physically loss of active materials or electrochemically isolated active material from the conduction pathway. It is a dead Si that can't be donated to capacity[18,40]. Another important problem with Si dominant anodes is phase transformation. Depending on the atomic structure, the mechanism of the phase transition can be dissimilar, and thus the electrochemical performance can vary[41,42]. Here we classify the phenomena of Si electrodes into three categories. Volume change, SEI formation and phase transformation (Figure 7B).

Volume Change and Mechanical Properties

The mechanical properties of volume change during charging and discharging are the most important problems in Si dominant anodes because all the fading mechanisms of Si dominant anodes are directly or indirectly related. Accordingly, there are various methods for detecting the mechanical properties associated with the volume change of the Si-based anode. It is the simplest way to observe the volumetric expansion by measuring the thickness of the electrode after cycling. This process can only be carried out in a drying room or glove box for safety reasons and can prevent unexpected chemical changes. However, the mechanical effect of Si volume expansion, the nature of the expanded material, or the damage to the periphery of the active material couldn't be analyzed via simply measuring the volume change of the electrode. Therefore, it is necessary to develop a technique for characterization of the active material itself during Si expansion as well as measuring the volume change of the electrode.

In recent years, *in situ* TEM techniques have clearly improved. In addition to observing the expansion of particle and crack formation, investigators also attempt to expose the comprehensive impact and characterization of Si expansion. Lee et al. have mentioned a study on the relationship between the direction of Si expansion in compression and the fractional resistance and clamping[43]. The utilized Si nanofillers were synthesized via Si wafer etching. The expansion rate heading <110> direction was higher than the expansion rate heading <100> direction in the unclamped condition and the pressed plane of <110> direction motivated the further expansion heading <100> direction. These investigation results were proved via the *ex situ* SEM and *in situ* TEM analysis (Figure 8A). It showed the direction of Si expansion is more preferable than the unclamped region which is the void space rather than the clamped region. They also found that by mechanical clamping, fracture resistance could be improved to enable

larger critical dimensions of Si without breakage. Wang et al. describes the strength and ductility of Si and lithiated Si through *in situ* TEM nanoindentation[44]. They used Si nanowires and thin films as the active material and provided the TEM results of fragmented Si and strained Li silicide when the partially lithiated Si nanowires were compressed (Figure 8B). They also calculate the fracture toughness and energy of lithiated Si as a function of the Li concentration from the nanoindentation, and the calculated fracture properties increase significantly with increasing Li content (Figure 8B). As a result, they found the initial Si to be brittle whereas the Li silicide showed ductile feature. Another excellent surveillance technique for volume expansion is operando tomography. Pietsch et al. stated the microstructure change of graphite-silicon mixed electrode (weight ratio of graphite and silicon = 75 (graphite): 25 (silicon) and active material ratio at electrode is 80 wt%)[45]. The blended electrode showed an expansion of 35% and a porosity reduction of 8% (Fig. 3C). This technique can measure the microstructural changes that occur in the electrode during lithiation/delithiation and is predictable to be useful for the analysis of porous Si electrodes.

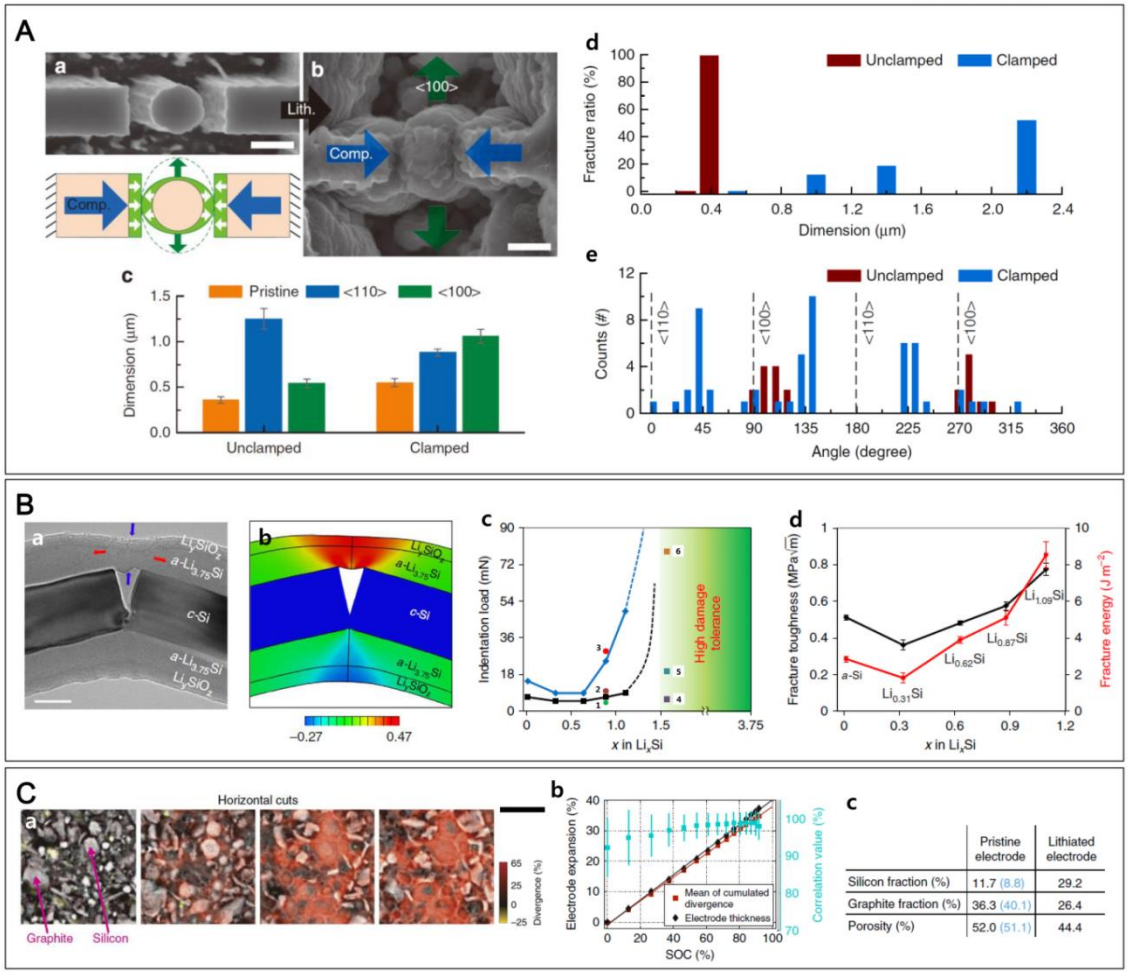

Figure 8. Recent progress of investigating volume changes and mechanical features of Si dominant anode (A) facture resistance of Si anode in compressed state, SEM images of (a) Si nanopillar before lithiation and (b) Si nanopillar after lithiation in compressed state, (c) expansions of Si anode dependent on direction, (d) fracture ratios dependent on extent of compression walls, (e) amount of the fracture location depending on the angle of cracks **(B) comparison of fracture toughness; lithiated Si vs. pristine Si** (a) TEM image after partially lithiation into Si nanowires and the sample was bent, (b) elastic-plastic deformation properties as TEM image at (a) via finite element simulation. (c) lithiation extent in LixSi vs. indentation load graphite, points were measured via experiment and the dashed line was expected values via calculation. The blue line denotes the upper load boundary where massive cracking occurred, the black line denotes the lower boundary below where no cracking happened. (d) lithiation extent vs. facture toughness and energy. **(C) Microstructural dynamics of Si and graphite blending anode** (a) the lithiation extent (from left to right; 0, 17, 46, 92%. Scale bar = 50 μm) vs. divergence in Si and graphite blending anode. (b) Expanded electrode thickness (black) and divergence (red) of Si and graphite blending electrode. (c) faction of Si and graphite in pristine and lithiated blending electrode. The chemical composition of the electrode is evidence for the black values and segmentation of the tomographic data in the three phases is evidence for blue

values. *Reprinted with permission from reference*[39]. *Copyright 2017 Current Opinion in Electrochemistry*

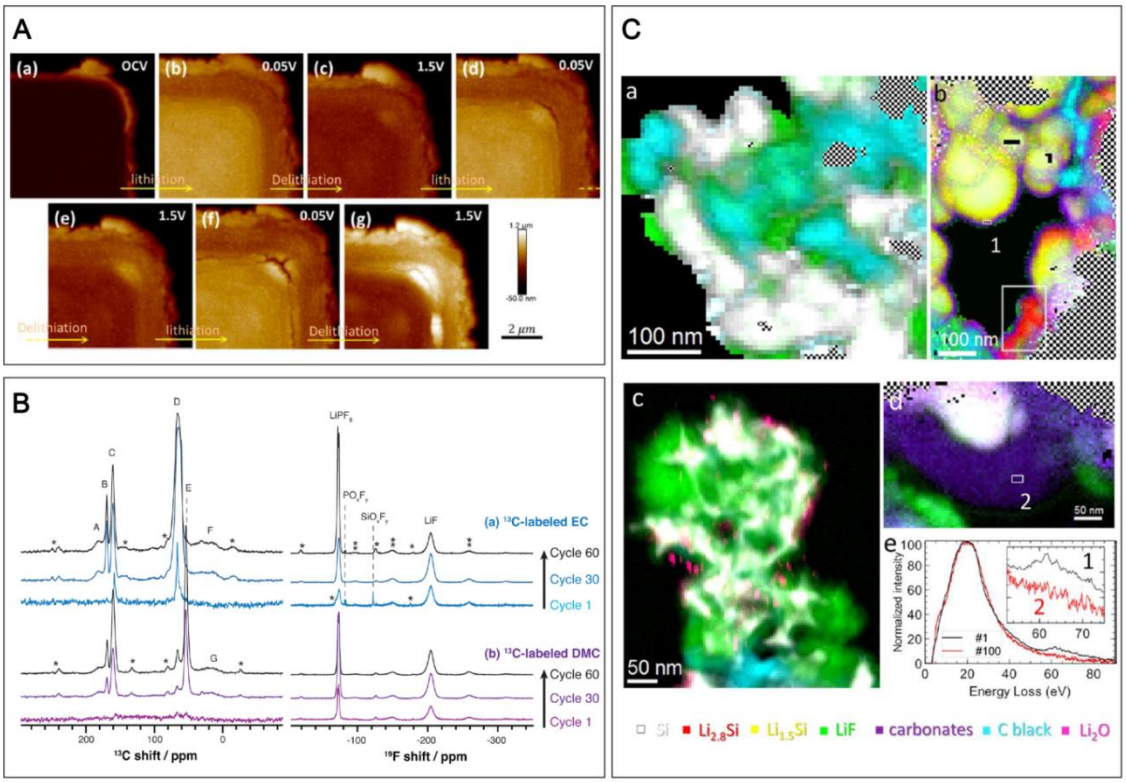

Figure 9. Recent progress of investigating SEI formation on Si dominant anode (A) SEI compensation happens during lithiation manner (a) AFM images of SEI layers during (a-c) the first cycle, (c-e) the second cycle, and (e-g) the third cycle. **(B) SEI growth (inorganic organic) and SEI accumulation in pores, Results of 13C, 7Li, and 19F ssNMR with** (a) 13C EC (blue) and (b) 13C DMC (purple) (C) Analysis of dead Si nanoparticle caused by continuous SEI growth, STEM-EELS element mapping of 30% lithiated Si anodes. (a) LiF dominantly formation after 1st lithiation at unlithiated part, (b) ~20 nm thick carbonate and LiF covered after 1st lithiation at crystalline Si/LixSi core-shell part. (c) dead Si nanoparticles in LiF matrix after 100th delithiation. (d) ~100 nm thick carbonate dominant SEI layer after 100th delithiation. (e) low-loss EELS spectra on site 1 and 2 representing low resident Li extent on SEI layer after long-term cycling. *Reprinted with permission from reference*[39]. *Copyright 2017 Current Opinion in Electrochemistry*

Solid Electrolyte Interphase Formation

Anode materials with a working potential lower than the reduction potential of the carbonate electrolyte such as graphite and silicon could not avoid forming the SEI layer[46]. However commercial graphite anodes exhibit excellent cycle life in carbonate electrolytes, because SEI formation somewhat lessens initial coulombic efficiency and no further SEI formation[47]. Conversly, the Si anode undergoes a gradual capacity decrease by continuous SEI formation during the cycle, since the volume expansion leads to a new electrode-electrolyte interface[40]. Thus the interaction between volume expansion and SEI formation (Continuous SEI thickening) results in an electrochemically isolated Si. Therefore, studying the SEI layer and bulk expansion is important to start a new strategy for Si dominant anode materials.

One recent and excellent approach concentrated on direct observation of SEI degradation using an *in situ* Atomic Force Microscope (AFM) [48]. In this study, the authors showed a noteworthy difference between the center and edge of the Si active material, and SEI formation was favored where extensive cracking occurred. It is the edge part. The cracks formed during the first lithiation were not covered. In subsequent delithiation and lithiation, the SEI layer of the degraded site was developed (Figure 9a). The LIB academic community has long discussed and forecast the place and timing of this SEI formation, but it was typically predictive and indirect evidence. This study demonstrated practical and direct evidence of SEI formation through experimental observations.

Alternatively, material composition and distribution become additional exploration points in SEI research,. Michan et al. reported 7Li, 19F and 13C solid state NMR (ssNMR), FIB and SEM were used to study SEI growth and SEI accumulation in electrode pores[49]. They compared three electrodes in the 1^{st}, 30^{th}, and 60^{th} cycles. In the 19F ssNMR, the primary peak of the LiF peak intensity remained almost constant up to the 60^{th} cycle, which means LiF species predominantly formed in the first cycle. Conversely, 13C ssNMR contains the material of the SEI presentation CH_3R, $ROCO_2Li$, including the organic species as $-OCH_2CH_2O-$, CH_2O and functional groups, the oligomeric species RCH_2R and CH_3CH_2R ethylene carbonate, lithium, butylene carbonate, RCO_2Li, HCO_2Li, Li_2CO_3, Li methyl carbonate. The signal strength of these materials increased after the 30th cycle; It means that the organic SEI layer grows. They also found that as the cycle progresses, the SEM formation of the FIB cross-section leads to the disappearance of pores.

The NMR studies delivered a broad opinion of the SEI components but could not provide spatial evidence for specific particles. Boniface et al. exploited electron energy loss spectroscopy (EELS) in scanning transmission electron microscopy (STEM) mapping scanning SEI components with a resolution of 5 nm or less. Figure 9C shows the color mapping of SEI components on Si electrodes cycled in a 30% state of charge (SOC) [50]. LiF and carbonate

components were detected in the electrodes after the first and 100th cycles, and the thickness of the carbonate layer increased from ~ 25 nm to ~ 100 nm. They also found that the LiF-rich SEI layer is more beneficial than the carbonate-rich SEI layer. This means electrochemical insulation due to carbonate accumulation.

Phase Transformation

The preceding two sections have concentrated on the mechanical (volume expansion) and chemical (SEI formation) problems of Si-based electrodes. From now on, I will consider the phase transformation that can reflect the atomic change of the Si-based electrode, namely the dynamics and reversibility of Si and Li_xSi. Previously, structural changes in the lithiation of Si have been studied in a variety of ways such as in situ XRD, TEM and NMR[42,51,52]. Among them, specific properties related to phase transformation such as amorphization of crystalline Si after lithiation, a crystalline phase of $Li_{15}Si_4$, and anisotropic lithiation of crystalline Si have been introduced and studied so far. However, there are little noticeable results in terms of sophisticated quantitative and nanoscale analysis. The STEM-EELS method presented in the previous section can be a suitable technique for studying the phase change of the Si electrode[50]. With this technique, the degree of lithiation and crystallinity of Si can be observed. Thus, the dense SEI layer allows the discovery of an electrochemically isolated Si moiety (Figure 10A).

Another technology is the neutron reflectance, which allows non-destructive and quantitative analysis at nanometer resolution. Seidlhofer et al. utilized *in situ* neutron reflectivity to study the alloying of bulk crystalline silicon[53]. They observed the degree of retention in the Si layer with depth and time using single-crystal Si of 1 cm size. The Li silicide layer was segmented into two distinct parts; Highly lithiated skin areas ($x \approx 2.5$ in Li_xSi) and partially lithiated growth areas ($x \approx 0.1$ in Li_xSi) (Fig. 4B). After completely delithiation, The Li content in the skin area was maintained at $x \approx 1.1$ in Li_xSi. However, the thickness of the skin layer remained one of the growth regions as cycle proceeded (Figure 10B). This denotes that the thick Si anode has inactive and irreversible regions.

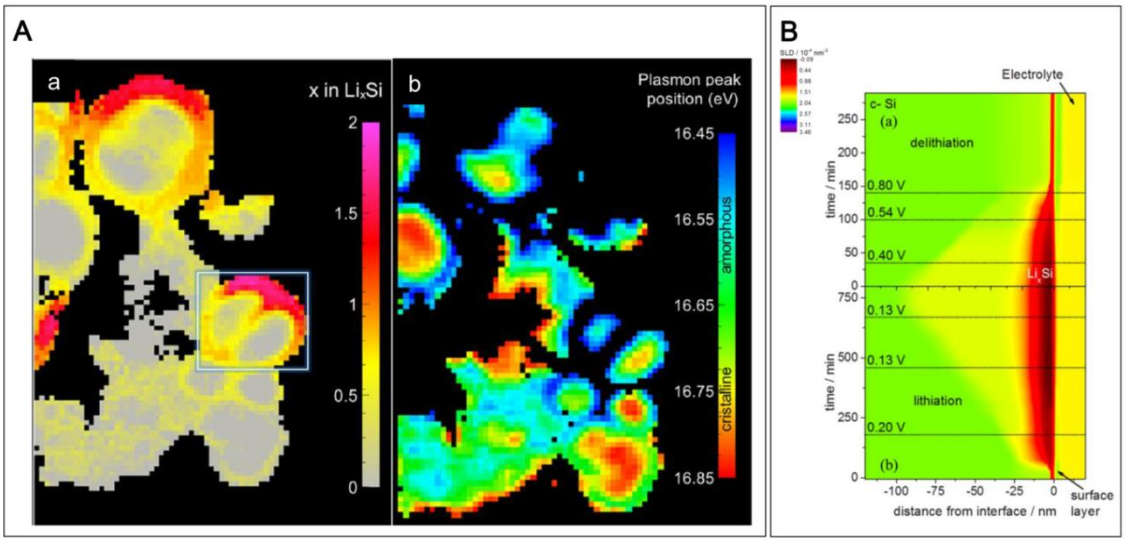

Figure 10. Recent progress of investigating phase transformation on Si dominant anode (A) Lithiation extent into Si and phase transformation of Si during lithiation (a) Chemical element STEM-EELS mapping of Si anode after 10th lithiation. (b) crystalline change of Si via STEM-EELS mapping. (B) Persisted Li in LixSi after delithiation, the scattering length density graphs after (a) 2nd charge and (b) 2nd discharge and the x axis is distance from the interface (c-Si (green), the electrolyte (yellow), surface lithiation (red/dark-red), and deep lithiation (red-yellow)). *Reprinted with permission from reference*[39]*. Copyright 2017 Current Opinion in Electrochemistry*

In conclusion, I examined the exclusive properties of Si-based cathodes as said by three features. 1) the volume change extended with mechanical properties, 2) the SEI formation associated with the surface reaction on the Si electrode, and 3) the phase transition by atomic rearrangement. In the first section (volume change), we summarized the new observations of volume changes and mechanical properties at the Si anodes. An anisotropic volume expansion when Si is compressed, an increase in fracture toughness of lithiated Si, and a change in microstructure happening in graphite-Si electrode. The following sections describe when, where, and how the SEI layer is built, the configuration of the SEI, and the fading mechanism induced by the SEI thickening. In the last section, the phase transition of Si is concentrated and the Li content is maintained in Si after complete delithiation, which is the electrochemical reversibility ratio of Li-Si reaction. For further research, the analysis of Si-based anodes should focus on higher scale evaluation.

The ultimate goal of a basic understanding of this phenomenon in Si-based anodes is to derive a solution that can use Si-based anodes extensively in commercial LIBs. In particular, the intrinsic expansion of the Si active material itself can not be dynamically controlled at the atomic level, but expansion at the electrode level should be considered rather. Thus, the adverse effects due to electrode expansion are controlled by the pore structure, the buffer matrix or the binder material which suppresses crushing and cracking. While it is necessary to declare that SEI formation is unavoidable owing to intrinsic reduction potentials, there is still a need to advance functional electrolytes to create a strong SEI layer. In addition, the atomic design of Si-based materials should deliver faster dynamics and sophisticated reversibility based on phase change researches. We hope this review will be of excessive support to researchers developing Si-based anodes for LIB.

1.5 Previous Strategies for Si anode

Previously, there have been numerous strategies for Si anode. The strategies could be classified by five; size control, surface coating, active/inactive alloy, void space engineering, and composite. In this section, the representatives of each strategy will be presented. The first is size control. In 2003, J. Graetz et al. reported cycle performance nanostructured Si film anode was improved compared to bulk Si anode (figure 11) [54]. In 2007, C. K. Chan et al. reported Si nanowire anode, which was pioneer work of nanowire shaped Si anode (figure 11) [55]. After these works, many researchers have reported numerous following works changing Si morphologies and nanosizing strategies were effective to improve electrochemical performance of Si anode because mechanical strength was improved [56-65]. The second strategy is surface coating. There have been various surface coating materials such as polymer, carbon, metal and metal oxide. Recently, unique graphene coating methods were reported. In 2015, I. H. Son et al. reported silicon carbide-free graphene growth on Si nanoparticles for LIBs (figure 12) [28]. Usually, carbon coating on Si at high temperature could induce silicon carbide, which is lithium inactive material. Thus, after carbon coating, gravimetric capacity could be dramatically decreased. However, I. H. Son et al. developed silicon carbide free method and its volumetric energy density reached 972 Wh/l. In 2016, Y. Li et al. reported conformal graphene growth on micron Si, at the same time constructing void space. They also reveal mechanical strength of graphene coating via *in situ* TEM analysis (figure 12) [36]. The third strategy is active/inactive alloy. In 2016, S. Chae et al. reported micron sized Fe-Cu-Si ternary composite composing Si nanoparticle, $FeSi_2$, and $Cu_{3.17}Si$ (figure 13) [66]. The inactive alloys of $FeSi_2$, and $Cu_{3.17}Si$ successfully alleviate volume expansion of Si and they also enable higher tap density of materials. The fourth strategy is void space engineering, which is one of the most used strategies with nano sizing. The most well-known of void space engineering are nanotubes and yolk shell structure. In 2009, M. Park et al. reported Si nanotube anode which was synthesized via alumina template and etching (figure 14) [61]. The pore in nanotube structure alleviated volume expansion of Si. In 2012, N. Liu et al. reported yolk shell structured Si anode (figure 14) [60]. In the design, yolk is Si and shell is carbon. When Si is expanded, the void space between shell and yolk alleviate the expansion. The last strategy is composite. There have been diverse composite materials, such as polymer, carbon, metal, and metal oxide. Recently, the best performing composite materials was graphite. In 2016, M. Ko et al. reported scalable synthesis of Si nanolayer embedded graphite via silane CVD method (figure 15) [35]. The thin Si nanolayers on graphite showed lower volume expansion compared previous works. In 2017, N. Kim et al. reported Si nanolayer embedded on etched graphite which enables higher power and energy density compared to Si nanolayer embedded graphite concepts (figure 15) [67]. In order to help

understanding, I have divided and explained the strategies and examples of Si anode development, but in practical approach, the successful strategies with great electrochemical performance are made by combining 2 or 3 strategies.

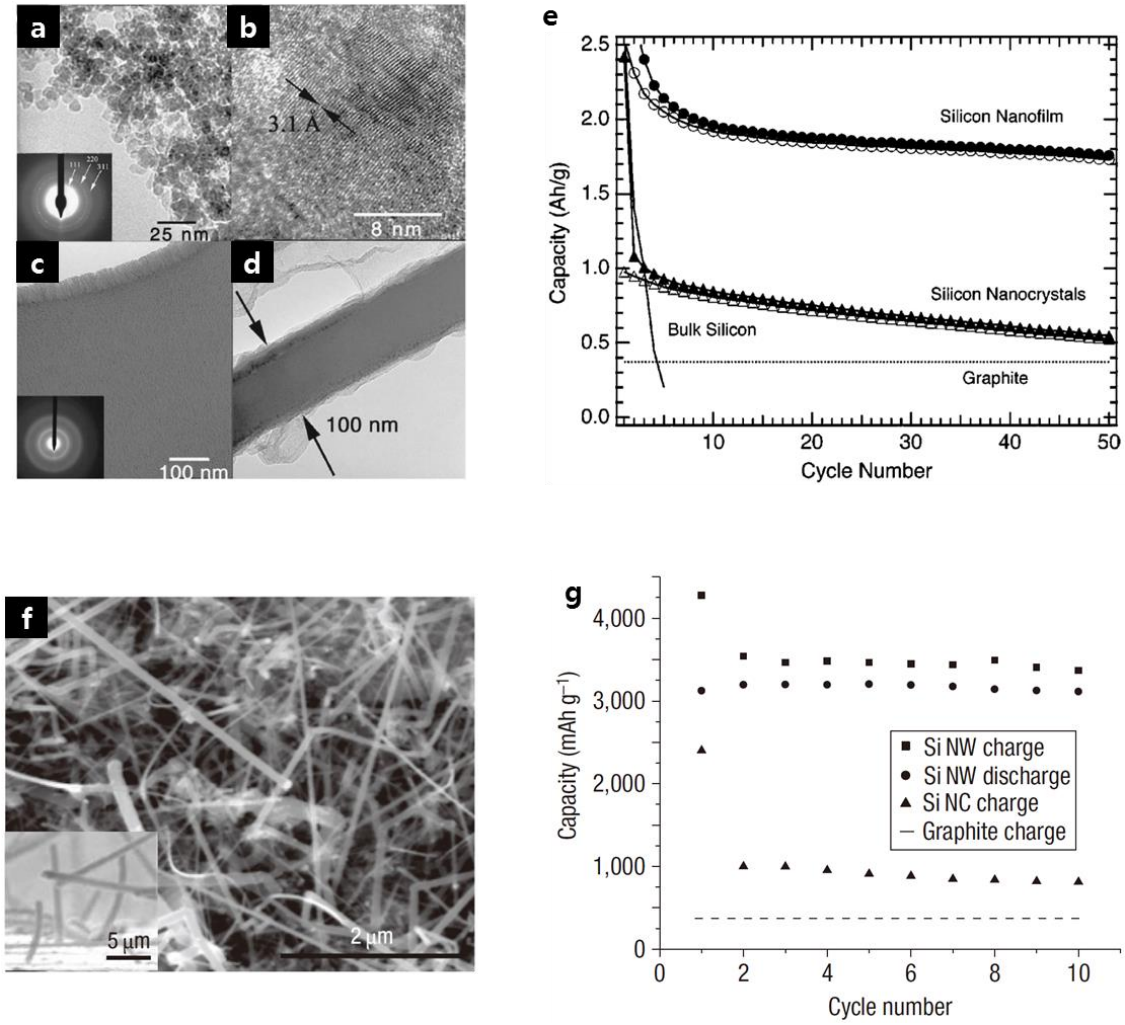

Figure 11. Representatives of the size control strategy (a-e: silicon nanofilm, and f, g: silicon nanowire). (a) TEM image and electron diffraction pattern of silicon nanocrystals. (b) high-resolution TEM image of silicon nanocrystal. (c) TEM image and electron diffraction pattern of silicon nanofilm. (d) TEM cross section image of silicon nanofilm. (e) half-cell cycle performance of silicon nanocrystals and nanofilm with theoretical capacity of graphite and experimental reference result of bulk silicon. (f) SEM images of pristine silicon nanowires. (g) half-cell cycling performance of silicon nanowire (Si NW) and silicon nanocrystal (Si NC) with theoretical capacity of graphite. *Reprinted with permission from reference [54,55]. Copyright 2003 Electrochemical and Solid State Letters and Copyright 2008 Nature Nanotechnology*

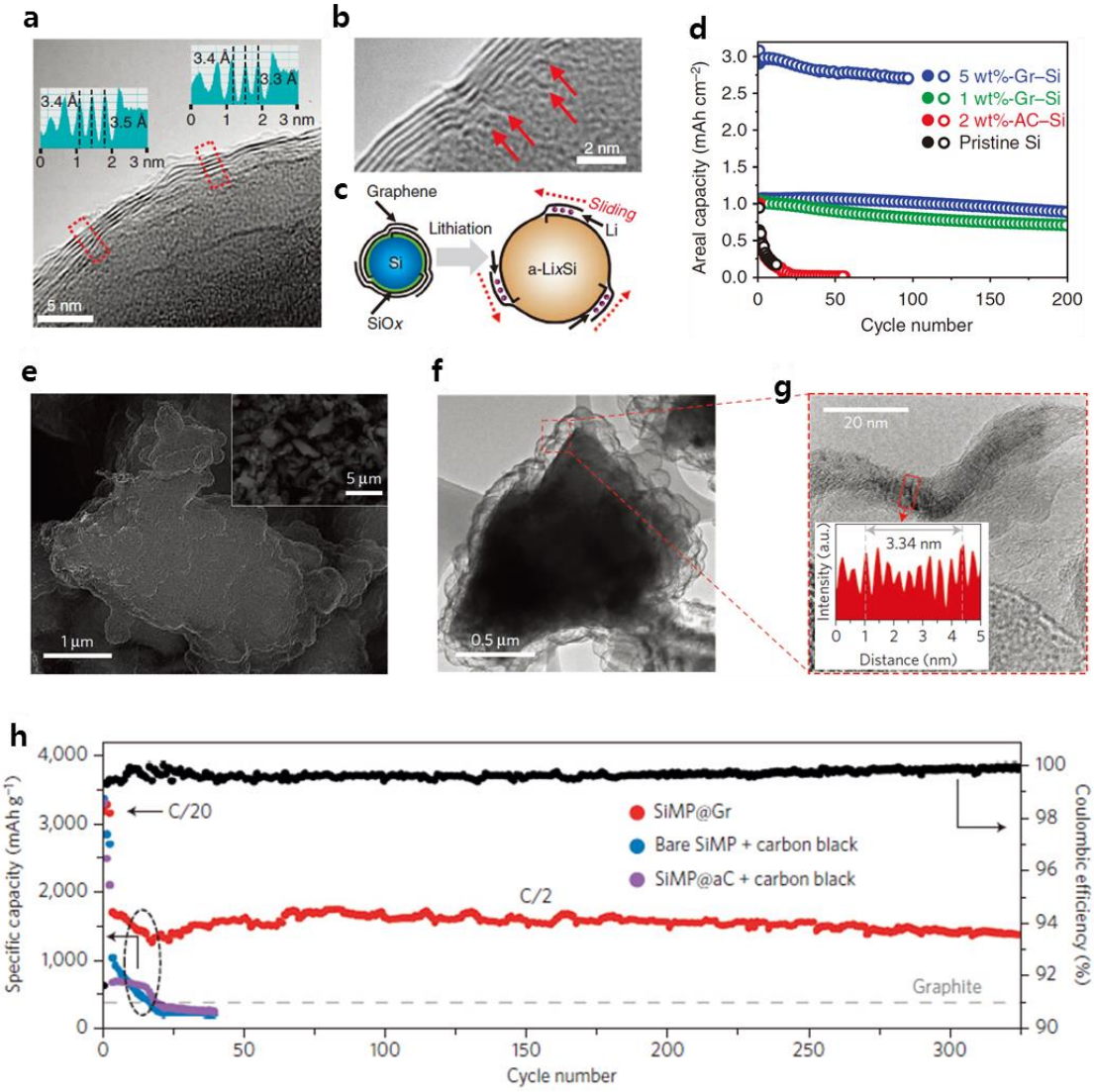

Figure 12. Representatives of the surface coating strategy (a-d: silicon carbide free graphene coating, and e-h: graphene cage coating). (a) TEM image of Graphene coated Si NP (Gr-Si). The line profiles from the two red boxes indicate that the interlayer spacing between graphene layers is ~ 3.4 Å. (b) magnified TEM image of graphene layers visualizing the origins (red arrows) from which individual they grow. (c) A schematic illustration showing the sliding process of the graphene coating layers that can buffer the volume expansion of Si. (d) Half-cell cycling performance of Gr-Si depending on the weight ratio of graphene. (e) SEM image of a graphene-encapsulated Si microparticle (SiMP@Gr). (f) TEM image of an individual particle of SiMP@Gr. (g) High-resolution TEM image of the graphene cage's layered structure. The intensity plot shows that ten layers span a distance of 3.34nm (average inter-layer distance: 0.334 nm). *Reprinted with permission from reference[28,36]. Copyright 2015 Nature Communication, and Copyright 2016 Nature Energy.*

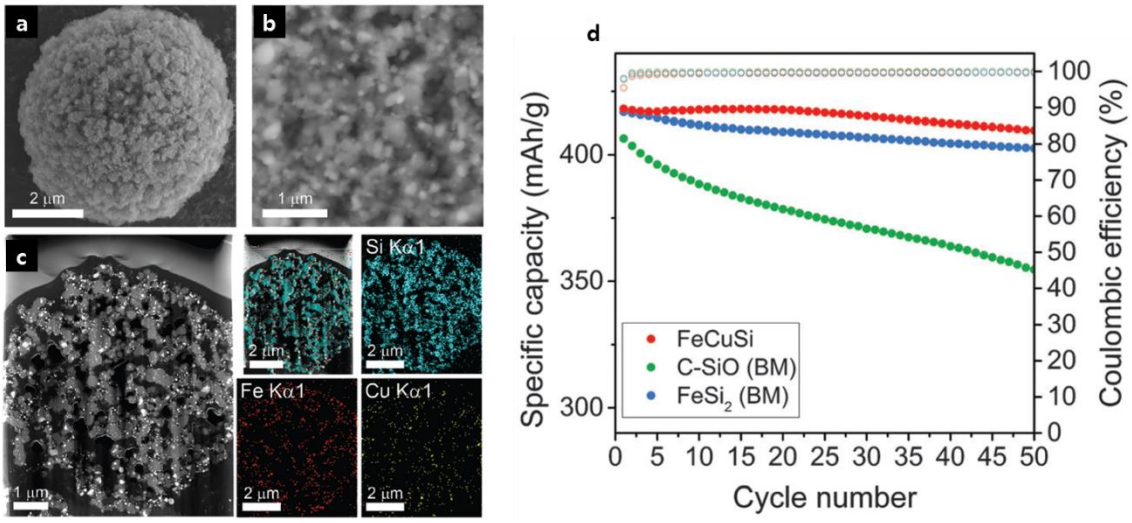

Figure 13. Representative of the active/inactive alloy strategy. (a-d: Fe-Cu-Si ternary composite). (a) SEM image of FeCuSi. (b) Magnified cross-sectional SEM image of FeCuSi. (c) HAADF-STEM image and EDS mapping of FeCuSi in cross sectional view. (d) Half-cell cycling performance of FeCuSi with C-SiO and $FeSi_2$ references. *Reprinted with permission from reference [66]. Copyright 2016 Energy and Environmental Science.*

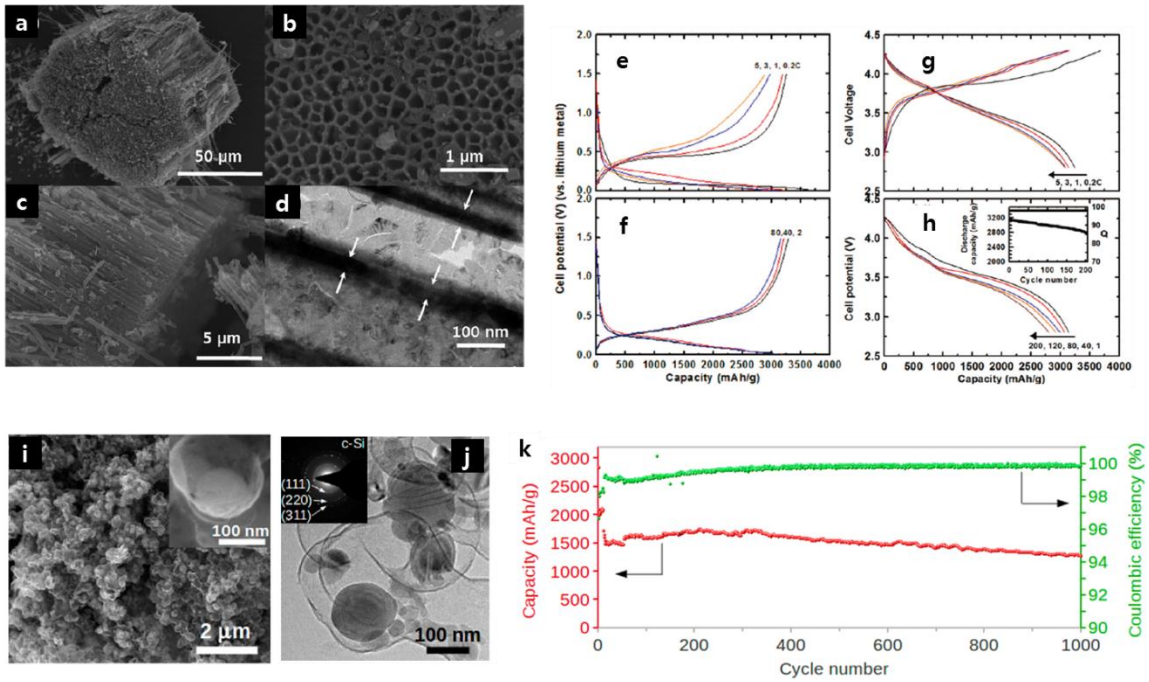

Figure 14. Representatives of the void space engineering strategy. (a-h: silicon nanotubes and i-k: yolk-shell structures). (a) SEM images of Si nanotubes. (b) Top view SEM images of Si nanotubes. (c) Side view SEM images of Si nanotubes. (d) TEM images of Si nanotubes (e) Half-cell voltage profiles of Si nanotubes anode from 0.2 to 5C. (f) Half-cell voltage profiles of Si nanotubes anode after 2nd, 40th, and 80th cycle. (g) Full-cell voltage profiles of Si nanotubes anode from 0.2 to 5C. (h) Full-cell cycling performance of Si nanotubes anode at 1C (cathode was $LiCoO_2$). (i) SEM image of yolk-shell particle. (j) TEM image of yolk-shell particle with SAED pattern. (k) Half-cell cycling performance of yolk-shell particles anode. *Reprinted with permission from reference [60,61]. Copyright 2009 Nano Letters and Copyright 2012 Nano Letters.*

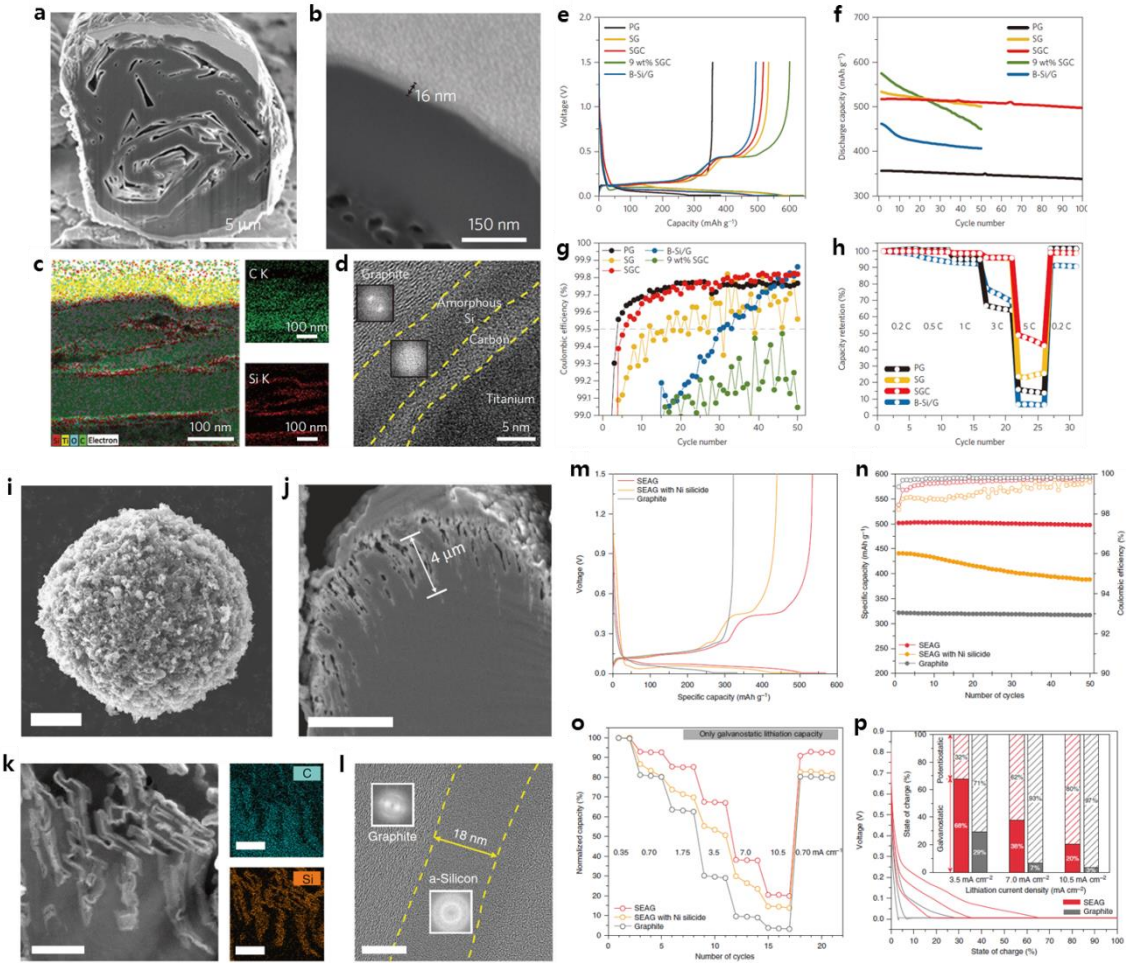

Figure 15. Representatives of the composite strategy. (a-h: silicon nanolayer embedded graphite/carbon (SGC) and silicon nanolayer embedded etched graphite (SEAG)). (a) SEM images of cross-sectional SGC hybrids (b) on the graphite surface. (c) STEM images of SGC with elemental mapping by energy-dispersive spectroscopy. (d) High-resolution TEM image at the interfacial region of the SGC, with fast Fourier transform inset images. The yellow dotted curves indicate the boundaries between graphite, amorphous Si and carbon. (e) Voltage profiles of pristine graphite (PG), Si-nanolayer-embedded graphite (SG), SGC and physically blended nano-Si/graphite (B-Si/G) measured at 0.1 C. (f) Half-cell cycling performances of PG, SG, SGC, 9 wt%-SGC, and B-Si/G cycled at 0.5 C. (g) Coulombic efficiencies of the samples depending on cycle number. (h) Rate performance of SGC from 0.2 C to 5 C, compared with PG, SG and B-Si/G. (i) SEM images of SEAG. (j) Cross-sectional SEM image of SEAG. (k) STEM images of magnified surface of SEAG with EDS mapping analysis. (l) HR-TEM images at the interfacial region of SEAG. (m) Voltage profiles of SEAG, SEAG with Ni silicide, and graphite in the 1st cycle (n) Half-cell cycling performances of SEAG, SEAG with Ni silicide, and graphite. (o) Rate performance of SEAG, compared to SEAG with Ni silicide and graphite. (p) Voltage profiles during charging process of SEAG and graphite, measured at increasing current densities; the

inset shows a plot of SOC divided into galvanostatic/potentiostatic stages at each current density. *Reprinted with permission from reference [35,67]. Copyright 2016 Nature Energy and Copyright 2017 Nature Communication.*

1.6 Scope and organization of this dissertation

The objective of this dissertation is the study of Si based anode materials for LIBs and perspectives on future anode materials.

The chapters are categorized as follows:

Chapter 2 presents new design of C/Si nanolayer/macroporous C trilayer covered graphite
: Silicon-graphite composite for > 650 mAh/g anode materials

Chapter 3 presents new design of C/Si nanolayer/C micro cage
: Silicon-carbon composite for > 1000 mAh/g anode materials

Chapter 4 presents perspectives on future anode materials with challenges facing anode materials for LIBs

Chapter 2

C/Si nanolayer/macroporous C trilayer covered graphite : Silicon-graphite composite for > 650 mAh/g anode materials

2.1 Introduction

The ever-growing demands for electric vehicles and energy storage system has stimulated the development of high-energy density lithium-ion battery (LIB), through the exploration of various emerging anodes [68-74]. Among these materials, Si has been considered as the most promising candidate because of its 10 times higher gravimetric capacity than that of conventional graphite, low working potential, and low cost. However, despite of these attractive features, the utilization of Si-dominant electrodes has been limited by the tremendous volume expansion of Si upon cycling, which brings about particle pulverization, loss of inter-particle electrical contact, and continuous formation of solid electrolyte interphase (SEI) layer [74-84].

In order to address these severe obstacles, intensive efforts have been devoted toward development of nano-engineering such as nanoparticle, nanowire, and nanolayer. These nano-engineered Si have succeeded in mitigating the stress derived from the volume variation and demonstrating the improved electrochemical performances of Si anode [75,84]. Nonetheless, the industrial application of such nano-architectures has been impeded on account of their low tap density, poor electrical properties, and low Coulombic efficiency (CE) derived from the large surface area available to form excessive SEI layer.

In consideration of practical implementation of the nano-Si anodes, incorporation of the Si into graphite has been highlighted as a rational strategy for high-energy density anodes, instead of the usage of Si-dominant material. In these composite electrodes, the graphite complements low electrical conductivity of Si with its good electrical conductivity and increases a tapping density of the composite owing to its micron-sized framework. Furthermore, it provides an excellent electrochemical stability and alleviates lithiation-induced volume expansion by diluting Si content as buffer matrix, resulting in improved battery performances. Additionally, the graphite, acting as lubricant, facilitates electrode calendaring of the composite, which is favorable to the attainment of high energy density in electrode scale.

In recent studies, a series of pioneering researches proposed notable Si–graphite composites fabricated by chemical vapor deposition (CVD) of gaseous Si precursor, which is advantageous to homogeneous deposition of high-quality Si nanolayer on the graphite surface and scalable synthesis [35,67]. According to these reports, the Si–graphite composites (including around 6 wt%

of Si content) were successfully demonstrated and they exhibited exceptional cycle stability with high reversible capacity (500 mAh g-1) and initial CE (92%). However, these Si–graphite composites suffer from limitation of Si content below around 6 wt%, otherwise excessive deposition of Si causes thickened Si nanolayer on graphite, leading to accelerating performance degradation with attenuating the merits of nano-sizing. Herein, we introduce unique design of Si nanolayer embedded macroporous carbon architecture on graphite for advanced Si-graphite composite anode using a simple SiO2 template and CVD methods. This design enables much Si content over 6 wt% in Si-graphite composite anode without significant deterioration. As a result, we have achieved next levels of lighter and denser anode material; 665 mAh/g (gravimetric), 3.5 mAh/cm2 (areal), and 1011 mAh/cm3 (volumetric) with 95.6% retention at 50th cycle.

2.2 Experimental detail

Preparation of CSMG and CSG.

The synthesis of CSMG composite starts from violently mixing of SiO_2 nanoparticles (200-300 nm), pitch, and spherical natural graphite. Mixing was conducted by revolution-rotation mixer. During the mixing, a small amount of tetrahydrofuran (THF) was added and mixed until the THF evaporated by frictional heat. Note that THF is very toxic solvent so mixing process should be conducted under fume hood. The mixed sample was loaded into a tube furnace. For carbonization of pitch, the sample was annealed under nitrogen atmosphere. The heating temperature was raised to 300 ℃ with ramping rate of 3 ℃/min and 3 hours of duration time, and then it is raised to 900 ℃ with ramping rate of 10 ℃/min and 1 hour of duration time. After heat treatment, the SiO_2 template was etched in 5M NaOH solution for 10 hours. To collect the powder, etched solution was filtered with distilled water until pH of filtered solution would be neutral. The collected MG powder was dried at 120 ℃ vacuum condition for 5 hours. To obtain homogeneous deposition of Si on each graphite and MG powder, high-purity silane gas (99.9999%) was streamed at a low flow rate of 50 cm^3/min for 70 min (graphite) and 50 cm^3/min for 45 min (MG) . Carbon coating was carried out with the same mixing method for formation of C and SiO2 covered graphite by only pitch. The coated carbon ratio was 6 wt% of the SMG sample.

Electrochemical characterization.

The electrodes were made by slurry casting on a copper current collector. The electrode composition was active material (CSMG, CSG, and silicon nanoparticle-graphite blending), sodium carboxymethyl cellulose (CMC), styrene butadiene rubber (SBR), and carbon black (Super-P, TIMCAL) = 95: 2: 2: 1 (weight/weight). The loading levels of electrodes were adjusted to achieve 3.5 mAh/cm2. The electrodes were dried at 80 ℃ for 2 h, and then pressed to achieve electrode density over 1.6 g/cm3. Immediately before coin cell assembly, the electrodes were vacuum-dried at 110 ℃ for 6 hours. 2032 coin-type cells are used for half- and full-cells assembly in an argon-filled glove box. The electrolyte was 1.3M LiPF6 in ethylene carbonate/diethyl carbonate (3:7 vol%) with 10% fluoroethylene carbonate (Panax Starlyte) and microporous polyethylene (15 μm, Celgard) was used as a separator. The voltage window of half-cells was 0.01-1.5 V for the formation cycles and 0.01-1.0 V for the rest of the cycles. A TOSCAT-3100 battery cycler (TOYO SYSTEM) was used for cycle test and a WBCS3000 cycler (WonAtech) was used for GITT test.

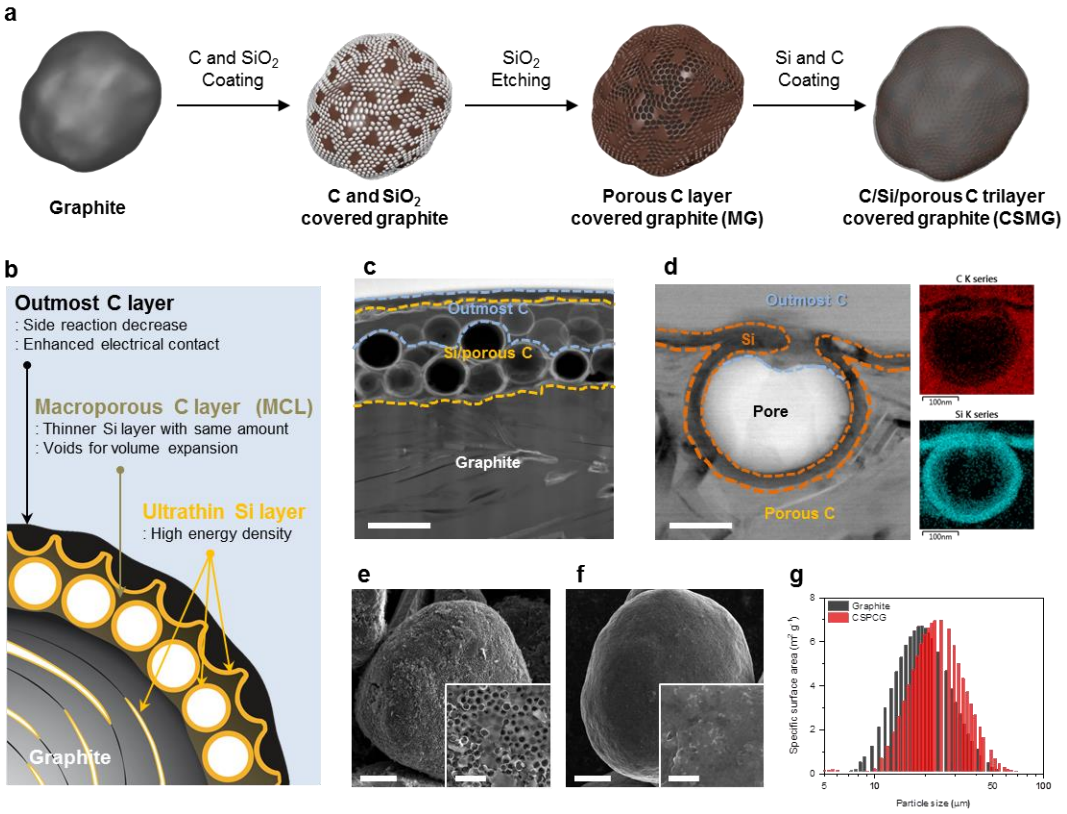

Figure 16. (a) Schematic view of synthetic process for CSMG. (b) Schematic view of unique features of CSMG. (c) STEM image of CSMG. (d) magnified STEM image of Si nanolyer and pore in CSMG with EDS mapping. (e) SEM images of MG. (f) SEM images of CSMG. (g) particle size distribution of pristine graphite and CSMG (Scale bar = 0.5 μm for (c), 100 nm for (d), 5 μm and 1 μm for (e) and (e)'s inset respectively, and 5 μm and 1 μm for (f) and (f)'s inset respectively.)

2.3 Results and discussion

Figure 16 illustrates the synthetic process of our designed Si-graphite composite. Each step-by-step Scanning Electron Microscopy (SEM) images are in figure 17. Initially, pitch and SiO_2 nanoparticles (diameter = 200~300 nm) [85,86] were assembled with pristine graphite via reveolution-rotation mixing as roles of carbon precursor and template. After subsequent carbonation of assembled composite, C and SiO_2 covered graphite was formed and SiO_2 nanoparticles were etched with 5M NaOH solution [87-91] which is relatively easy to handle compared to widely used etchant hydrofluoric acid (HF) because HF has irritating odor but NaOH solution is odorless [92,93]. Residual NaOH was totally washed with distilled water after etching. As a last step, Si nanolayer was homogenously distributed on macroporous carbon layer (MCL) covered graphite via CVD silane deposition method and carbon coating was conducted via pitch mixing & annealing method which is same method for construction of MCL (Detailed synthetic method is described in supplementary information). Note that pitch couldn't be completely infiltrated into inner pores of MCL during outmost carbon coating. In other words, the pores in MCL were maintained even after carbon coating. This will be shown in later section.

The size of SiO_2 and pitch/SiO_2 ratio were determined via empirical approaches; the diverse size and ratios such as average sizes of 150, 250, and 350 nm and ratios of 1:1, 1:2, 1:3, 1.25:3 and 1.5:3 were testified for optimization of MCL. Figure 18 showed SEM images of SiO2 nanoparticles and MGs (with pitch/SiO2 ratio = 1/2) depending on size of SiO2. The pore size in MGs was settled by the size of SiO2. The MG using 350 nm templates didn't well form MCL more than MGs using 150 and 250 nm templates (figure 18). Although MG using 150 nm templates well formed MCL, the pores in MCL were blocked after CVD silane coating (figure 19). Therefore we decided 250 nm templates were optimized size for pore control of MCL. Figure 20 summarized optimization process of pitch/SiO2 ratio. The SEM images of each ratio were shown in figure 33. As the absolute amounts of pitch and SiO2 increased, the BET surface area of the MCs increased (figure 21). However, the coating ratio exceeded 1.5:3 couldn't proceed due to particle aggregation . Thus, we concluded that 1.5:3 was the optimal ratio, and the latter experiment proceeded with this ratio. Note that the ratio optimization was done with same experimental method, and then the surface area of the final MC was slightly increased over 8.6 m2/g with technical advancement.

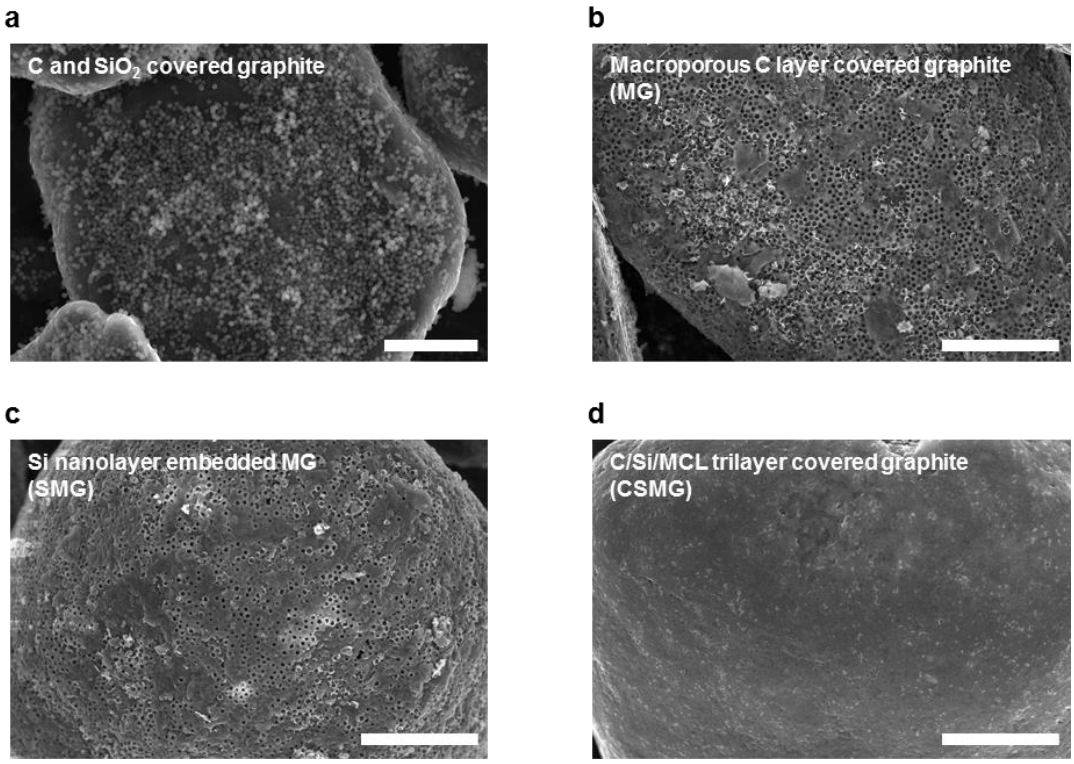

Figure 17. SEM images of (a) C and SiO_2 covered graphite, (b) MG, (c) SMG, and (d) CSMG (Scale bar = 5 μm)

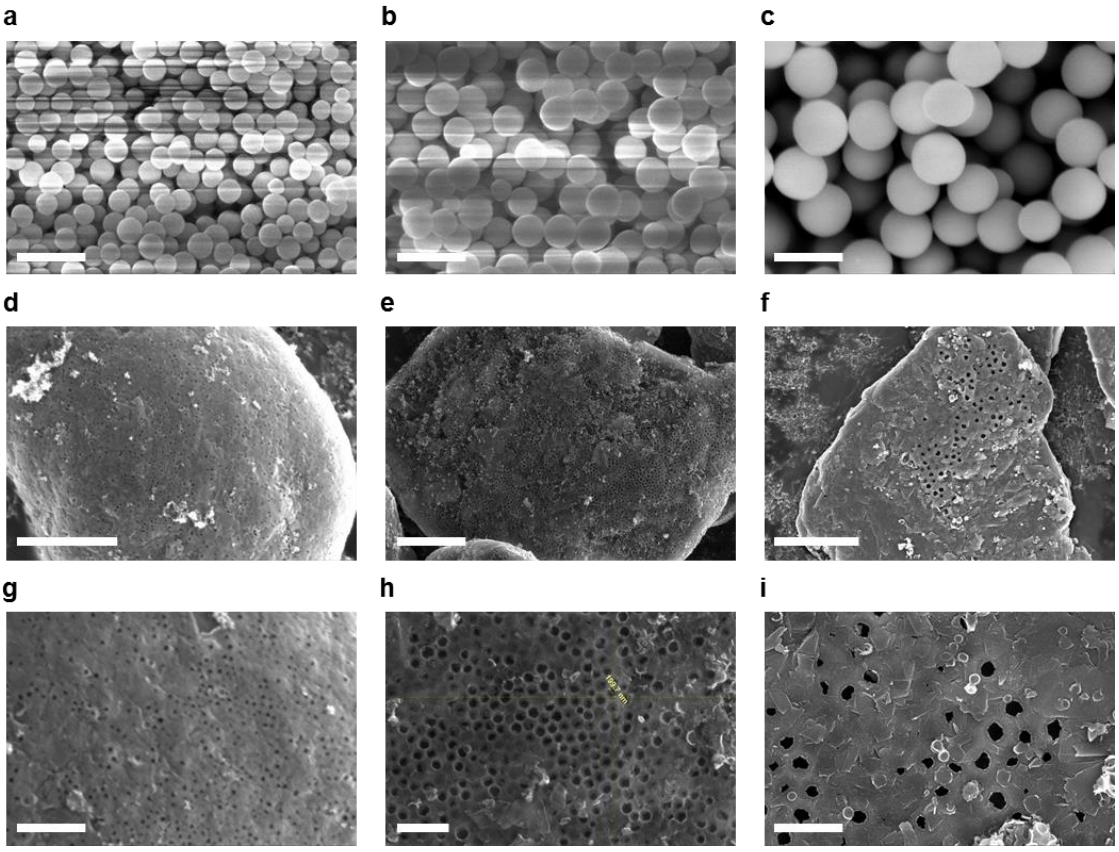

Figure 18. SEM images of (a) 100-200 nm SiO_2, (b) 200-300 nm SiO_2, (c) 300-400 nm SiO_2, (d) MC by using 100-200 nm SiO_2, (e) MC by using 200-300 nm SiO_2, and (f) MC by using 300-400 nm SiO_2, Magnified SEM images of (g) MC by using 100-200 nm SiO_2, (h) MC by using 200-300 nm SiO_2, and (i) MC by using 300-400 nm SiO_2. (Scale bar = 500 nm for (a), (b), and (c), 3 μm for (d), 5 μm for (e) and (f), and 1 μm for (g), (h), and (i))

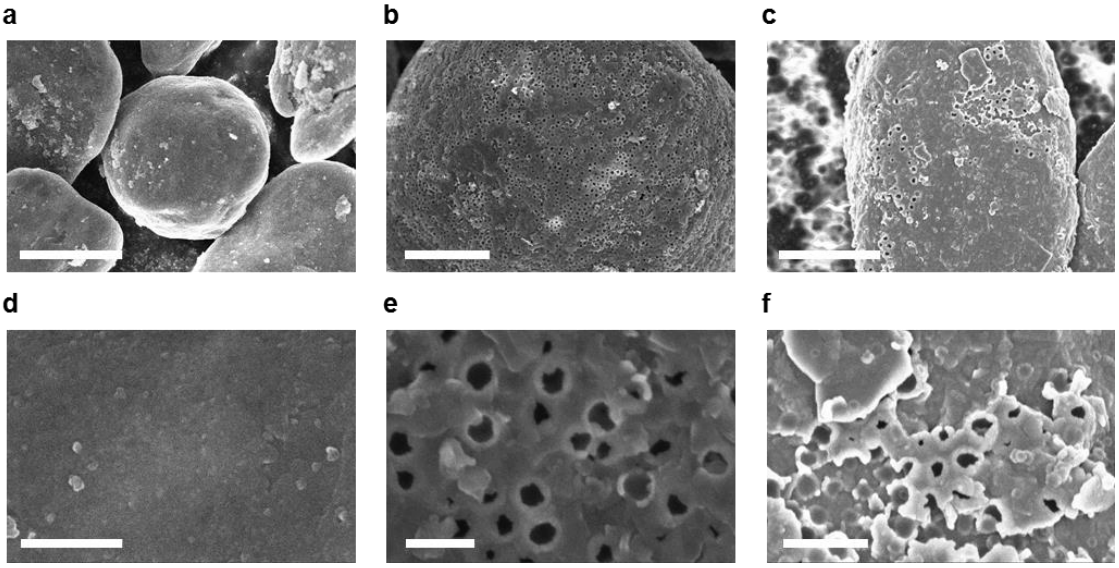

Figure 19. SEM images of (a) SMC by using 100-200 nm SiO_2, (b) SMC by using 200-300 nm SiO_2, (c) SMC by using 300-400 nm SiO_2. Magnified SEM images of (d) SMC by using 100-200 nm SiO_2, (e) SMC by using 200-300 nm SiO_2, (f) SMC by using 300-400 nm SiO_2 (Scale bar = 10 μm for (a), 5 μm for (b) and (c), 1 μm for (d), 500 nm for (e), and 1 μm for (f)).

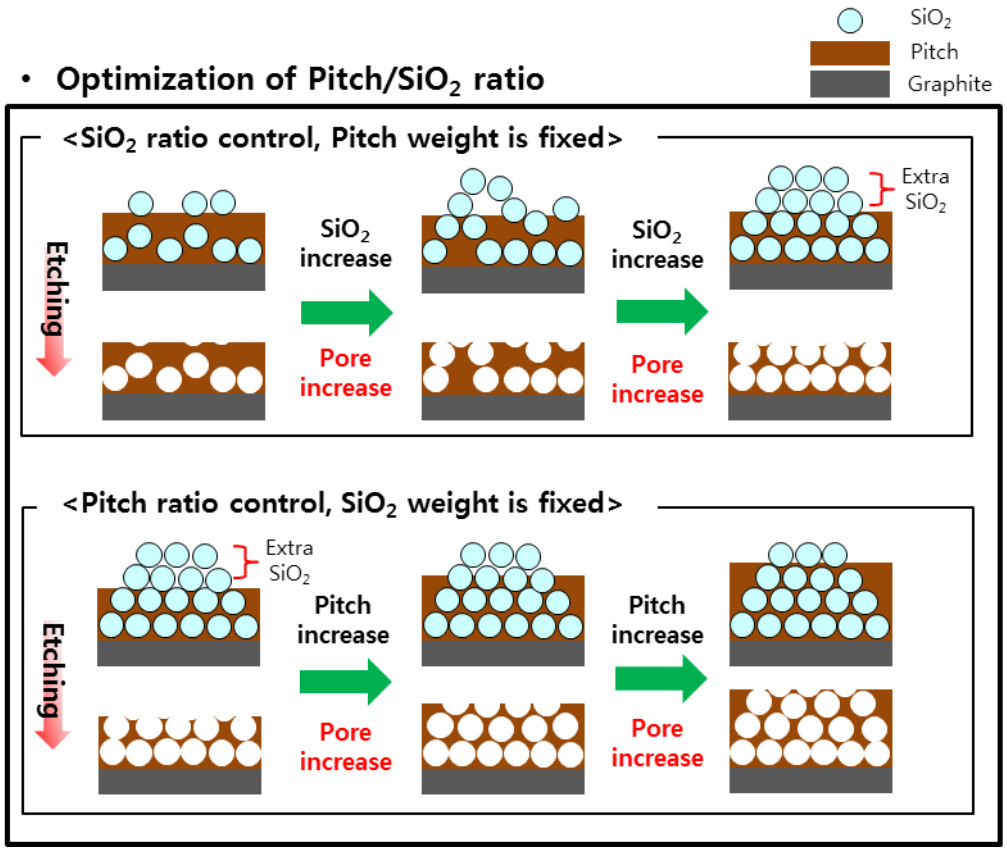

Figure 20. Summary of optimization process for pitch/SiO_2 ratio

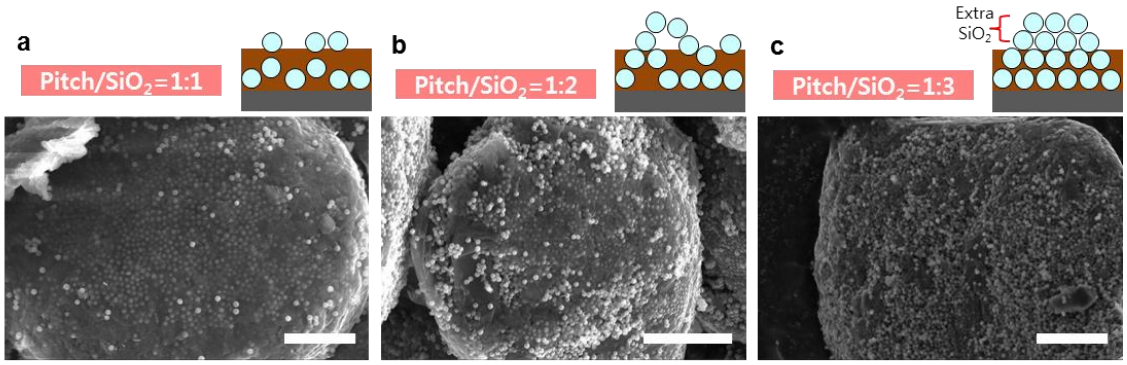

f

Pitch/SiO_2	BET (m^2 g^{-1}) (MGs)
1:1	5.3
1:2	6.5
1:3	7.0
1.25:3	7.4
1.5:3	8.6

Figure 21. SEM images of C and SiO_2 covered graphite depending pitch/SiO2 ratio (a) 1: 1, (b) 1: 2, (c) 1: 3, (d) 1.25: 3, (e) 1.5: 3, and (f) BET surface area depending on pitch/SiO_2 ratio (Scale bar = 5 μm for (a), (b), and (c) and 10 μm for (d) and (e))

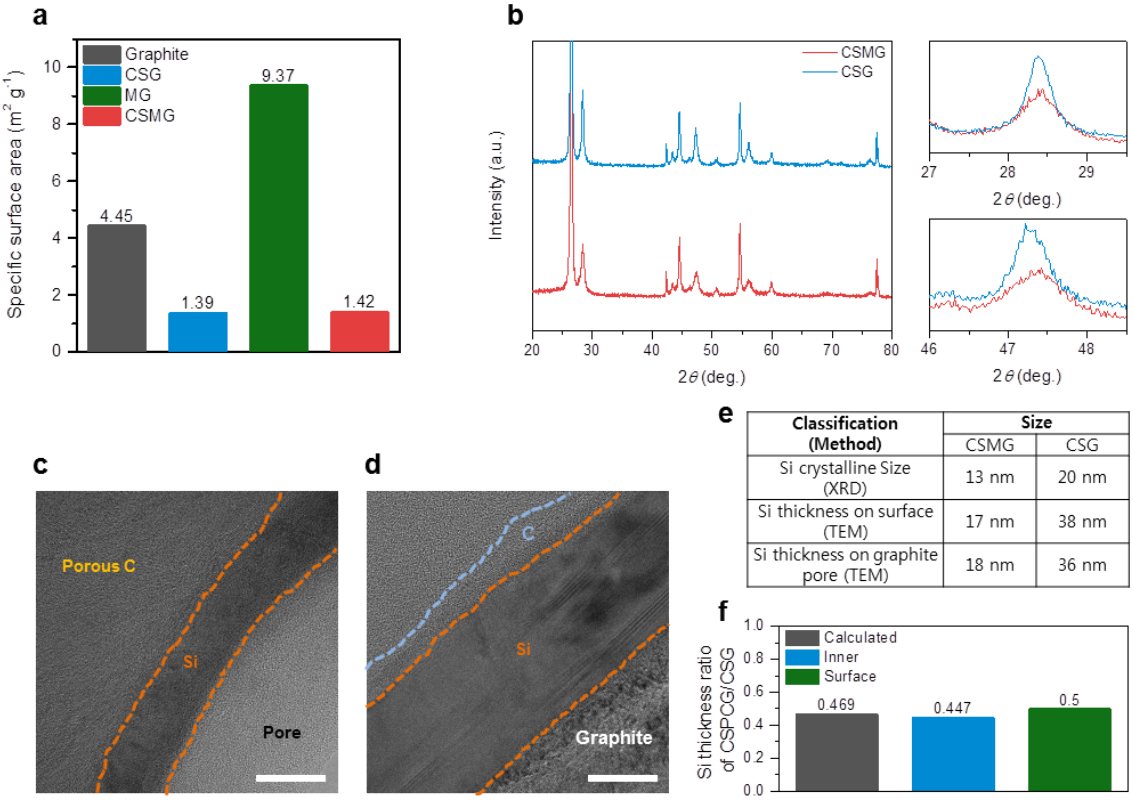

Classification (Method)	Size	
	CSMG	CSG
Si crystalline Size (XRD)	13 nm	20 nm
Si thickness on surface (TEM)	17 nm	38 nm
Si thickness on graphite pore (TEM)	18 nm	36 nm

Figure 22. (a) surface area of pristine graphite, CSG, MG, and CSMG. (b) XRD patterns of CSMG and CSG. (c) TEM image of CSMG. (d) TEM image of CSG. (e) Summary of size of Si nanolayer in CSMG and CSG. (f) Si thickness ratio of CSMG/CSG. (Scale bar = 20 nm for (c) and (d))

The designed features of final sample; C/Si/macroporous C trilayer covered graphite (CSMG) was summarized in figure 16b. The CSMG structure has three distinctive features; 1) MCL, 2) Ultrathin Si layer, and 3) Outmost C layer. It is different form from conventional layer by layer structures which are simply stacked. The ultrathin Si layers were embedded on MCL and surface of this composite was totally wrapped by outmost C layer. The roles of MCL is affording large surface area which could reduce Si nanolayer thickness even with same Si ratio in Si-graphite composite materials and its voids provided enough space for Si volume expansion. The ultrathin Si nanolayer on the MCL enables higher energy density compared to conventional graphite anode and previously reported Si nanolayer embedded graphite. Although Si content in CSMG was more than 9 wt% grounded on its reversible capacity, the thickness maintained an ultrathin shape and was beneficial for volume expansion. This topic will be meticulously described on later section with figure 22. The outmost C layer smoothened the surface of the CSMG without blocking the pores of MCL. It has roles of decreasing side reactions, at the same time enhancing electrical contacts between particles.

Figure 16c and d supported the described distinct morphologies of each part. They clearly showed components of CSMG; core graphite, Si nanolayer embedded MCL (SMCL), and outmost C was wrapping and overlapping with SMCL structure. The void space was maintained even after outmost C coating (figure 16d). The curvature surface of MG and smoothened surface of CSMG were clearly observed via SEM images (figure 16e and f) and there was no significant change of particle distribution between pristine graphite and CSMG (figure 16g). This means our surface treatment for Si and C design construction does not meaningfully alter the physical properties of pristine graphite for preparation of electrode fabrication.

To specifically investigate impacts of MCL, we synthesized reference Si-graphite composite sample which shows almost same reversible capacity (it means same Si ratio) but doesn't have MCL structure. The reference sample was synthesized via CVD silane coating on pristine graphite and subsequent outmost C coating. Hence, it is carbon coated Si nanolayer embedded graphite (CSG). Primarily, we compared the BET surface of pristine graphite and MG. The MCL dramatically increased the BET surface of 4.45 m2/g (pristine graphite) up to 9.37 m2/g (MG) (figure 22a). The increased BET surface was decreased down to 1.5 m2/g after final synthetic steps of Si and C coating.

The crystal structure of Si nanolayer was investigated by X-ray diffraction (XRD). The (111) and (220) crystalline Si peaks of CSMG showed lower intensity compared to those of CSG, that is Si crystalline size of CSMG was smaller than that of CSG [94,95]. The crystalline size calculation via the Scherrer equation represented 13 and 20 nm for CSMG and CSG respectively [96-98]. The Si nanolayer thicknesses were directly observed by Transmission Electron

Microscopy (TEM) (figure 22c, d and 32). The Si thicknesses on surface were 17 and 38 nm, and those on graphite inner pore were 18 and 36 nm for CSMG and CSG respectively (figure 22 and 23). The crystalline sizes and thicknesses of Si nanolayers were summarized in figure 22e. It represented the existence of MCL reduced the Si thickness by almost half. We also compared Si thickness with reported values. Previous Si nanolayer embedded graphite concepts showed 16~18 nm of Si nanolayer for 517~525 mAh/g of reversible capacity. However, herein we maintained 17~18 nm of Si thickness even increasing reversible capacity over 650 mAh/g.

To figure out the relationship between deposited Si layer thickness and surface area, we compared calculated Si thickness ratio of CSMG/CSG based on the BET surface areas of Si coating target materials (MG and graphite) and measured Si thickness ratio of CSMG/CSG (figure 22f) (The detailed calculation method is on supplementary information). The calculated and measured (inner and surface) Si thickness ratios of CSMG/CSG were 0.469 (calculated), 0.447 (inner measured), and 0.5 (surface measured). The calculated values were no different than the differences between the measured values. That is, the calculation based on BET surface area corresponds to the actual value, which means that BET surface area is the most important factor in determining the deposited Si thickness.

Figure 24a and b describe lithiation mechanisms of CSMG and CSG. We designed a novel MCL included Si-graphite composite, in which the Si layer is ultrathin and enough void space is provided. In this design, since the expansion of the Si layer is smaller due to ultrathin size and the direction of the expanded Si is void space, the expansion at the particle level could be minimized (figure 24a). In contrast, the CSG is the structure in which Si is merely superimposed on surface of graphite, causing a larger expansion and resulting in cracks between Si and graphite and between Si and coated carbon (figure 24b). Figure 24c-h showed TEM/Scanning TEM (STEM) images of pristine and lithiated CSMG and CSG. To extract the lithiated electrodes, the charged 2032 coin cells of CSMG and CSG electrodes were opened in dry room and the lithiated CSMG and CSG were transferred to Focused Ion Beam (FIB) for sampling and TEM for sample observation as sealed state to minimize water & air exposure. Figure 24c and f were TEM images of CSMG and CSG already shown in figure 22c and d. To clearly compare the Si and Li-Si layer thicknesses, we observed with STEM-annular dark field (ADF) imaging mode, which is highly detectable for the different atoms in the samples. The Si layer thicknesses in pristine CSMG and CSG were 18 and 42 nm in STEM-ADF images (figure 3d and g) and after lithiation (0.1C charge until 0.01V and constant voltage mode until 0.01C) Li-Si layer thicknesses expanded to 23 and 69 nm (figure 24e and h). The variation of Si layer thickness was much larger in CSG due to Si size effect and there was a crack between Li-Si and graphite in lithiated CSG due to large volume expansion. In contrast, the Li-Si layer in lithiated CSMG didn’t show any crack beside the Li-Si layer. The electrode scale expansion will be mentioned in

later section.

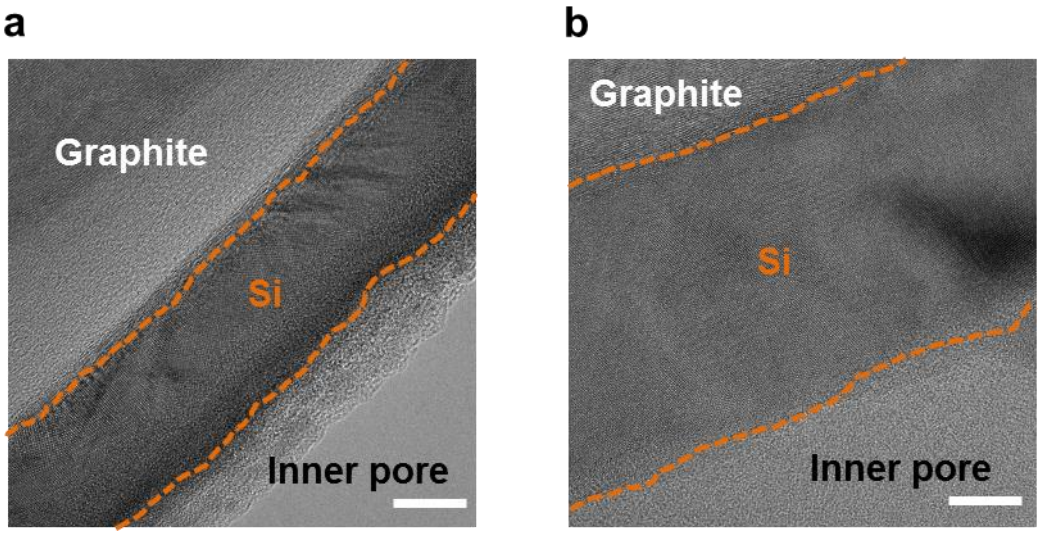

Figure 23. TEM images of Inner part of (a) CSMG and (b) CSG (Scale bar = 10 nm).

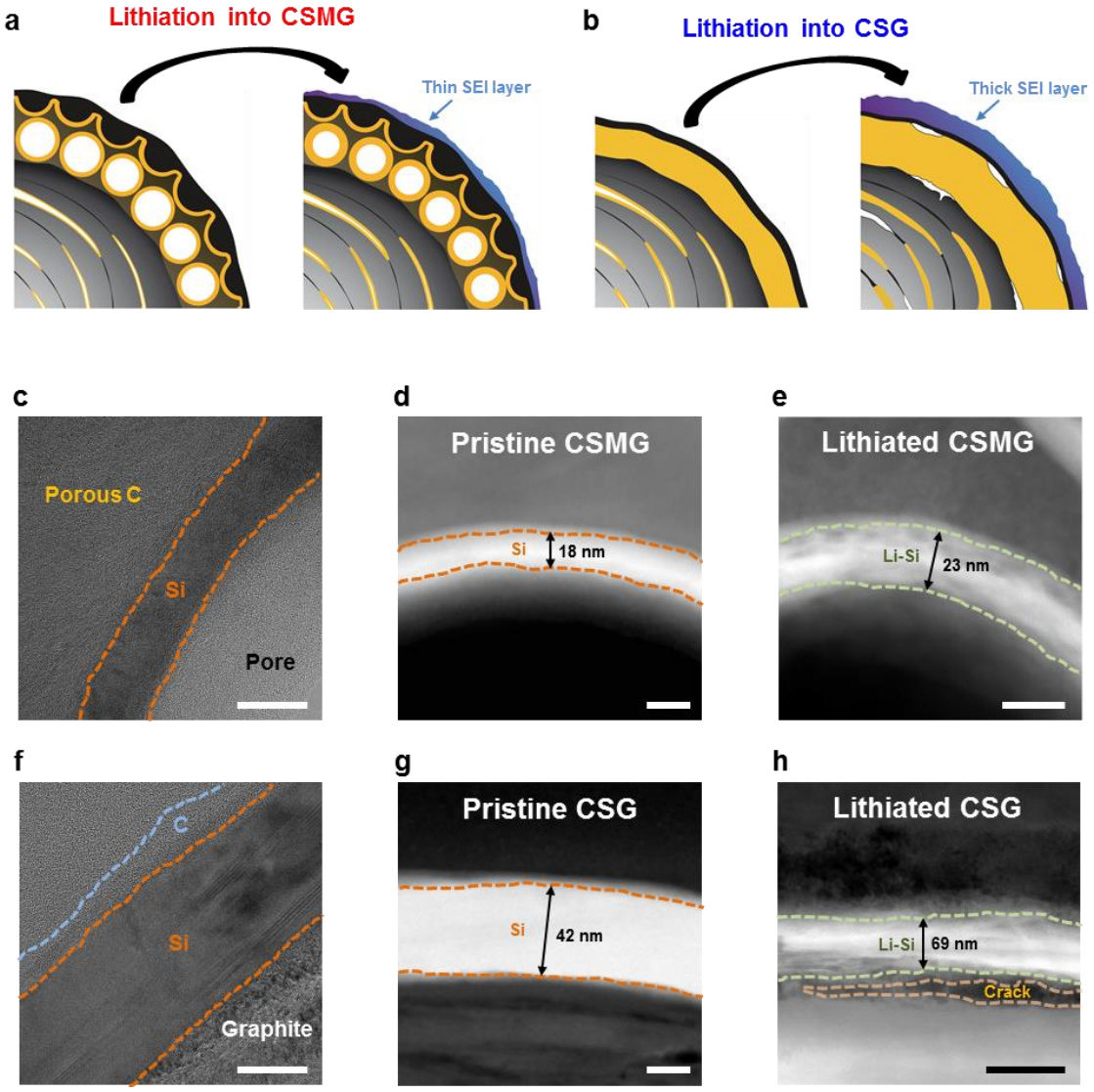

Figure 24. Schematic view of lithiation process of (a) CSMG and (b) CSG. Reproduced TEM images from figure 22, TEM image of (c) CSMG and (f) CSG. STEM-ADF images of (d) pristine CSMG, (e) lithiated CSMG, (g) pristine CSG, and (h) lithiated CSG. (Scale bar = 20 nm for (c), (d), (e), (f), and (g), and 100 nm for (h))

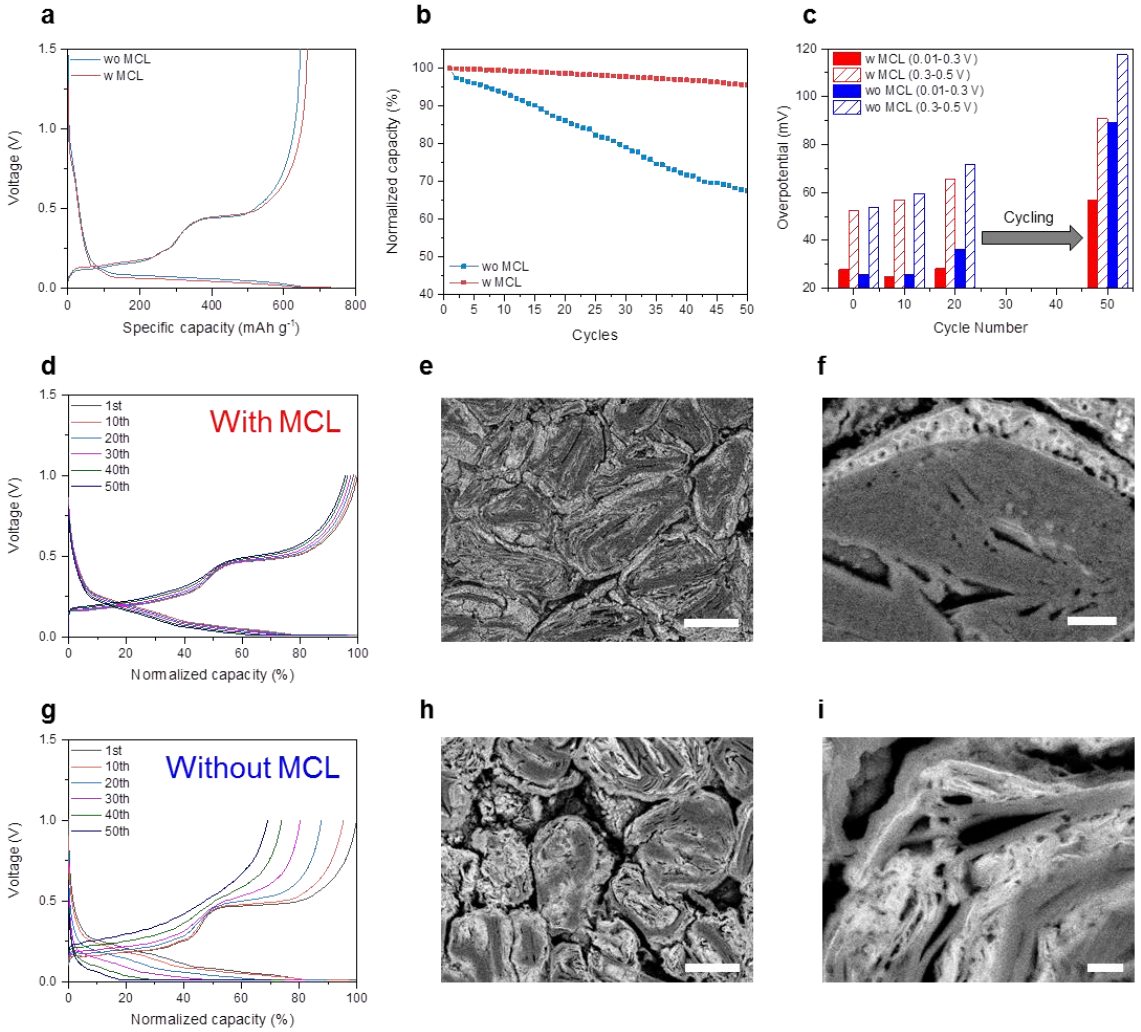

Figure 25. (a) First cycle voltage profiles of CSMG and CSG. (b) 0.5C cycle graphs of CSMG and CSG. (c) Overpotentials measured via GITT depending on cycle number. (d) Voltage profiles of CSMG during cycling. (e) Cross sectional SEM image of CSMG electrode after 50th cycle. (f) Magnified cross sectional SEM image of CSMG electrode after 50th cycle. (g) Voltage profiles of CSG during cycling. (h) Cross sectional SEM image of CSG electrode after 50th cycle. (i) Magnified cross sectional SEM image of CSG electrode after 50th cycle (Scale bar = 10 μm for (e) and (h), and 1 μm for (f) and (i)).

To explore electrochemical properties of CSMG as anode materials for lithium ion batteries, we prepared electrodes and assembled 2032 half coin cells (detailed process is on method section). The electrode composition was active material: super-P: CMC: SBR = 95: 1: 2: 2 and mass loading and density were 5 mg/cm2 and 1.6 g/cc respectively. The charge/discharge rate was 0.1C rate for formation and 0.5C rate for cycle. The cut-off voltage was 0.01-1.5V for formation and 0.01-1.0V for rest of cycles. The cut-off c-rate for constant voltage mode was 0.01C rate. The 1st reversible capacities of CSMG and CSG were 665 and 646 mAh/g and their initial coulombic efficiencies (ICE) were 90.9 and 90.1% (figure 25a). The electrode volume expansion of CSMG and CSG were 42 and 70% after formation. At subsequent cycling test, CSMG and CSG showed 95.6 and 67.6% retention and the electrode volume expansion of CSMG and CSG were 64 and 89% at 50th cycle (figure 25b). The lower volume expansion of CSMG electrode was resulted from ultrathin Si layer, void space, and buffer matrix induced by MCL.

For comparison with commercial anode materials, we testified Si nanoparticle and graphite blending (SGB) electrode with same conditions for CSMG and CSG. The 1st reversible capacity of SGB was 657 mAh/g and its ICE was 90.2% (figure 26). The electrode volume expansion of SGB was 88% after formation. At subsequent cycling test, SGB showed 69.4% retention and the electrode volume expansion of SGB was 90% at 50th cycle (figure 26). SGB electrode showed comparable performance to CSG, which means that the CSG concept is not as effective as SGB for Si-graphite mixed system of 650 mAh/g.

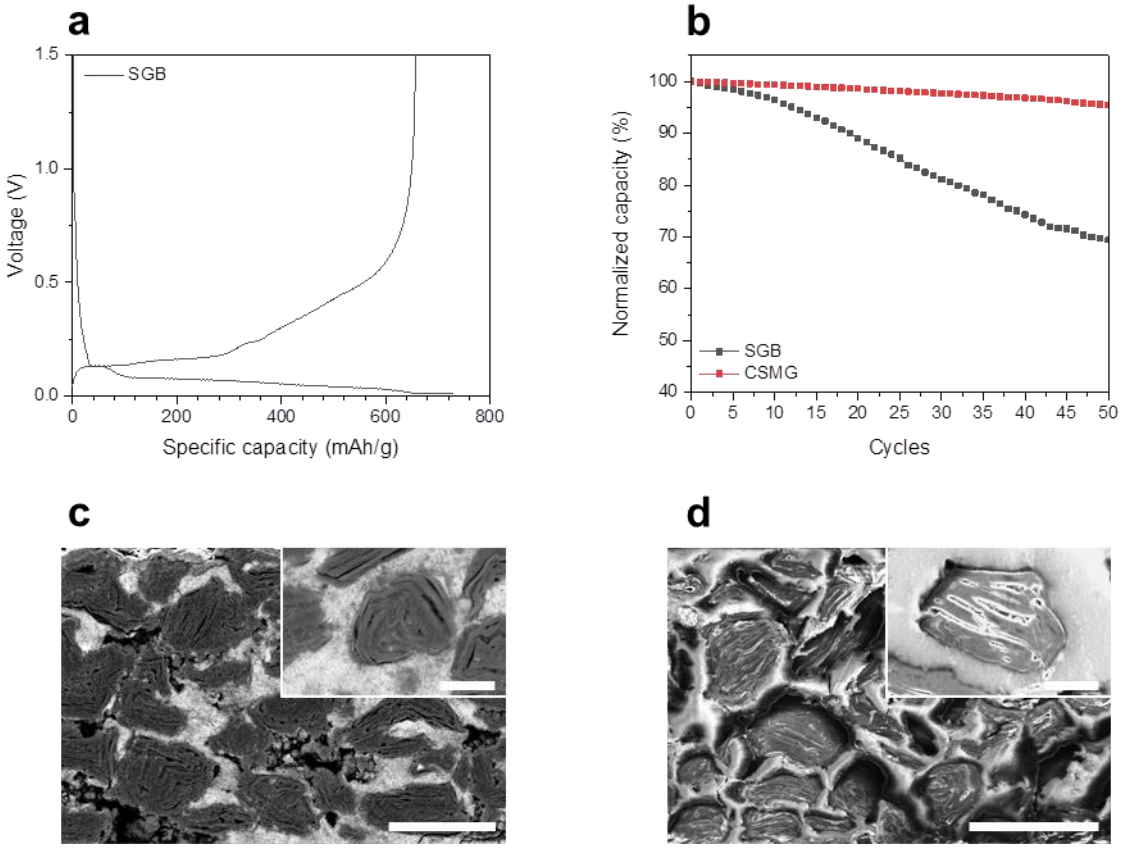

Figure 26. (a) Voltage profile of SGB at 1st formation. (b) 0.5C cycle test of SGB with CSMG. (c) Cross sectional SEM images of SGB electrode after formation (lithiated state). (d) Cross sectional SEM images of SGB electrode after 50th cycle (delithiated state) (Scale bar = 5 μm and 20 μm for (c) and (c)'s inset and 5 μm and 30 μm for (d) and (d)'s inset respectively).

To measure the increases of internal resistance, we conducted modified galvanostatic intermittent titration technique (GITT) for CSMG and CSG electrode [99,100]. Because of slight working potential difference among graphite, Si, and Li metal (graphite: 0.05 V, Si: 0.4 V, Li metal: 0 V), the lower cut off voltage for Si and graphite anode should be over 0 V to avoid lithium plating phenomenon which is one of the fading reasons of Si and graphite anode [18,101,102]. Hence constant voltage (CV) mode charging is generally accepted after constant current (CC) mode charging for full lithiation of anode materials[103-105]. In this context, the pulsed current of GITT couldn't induce full lithiation of anode materials. Therefore we devised the modified GITT method that is ordinary charging process which includes CC-CV mode and subsequent discharging process with the pulsed current (see the method for detailed process). As a result, we compared IR drops and overpotentials of CSMG and CSG at delithiation process and separated delithitions of lithiated graphite and Si by voltage ranges 0.01-0.3 V for lithiated graphite and 0.3-0.5 V for lithiated Si (figure 25c and 27). At 1st cycle, the overpotentials of CSMG and CSG were 28 mV (CSMG; 0.01-0.3 V), 53 mV (CSMG; 0.3-0.5 V), 26 mV (CSG; 0.01-0.3 V), and 54 mV (CSG; 0.3-0.5 V), and at 50th cycle, the overpotentials of CSMG and CSG were increased to 57 mV (CSMG; 0.01-0.3 V), 91 mV (CSMG; 0.3-0.5 V), 89 mV (CSG; 0.01-0.3 V), and 117 mV (CSG; 0.3-0.5 V) (figure 25). Overall, there was a large overpotential in the voltage range 0.3-0.5 V which is Li-Si reaction range, and the overpotential gap between CSMG and CSG increased as the cycle passed. The IR drops of CSMG and CSG showed the same trend of overpotentials (figure 27). The increased internal resistances could be also detected in increased and disappeared voltage plateau at voltage profiles depending on cycle number (figure 25d and g). The voltage profiles shape of CSMG were almost maintained from 1st to 50th cycle, however the voltage plateaus of CSG were raised up and disappeared gradually as cycle goes.

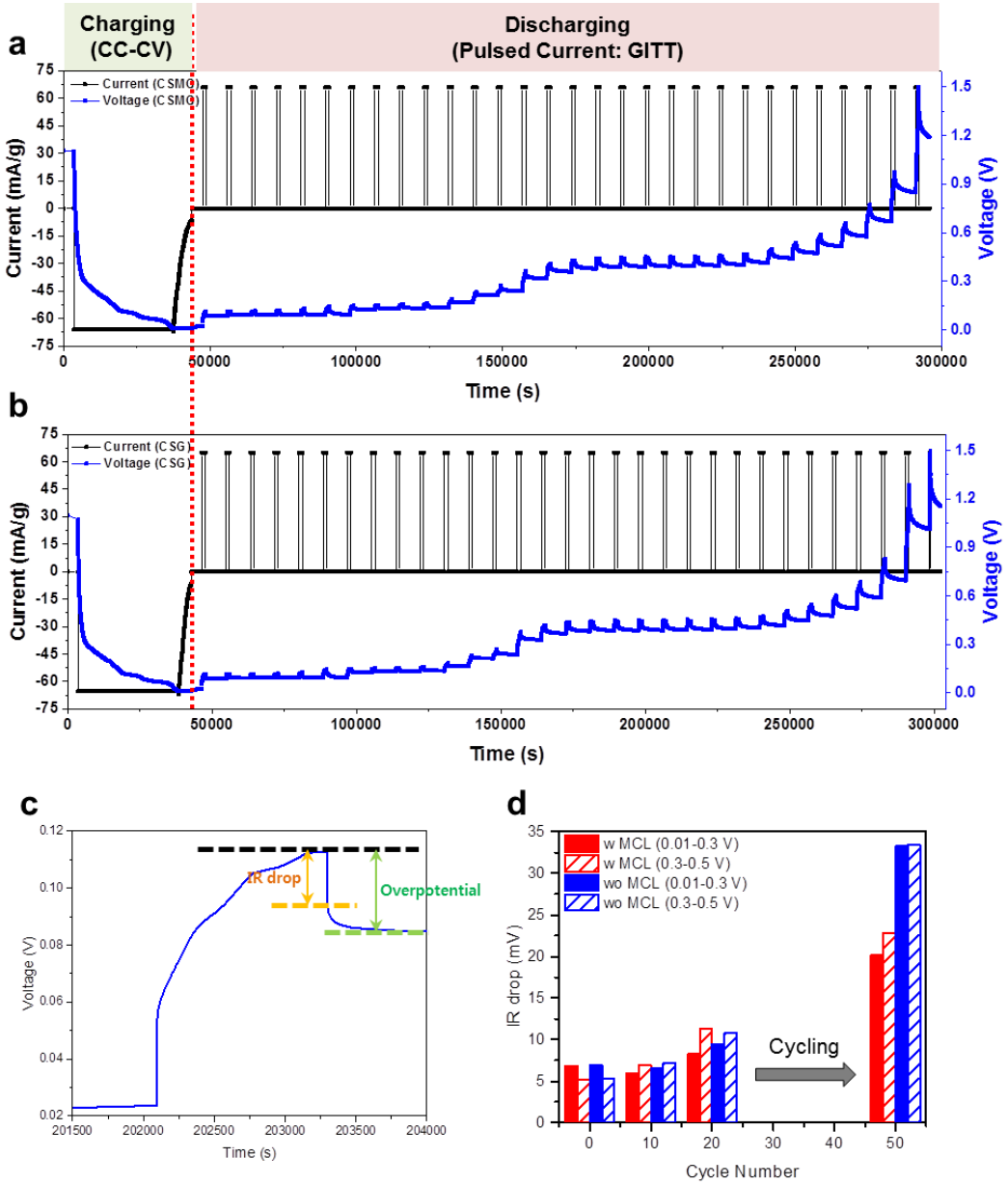

Figure 27. (a) Voltage and current profiles of CSMG during GITT test. (b) Voltage and current profiles of CSG during GITT test. (c) Magnified voltage response by pulsed current. (d) IR drops of CSMG and CSG measured via GITT depending on cycle number.

Figure 25e, f, h, and i showed cross sectional SEM images of electrodes after 50th cycle. There was a large crevice between the particles in CSG electrode, however there was no such a crevice in CSMG electrode after 50th cycle (figure 25e and h). In magnified cross sectional images of CSG electrode after 50th cycle, expanded Si layer peeled off from the graphite and graphite plates were released from tightly winded spherical state, inducing large crevice between plates. In contrast, there was no significant change in magnified cross sectional image of CSMG electrode. It demonstrated that MCL is a strategically advantageous structure for Si-graphite composite anode system.

2.4 Conclusion

In summary, we have developed synthetic method to raise Si ratio in Si-carbon-graphite composite without increase of crystalline size and Si layer thickness. Enlarged BET surface area due to MCL assisted ultrathin Si layer deposition of 17-18 nm. Its unique structure of Si layer embedded MCL on graphite composite was maintained even after outmost carbon coating. The pores in MCL and its robust carbon structure accommodated volume expansion of ultrathin Si layers. The gravimetric capacity of our product materials (CSMG) was designed for 665 mAh/g and the electrode was produced for 3.5 mAh/cm2 and 1011 mAh/cm3. The initial CE and the 50th retention of CSMG electrode were 90.9% and 95.6% respectively. The fading reasons were investigated by GITT and ex-situ SEM/TEM. GITT provide internal resistance change during cycle life. Consequently, we proved our designed morphology was effective to reduce increasing of internal resistance induced by SEI growth during cycling and also confirmed CSMG structure maintained its morphology even after 50th cycle. We believe this strategy will enable higher gravimetric capacity (> 650 mAh/g) of Si-graphite composite materials, opening new class of light and dense anode materials in lithium ion batteries industry.

Chapter 3

C/Si nanolayer/C micron cage
: Silicon-carbon composite for > 1000 mAh/g anode materials

3.1 Introduction

Pseudocapacitance is the electrochemically charging/discharge mechanism bridging from double layer capacitors to lithium ion batteries (LIBs) [106]. Electrical energy of pseudocapacitor is faradaically stored within redox active materials. The faradaic reaction in pseudocapacitor enables higher energy density compared to non-faradaic reaction in double layer capacitors and pseudocapacitive reaction wouldn't be limited by sluggish solid state diffusion like lithium (Li) ion diffusion in active materials of LIBs. Conventional pseudocapacitive materials such as ruthenium oxide, manganese oxide, titanium carbide and etc. were mostly operated in aqueous electrolyte[107-109]. However recently pseudocapacitive materials based on nonaqueous Li ion electrolyte have been studied to overcome energy density limitation of capacitors and kinetic limitation of LIBs. Reported pseudocapacitive materials using nonaqueous Li ion electrolyte were Nb2O5, LixMn2O4, Mn2O3, Sn and etc[110-113]. These works were evaluated with thin film-type electrode. However, preparation methods of thin film-type electrode are not appropriate for LIBs industry because of process complexity, ultralow loading level, and high cost. Therefore, succeeding researches require designed pseudocapacitive materials enabling conventional slurry casting method of electrode preparation.

Here, we established silicon (Si) nanolayer embedded carbon (C) micron cage structure gratifying prerequisites for next pseudocapacitive materials. To the best of our knowledge, this is the first investigation on pseudocapacitive behavior of Si based materials. We evaluated whether Si could be pseudocapacitive minimizing its diffusion length for Li-Si alloying reaction and confirmed superior rate capability as pseudocapacitive capacity ratio was increased. On the other side, although Si is the most promising anode materials for LIBs because of its large theoretical capacity, volume expansion of Li-Si alloying reaction involving dramatic capacity fading is impeding extensively usage of Si materials in LIBs industry[17,68,81,114-116]. Thus, we intended three dimensional pores provided enough void space for volume expansion and it was proved there weren't particle scale expansion in the designed Si-C composite via in situ SEM analysis.

3.2 Experimental detail

Preparation of CSMC

SiO_2 nanoparticles template was synthesized according to literature[117]. Prepared SiO2 nanparticles and pitch were mixed with 3:1 weight ratio. 12 g of the mixed powder was well dispersed in 0.6 L of tetrahydrofuran (THF) by sonication (Use sonication with the mixed solution in closed bottle). Under stirring, the mixed solution was sprayed and dried via spray dryer (Mini Spray Dryer B-290, BUCHI Labortechnik) at 120 ℃. Collected spray dried powder was heated in a tube furnace under nitrogen atmosphere. Firstly, heating temperature was raised to 300 ℃ with ramping rate of 3 ℃/min and 3 hours of duration time, and then it is raised to 900 ℃ with ramping rate of 10 ℃/min and 1 hour of duration time. After heat treatment, the SiO2 template was etched in 3M NaOH solution for overnight. To collect MC powder, etched solution was filtered with distilled water until pH of filtered solution would be neutral. Collected MC powder was dried at 80 ℃ vacuum condition for overnight.

To obtain homogeneous Si nanolayers on each MC powder, high-purity silane gas (99.9999%) was flowed at a low flow rate of 50 cm3/min for 6 min (SMC600), 11 min (SMC1200), and 25 min (SMC2000). The decomposition temperature was maintained at 475 ℃. 15wt% of carbon coating was carried out with pitch solution (solvent: THF). After physical mixing of pitch solution and SMC powder, solvent was evaporated and then same heat treatment for MC powder was conducted (After heat treatment, actual coated carbon ratio was expected to 9wt%).

Material characterization

Structural and chemical properties of samples were investigated by scanning electron microscopy (SEM; Verios 460, FEI), Raman (NRS-5000, JASCO), X-ray diraction (D/Max 2200, Rigaku), and transmission electron microscopy (TEM; JEM-ARM300F, JEOL). To observe cross sectional images of samples, two cutting methods were utilized: The first method was using ion-milling system (HITACHI IM4000, Hitachi High-Technologies) for SEM sample preparation and the other method was using dual-beam focused ion beam (FIB), (Helios NanoLab 450, FEI) for TEM sample preparation. To minimize the sample damage from FIB process, the samples were treated by protective substance before sampling.

Electrochemical characterization

The electrode was fabricated by conventional slurry mixing and casting method on copper current collector. The electrode compositions are active material (MC, CSMC600, CSMC1200, CSMC2000, and Silicon nanoparticles (SiNPs; Alfa Aesar)), carbon black (Super P, TIMCAL),

carboxymethyl cellulose (CMC), and styrene butadiene rubber (SBR) with mass ratio of 80:10:5:5. The loading level of electrodes was adjusted to achieve 1.2~1.5 mAh/cm2. The electrodes were dried at 80 ℃ for 1 hour and they were vacuum-dried at 110 ℃ for 6 hours right before cell assembly. Coin type 2032 cell was used for half and full cell assembly. The electrolyte was 1.3M LiPF6 in ethylene carbonate/diethyl carbonate (3/7 vol%) with 10% fluoroethylene carbonate (Panax Starlyte) and the separator was microporous polyethylene with a thickness of 20 μm. All the cell assembly was conducted in a glove box filled with argon gas. Cut-off voltage ranges for half cells were 0.01-1.5 V for formation two cycles and 0.01-1.0V for rest of cycles. C-rates were 0.1C for formations and 0.5C for cycles. Cut-off C-rate for constant voltage (0.01 V) mode was 0.01C (Only for charge process). The entire electrochemical test was carried out using a Wonatech WBCS3000 cycler. For full cell test, we used commercial lithium cobalt oxide (LCO) as a cathode material. The LCO electrode composition is LCO, carbon black (Super P, TIMCAL), polyvinylidene fluoride (PVDF) with mass ratio of 94:3:3. The loading level of LCO electrode was adjusted to achieve N/P ratio of ~1.1. The LCO electrode was dried at 100 ℃ for 2 hours. Cut-off voltage ranges for full cells were 4.2-2.5 V for formation two cycles and 4.2-2.7 V for rest of cycles. C-rates were 0.2C for formations and 0.5C for cycles. Cut-off C-rate for constant voltage (4.2 V) mode was 0.05C for formation and 0.1C for cycles.

Cyclic voltammetry and its derivatives

General cyclic voltammetry method was conducted for only SiNP electrode. Voltage scan range was 0.01-2.0 V. Scan rate range was 0.04-1 mV/s (0.04, 0.09, 0.16, 0.25, 0.36, 0.49, 0.64, 0.81, and 1 mV/s). Modified cyclic voltammetry; Charged linear sweep voltammetry (C-LSV) was conducted for SiNPs, MC, CSMC600, CSMC1200, and CSMC2000 electrode. In C-LSV method, charge process was carried out using constant current-constant voltage mode (cut-off: 0.01V and 0.01C) and discharge process was linear sweep voltammetry with sweep rate range of 0.04-1 mV/s (cut-off: 2.0 V). The plot; log(sweep rate) vs. log(peak current) and calculation of capacitive and diffusion controlled capacities were conducted according to literatures [110,118].

In situ SEM analysis

The in situ chemical characterization was carried out in an SEM with two nanomanipulators (MM4-EM, Kleindiek Nanotechnik). The nanomanipulator with tungsten (W) tip (diameter: 100 nm) was used to pick up the samples (CSMC600, CSMC1200, and CSMC2000) and lithium metal. To prevent formation of Li2O, lithium metal was scratched in SEM vacuum chamber. In order to accelerate spontaneous alloying reac tion, the W tip holding samples was contacted with the lithium metal strained W tip[119,120]. The contact was maintained until there was no

structural change at all. In situ SEM analysis was operated under accelerating voltage and emission current of 5.00 or 10.00 kV and 0.40 nA respectively.

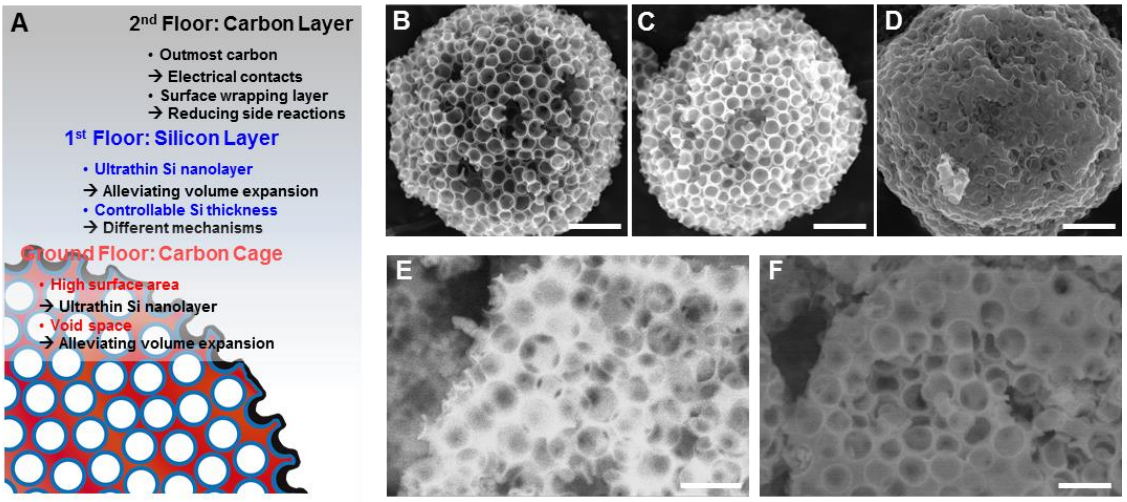

Figure 28. Proposed concepts of CSMC structure and roles of each features. (A) Schematic illustration of carbon-silicon nanolayer-carbon micron cage (CSMC) concepts. Red, blue, and black parts showed carbon cage, silicon layer, and carbon layer respectively. SEM images of (B) Carbon micron cage (MC), (C) Silicon nanolayer-carbon micron cage (SMC1200), and (D) CSMC1200. BSE images of cross-sectional (E) MC and (F) CSMC1200. Scale bar = 1 μm for B, C, and D, 500 nm for E and F.

3.3 Results and discussion

The designed features of proposed structure were described in figure 28A. The concepts came from imagination how to maximize surface area in micron size particles (micron size has advantages for electrode fabrication and materials packing[66]) for Si deposition, at the same time how to minimize the electrolyte exposed surface of Si. Based on the requirement, the final product was designed with three floors. The ground floor was macroporous carbon micro cage (MC) which had roles of substrate for Si deposition and it had void space alleviating volume expansion (red part in figure 28A). The first floor was ultrathin Si nanolayers which were mainly redox active material and its thickness could be controllable (blue part in figure 28A). The second floor was outmost wrapping carbon layers to reduce side reactions and enhance electrical contacts (black part in figure 28A).

The synthetic process of designed materials was described in figure 29. The first step of synthetic process was assembly of pitch and SiO2 nanoparticles via spray drying method (See the supplementary materials for detailed method, figure 29). The assembled sample was annealed at 900 ℃. After the annealing, SiO2 template was etched with NaOH solution and the sample was washed with distilled water. The SEM images of obtained MC are shown in figure 28B. The pore size was 200-300 nm, which was same size of SiO2 nanoparticles (figure 30). The X-Ray Diffraction (XRD) patterns and Raman spectrum revealed amorphous carbon structure of MC (figure 31) and the BET surface of MC was 69.31 m2/g. Though silane Chemical Vapor Deposition (CVD) method, the first floor; Si nanolayer was embedded on MC (SMC; figure 28C and 32). Depending on the CVD reaction time, the thickness of Si nanolayer was determined, which means gravimetric capacity of the product was controllable. We prepared three types of SMC series; SMC600, SMC1200, and SMC2000 depending on their gravimetric capacities. The second floor; outmost wrapping carbon layer was made by same pitch precursor composing the ground floor carbon substrate. Thus the final product was carbon wrapped SMC (CSMC; figure 28D and 33). To confirm the inner structures of MC and CSMC series, the samples were cut by ion-milling system and observed in scanning electron microscopy (SEM). The cross-sectional image of MC presented clear removal of SiO2 template (figure 28E) and those of CSMCs presented mostly preserved void spaces after outmost carbon layer, even though its surface was smoothened with outmost carbon layer (figure 28F and 34). Inner structure of CSMC was also detected via transmission electron microscopy (TEM). Figure 35 showed Scanning TEM (STEM) energy dispersive spectrometer (EDS) mapping of CSMC series. The void spaces were clearly observed in EDS mapping images.

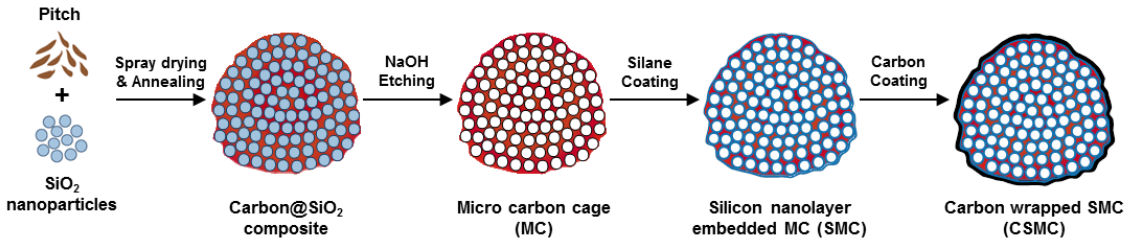

Figure 29. Schematic view of synthetic process.

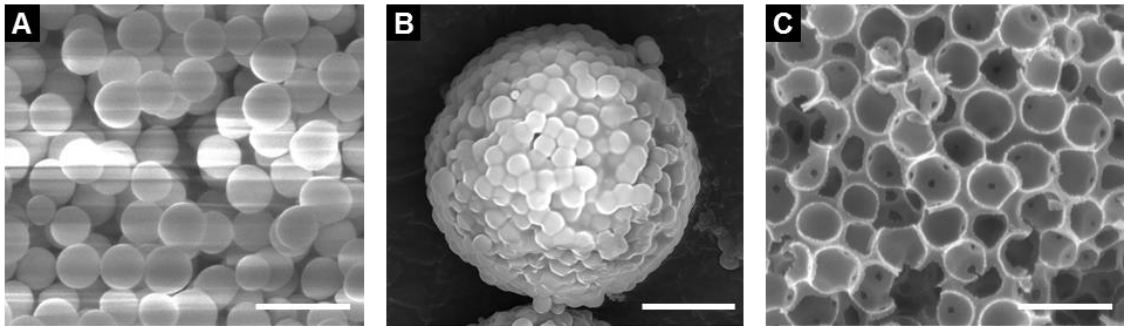

Figure 30. Comparison between templates and produced pores. SEM image of (A) SiO_2 nanoparticles, (B) Carbon@SiO_2 composite and (C) pores in MC. Scale bar = 500 nm for A and C, 2 μm for B

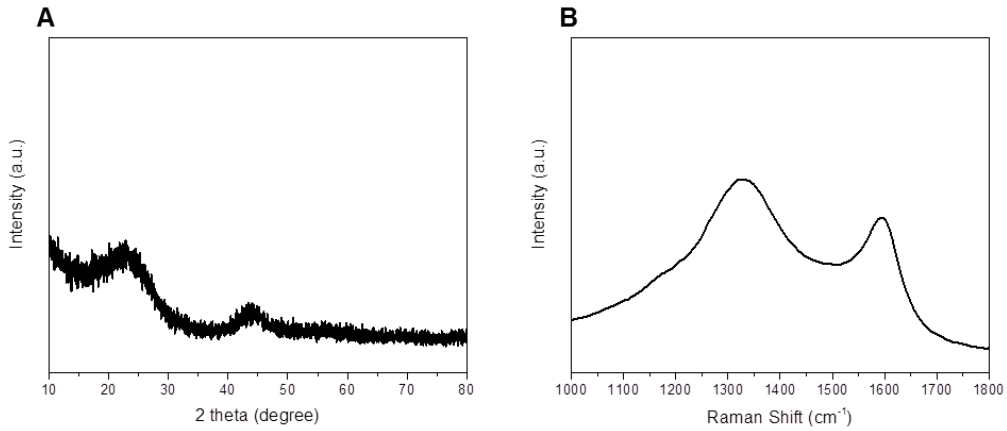

Figure 31. Chemical structure of MC. (A) XRD pattern of MC. (B) Raman spectra of MC. D/G ratio of MC was 1.30.

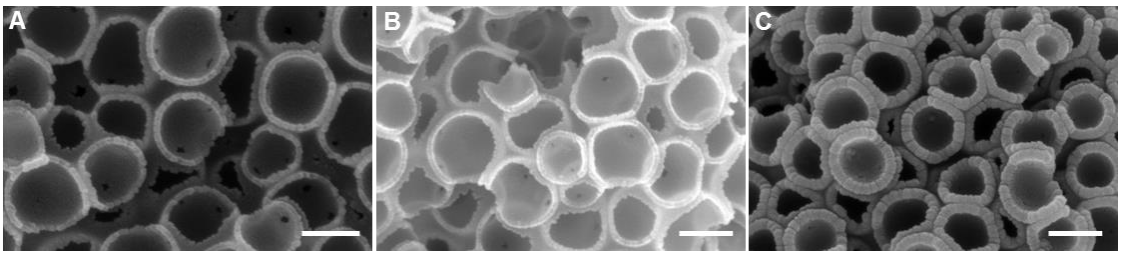

Figure 32. Morphologies of SMC series. SEM images of (A) SMC600, (B) SMC1200, and (C) SMC2000. Scale bar = 200 nm for A, and 250 nm for B and C.

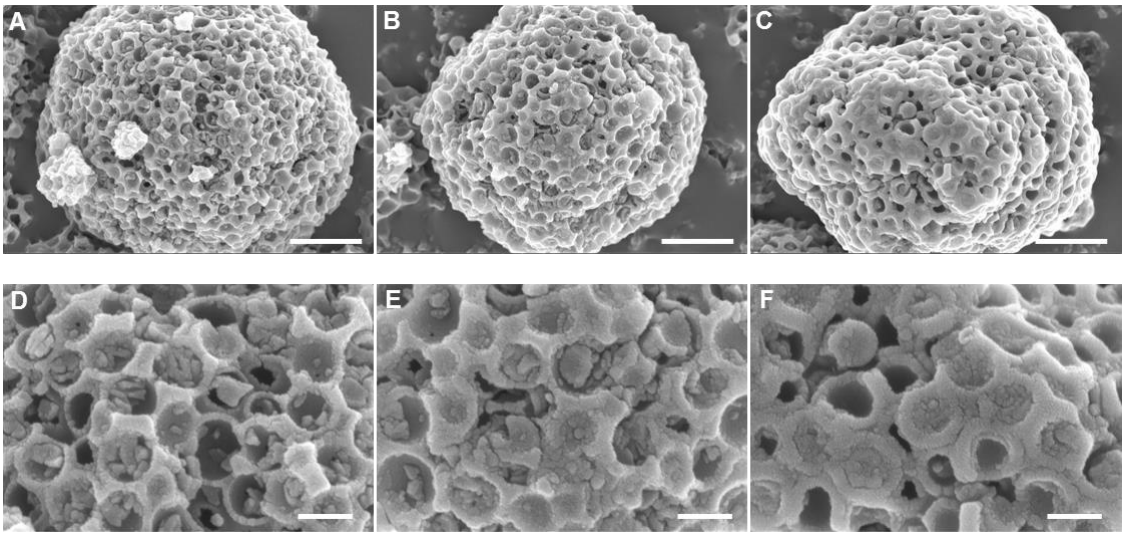

Figure 33. Morphologies of CSMC series. SEM images of (A) CSMC600, (B) CSMC1200, and (C) CSMC2000. Magnified SEM images of (D) CSMC600, (E) CSMC1200, and (F) CSMC2000. Scale bar = 1 μm for A, B, and C, 250 nm for D, E, and F.

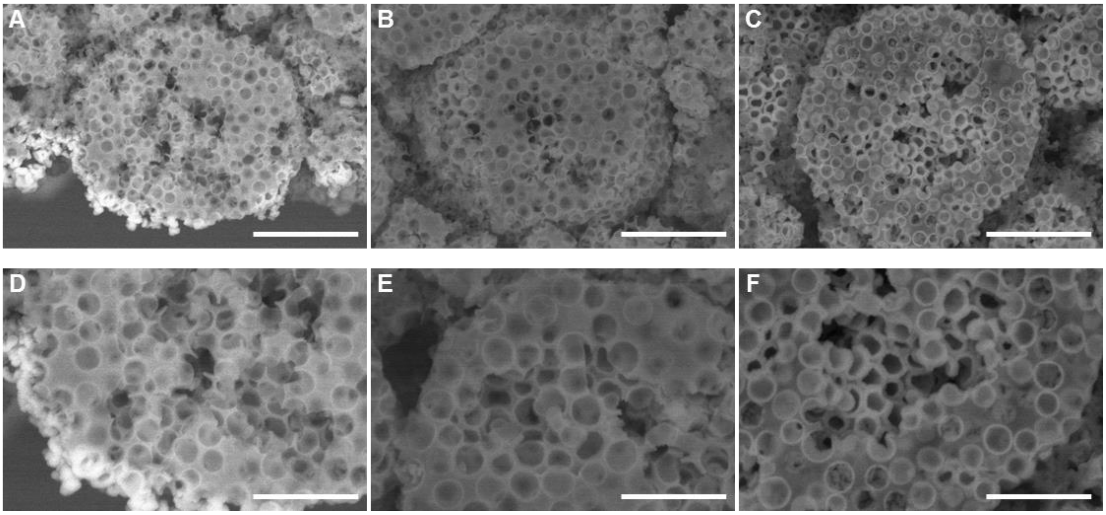

Figure 34. Inner morphologies of CSMC series. Cross-sectional BSE images of (A) CSMC600, (B) CSMC1200, and (C) CSMC2000. Magnified cross-sectional BSE images of (D) CSMC600, (E) CSMC1200, and (F) CSMC2000. Scale bar = 2 μm for A, B, and C, and 1 μm for D, E, and F.

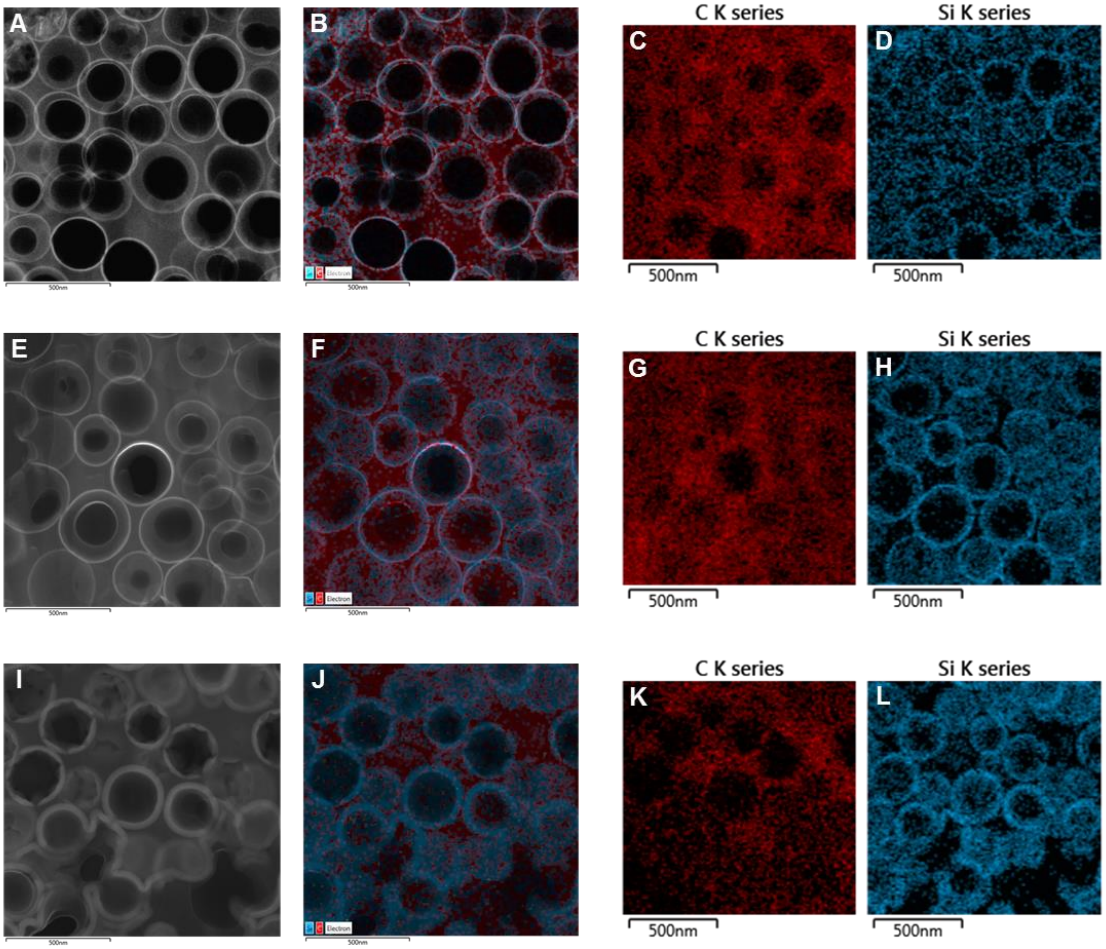

Figure 35. STEM EDS mapping of CSMC series. (A-D) CSMC600, (E-H) CSMC1200, and (I-L) CSMC2000. (red dot = carbon, blue dot = silicon)

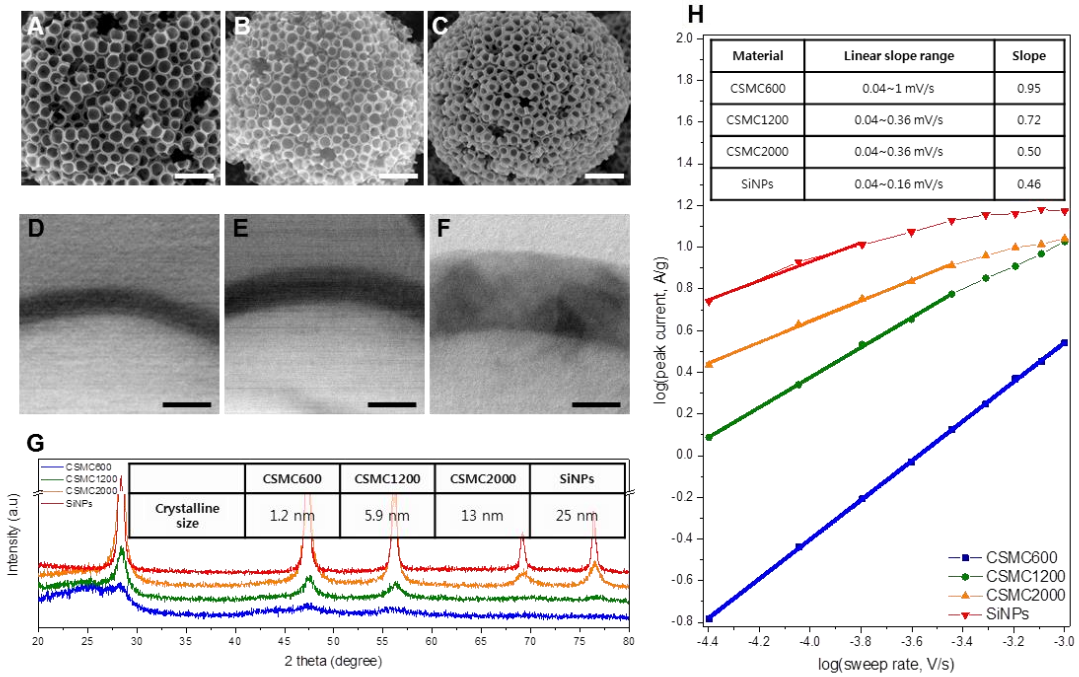

Figure 36. Revealing the Si size in CSMC series and relative properties. SEM images of (A) SMC600, (B) SMC1200, and (C) SMC2000. Magnified STEM images of Si nanolayers in (D) CSMC600, (E) CSMC1200, and (F) CSMC2000. (G) XRD patterns of CSMC series and SiNPs with crystalline size table derived by Scherrer equation. (H) Plot [log(peak current) versus log(sweep rate)] determining b-values in $i = av^b$ from anodic peak current, inset table shows slop of the graph and linear slope lange. Scale bar = 1 μm for A, B, and C, 20 nm for D, E, and F.

Figure 36 summarized different properties depending on the Si ratio. The weight ratio of C and Si was individually measured by element analyzer (EA) and inductively coupled plasma atomic emission spectroscopy (ICP-AES). C weight ratios by EA were 74, 65, and 44wt% and Si weight ratios by ICP-AES were 24, 39, and 48wt% for CSMC600, CSMC1200, and CSMC2000 respectively. There were inevitable errors measuring exact ratio of C and Si because of SiO2 formation and minor amount of insolubility of Si. Moreover, the expected reversible capacities of CSMC series based on C and Si ratio of EA and ICP-AES were variant from the real values. These differences in the reversible capacities according to Si ratios will be mentioned in later sections. The SEM images of SMCs showed the different Si layer thickness (figure 36A-C, 32). These differences were more clearly measured in the STEM images (figure 36D-F). The Si layer thicknesses of CSMC600, CSMC1200, and CSMC2000 were about 9, 15, and 31 nm. The crystalline size of samples was calculated using XRD data with the Scherrer equation. The calculated crystalline sizes of CSMC600, CSMC1200, and CSMC2000 were 1.2, 5.9, and 13 nm (figure 36G).

To figure out redox mechanisms of CSMC series, we conducted modified linear sweep voltammetry (C-LSV) for each sample (The detailed method was shown in supplementary information). The C-LSV method was typical constant current-constant voltage mode for lithiation and linear sweep voltammetry for delithiation with various sweep rate (0.04-1 mV/s). In figure 37, we compared conventional CV and our C-LSV methods with Si nanoparticles (SiNPs) anode. In gravimetric capacity vs. voltage plot, CV methods exhibited 151~578 mAh/g and C-LSV exhibited 3086~3485 mAh/g depending on the voltage scan rate. It means anodic/cathodic peak current analysis of CV just manifested electrochemical properties of partially lithiated Si anode rather than fully lithiated state. The reason of this large difference is on slight gap between reduction potentials of [$xLi^+ + e^- + Si \rightarrow Li_xSi$] and [$Li^+ + e^- \rightarrow Li$ (s)] [18]. To induce fully lithiation into Si with CV method, the cut-off voltage should be below 0 V. However, then Li plating reaction would also be activated under 0 V. Thus, constant voltage mode after constant current charging is usually used to fully charge Si-based or graphite anode rather than lower cut-off potential under 0 V[103]. Therefore, this new method; C-LSV could provide more precise electrochemical information of fully charged anode materials while it is limited in anodic peak current analysis.

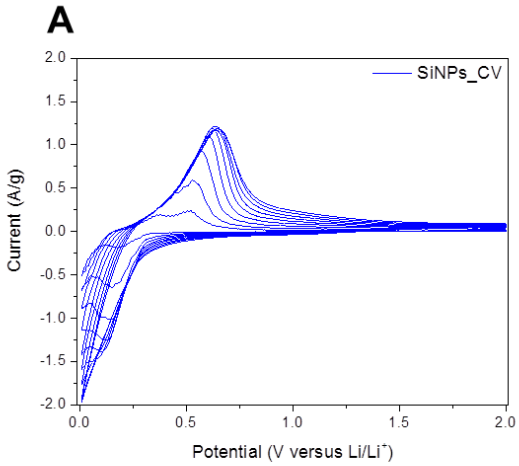

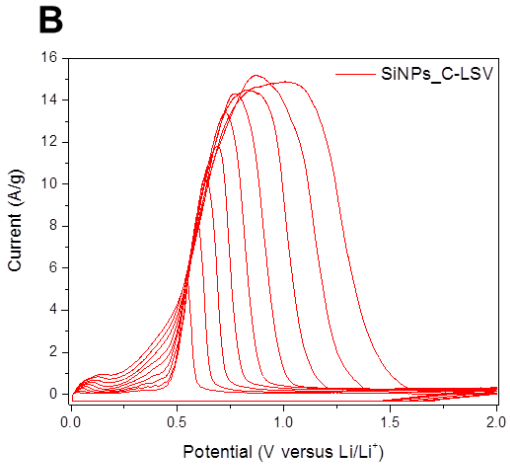

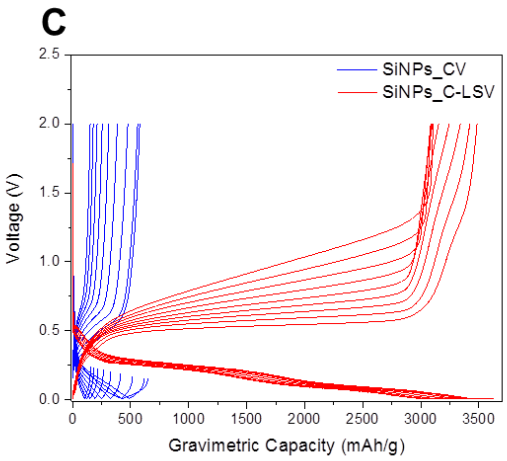

D

	CV		C-LSV	
Scan rate (mV/s)	Discharge Q (mAh/g)	CE (%)	Discharge Q (mAh/g)	CE (%)
0.04	578	89.3	3485	96.2
0.09	561	91.1	3423	95.1
0.16	475	92.4	3340	94.0
0.25	386	93.8	3246	93.1
0.36	313	95.3	3154	92.8
0.49	255	96.5	3100	93.7
0.64	211	97.3	3086	94.7
0.81	178	97.8	3090	95.3
1	151	98.2	3106	95.8

Figure 37. Comparison between conventional CV and C-LSV method with SiNPs electrode. (A) Conventional CV with scan rate of 0.04-1 mV/s. (B) C-LSV with scan rate of 0.04-1 mV/s. (C) Voltage profiles of CV and C-LSV at various scan rate. (D) Discharge capacities and coulombic efficiencies of CV and C-LSV depending on scan rates.

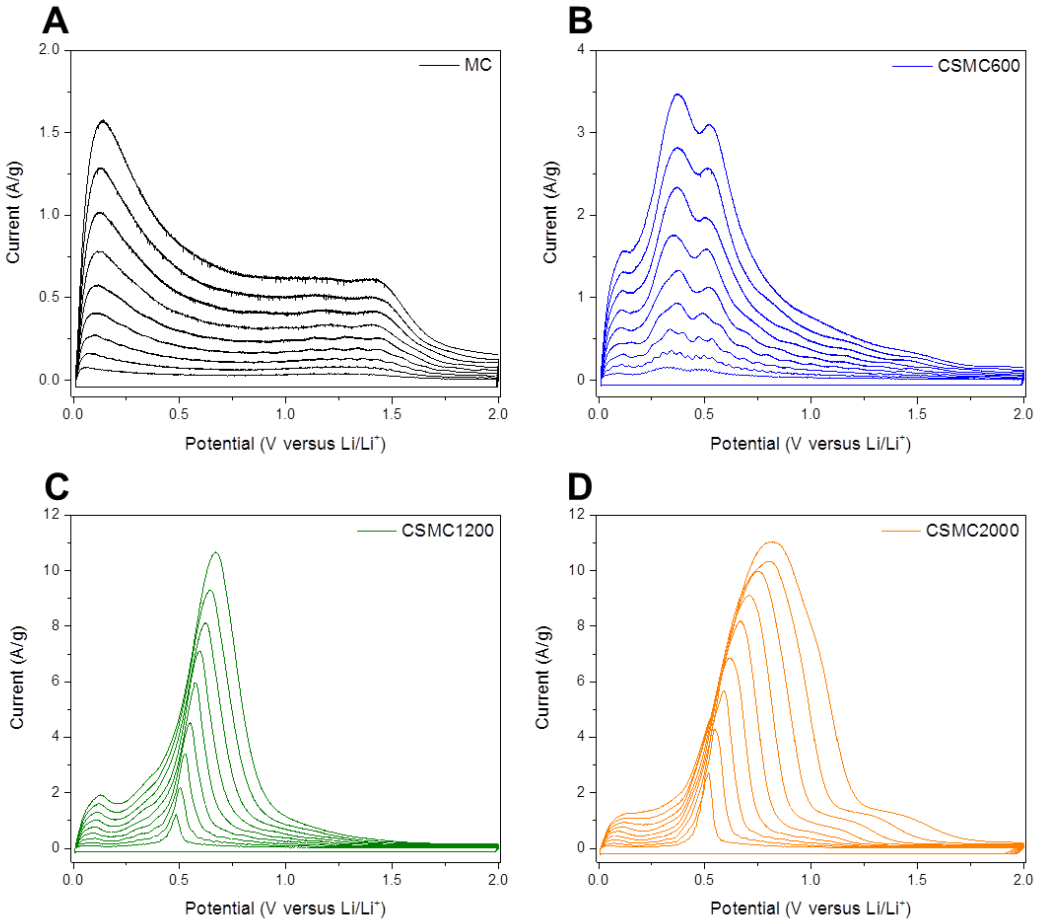

Figure 38. Comparison of C-LSVs for MC and CSMC series. C-LCVs of (A) MC, (B) CSMC600, (C) CSMC1200, and (D) CSMC2000 with scan rate of 0.04-1 mV/s. Slope of MC at plot log(sweep rate) vs. log(i_{peak}) was 0.93 for 0.04-1 mV/s.

The C-LSV results of MC, and CSMC series electrodes were shown in figure 38. We plotted the log (sweep rate) vs. log (peak current) graph according to literature examining pseucapacitive behaviors (figure 36H) [121]. Slopes of the graph were 0.93, 0.95, 0.72, 0.50, and 0.46 for MC, CSMC600, CSMC1200, CSMC2000 and SiNPs respectively (figure 36H, 37, 38). If slope is 1, its redox mechanism is capacitor behavior and if slope is 0.5, then its redox mechanism is battery behavior[122]. Thus, reaction mechanisms of MC and CSMC600 electrodes were close to capacitor behavior, those of CSMC2000 and SiNPs electrodes were close to battery behavior, and that of CSMC1200 electrode was intermediate property between capacitor and battery. As decreasing the diffusion length, pseudocapacitive properties gradually appeared in CSMC series electrodes. Capacitive contribution could be quantified via the relationship between current and sweep rate at a fixed potential; $i=k_1v+k_2v^{(1/2)}$ [123]. The calculated capacitive contributions of MC, CSMC600, CSMC1200, and CSMC2000 electrodes were 84, 88, 55, and 33% respectively at 0.04 mV/s of sweep rate (figure 39A and 38, 40) and that of SiNPs electrodes was 15% (figure 41). Figure 39B represented gravimetric capacities derived by two different mechanisms, capacitive and diffusion controlled. The capacities induced by capacitive effect of MC, CSMC600, CSMC1200, and CSMC2000 were 365, 585, 687, and 665 mAh/g and that of SiNPs was 511 mAh/g (figure 39B and 37, 10). It undoubtedly revealed reaction mechanism of Li ion insertion/extraction on surface and near-surface of Si materials was pseudocapacitive behavior and consequently the thinner Si nanolayer showed the higher capacitive contribution in total capacities. Another pseudocapacitive evidence of Si nanolayer was disappearance of plateau at voltage profiles (figure 39C) [121]. As the Si nanolayer became thinner (from CSMC2000 to CSMC600), the 0.1 V charge and 0.44 V discharge plateau gradually disappeared.

The reversible capacities of MC, CSMC600, CSMC1200, and CSMC2000 were 441, 623, 1215, and 2002 mAh/g at 0.1C formation (figure 40, 41, 42). The reversible capacities of CSMCs were not well reconciled with the calculated capacities from EA and ICP-AES results (figure 43). The real capacities were mostly lower than the calculated capacities and the difference was larger as Si nanolayer thickness decrease. It is mainly caused by native SiO2 layer, deactivated capacity of MC and nanosizing effect. Typically, Si nanostructures contains 2.0~3.4 nm of native SiO2 layer. 2.0~3.4 nm is about 22~38% of Si nanolayer thickness in CSMC600. In contrast, it is about 6~11% of Si nanolayer thickness in CSMC2000. Although native SiO2 layer was not significant amount changing gravimetric capacities in Si nanostructure > 50 nm, it was substantial amount changing gravimetric capacities tendency depending on Si thickness of CSMC structures (< 31 nm).

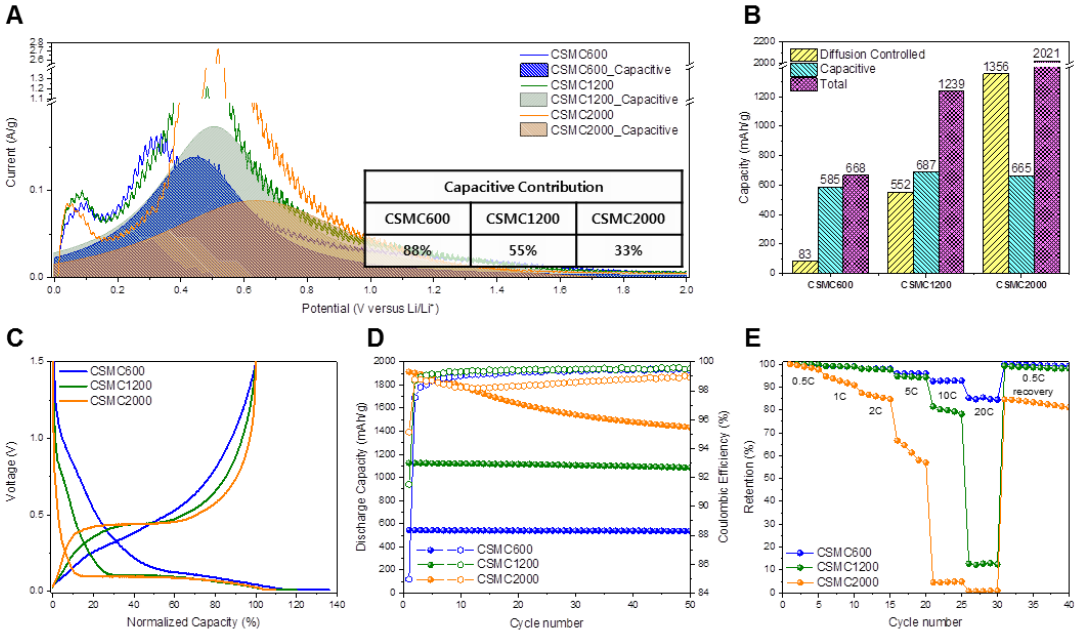

Figure 39. Electrochemical characterization of CSMC series. (A) anodic current of CSMC series with capacitive contribution at 0.04 mV/s. Inset table shows capacitive contributions at total capacities. (B) Diffusion controlled, capacitive, and total capacities of CSMC series. (C) Formation voltage profiles of CSMC series with normalized capacities. (D) 0.5C cycle test of CSMC series. (E) Discharge rate test of CSMC series from 0.5C to 20C.

The initial coulombic efficiencies (ICEs) were 48.6% (MC) 73.5% (CSMC600), 83.3% (CSMC1200), and 91.2% (CSMC2000) (figure 40, 12). Exceptional increase of ICE after C and Si coating was induced by deactivated surface reaction of MC [124]. Subsequent 0.5C cycling test showed stable charge and discharge reaction of CSMC600 and CSMC1200. The retentions at 50th cycle were 98.6% (CSMC600), 96.5% (CSMC1200), 74.9% (CSMC2000), and 54.7% (SiNPs) (figure 39D and 41). To investigate rate performance, we conducted various discharge C-rate cycling (from 0.5C to 20C) with fixed 0.5C charge rate (figure 39E). CSMC600 electrode maintained over 80% of reversible capacity even at 20C and CSMC1200 electrode maintained almost 80% of reversible capacity at 10C. The rate test with same C-rates of charge/discharge was also conducted (figure 44). The results of CSMC600 and CSMC1200 were superior to previous publications of Si based anode (table 1) [35,67,125-127]. For full cell test, lithium cobalt oxide (LCO) cathode was used and the 100th cycle retention of LCO-CSMC1200 full cell was 73% (figure 45).

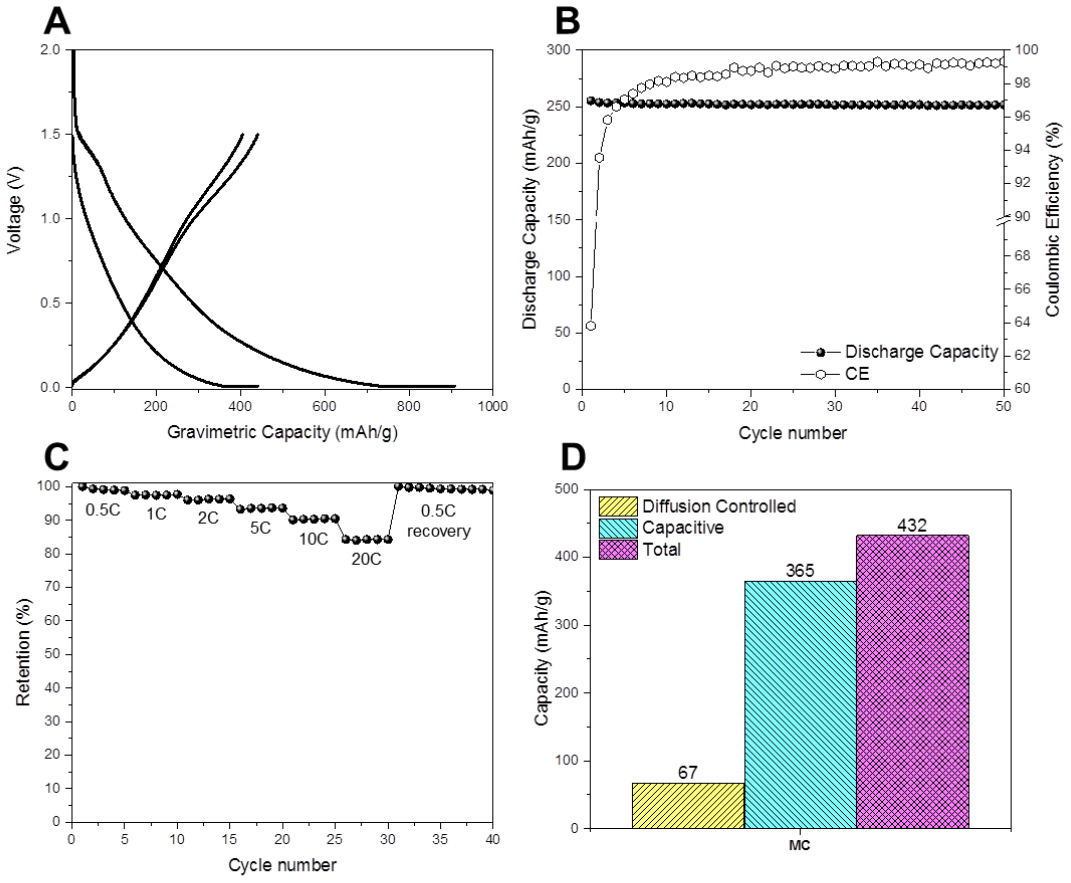

E

Material	1st Charge Q (mAh/g)	1st Discharge Q (mAh/g)	1st CE (%)	2nd Charge Q (mAh/g)	2nd Discharge Q (mAh/g)	2nd CE (%)
MC	908	441	48.6	441	405	91.8

Figure 40. Electrochemical characterization of MC. (A) Formation voltage profiles of MC, (B) Cycle performance of MC, (C) Discharge rate performance of MC, and (D) Diffusion controlled, capacitive, and total capacities of MC. (E) Summary of charge and discharge capacities and CE for MC electrode at formation.

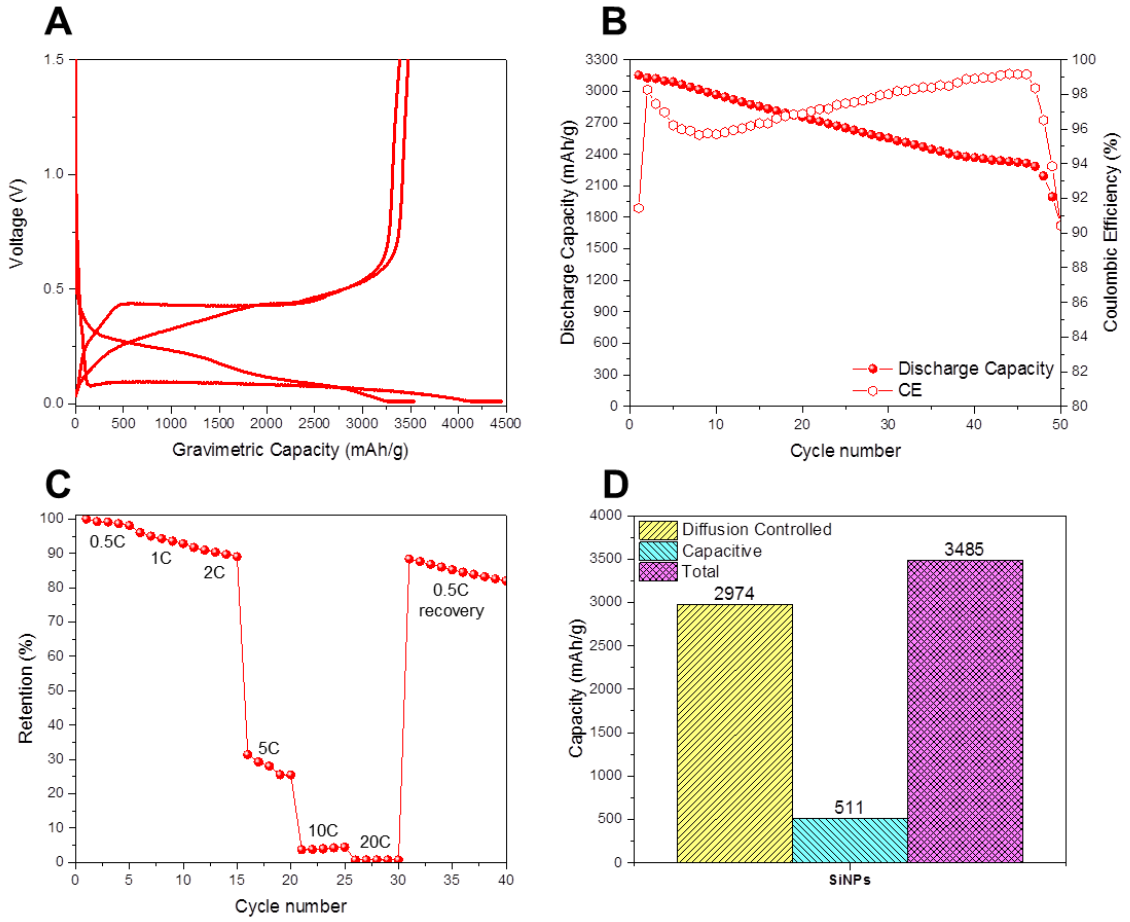

E

Material	1st Charge Q (mAh/g)	1st Discharge Q (mAh/g)	1st CE (%)	2nd Charge Q (mAh/g)	2nd Discharge Q (mAh/g)	2nd CE (%)
SiNPs	4454	3476	78.0	3540	3389	95.7

Figure 41. Electrochemical characterization of SiNPs. (A) Formation voltage profiles of SiNPs, (B) Cycle performance of SiNPs, (C) Discharge rate performance of SiNPs, and (D) Diffusion controlled, capacitive, and total capacities of SiNPs. (E) Summary of charge and discharge capacities and CE for SiNPs electrode at formation.

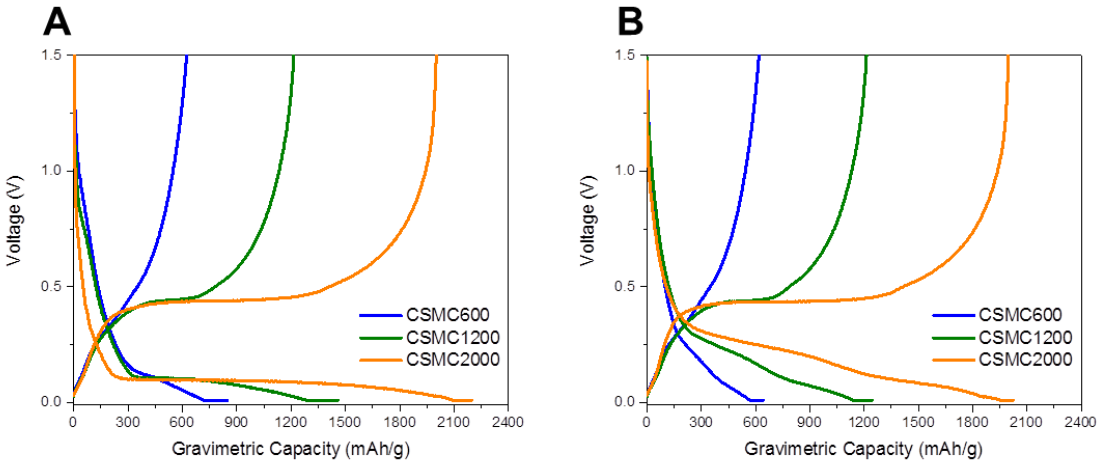

C

Material	1st Charge Q (mAh/g)	1st Discharge Q (mAh/g)	1st CE (%)
CSMC600	848	623	73.5
CSMC1200	1459	1215	83.3
CSMC2000	2196	2002	91.2

D

Material	2nd Charge Q (mAh/g)	2nd Discharge Q (mAh/g)	2nd CE (%)
CSMC600	644	618	96.0
CSMC1200	1243	1213	97.6
CSMC2000	2025	1998	98.7

Figure 42. Formation voltage profiles of CSMC series. (A) first formation, and (B) second formation. (C) Summary of charge and discharge capacities and CE for CSMC series electrodes at the first formation. (D) Summary of charge and discharge capacities and CE for CSMC series electrodes at the second formation.

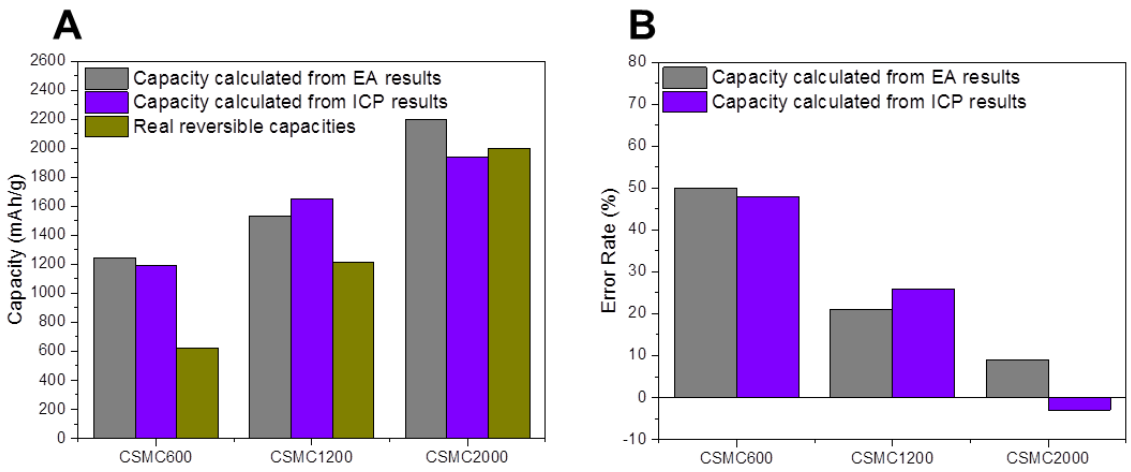

Figure 43. Atomic ratio comparison from EA and ICP. (A) Capacities of CSMC series calculated from EA and ICP, (B) Error rate of calculated capacities from EA and ICP.

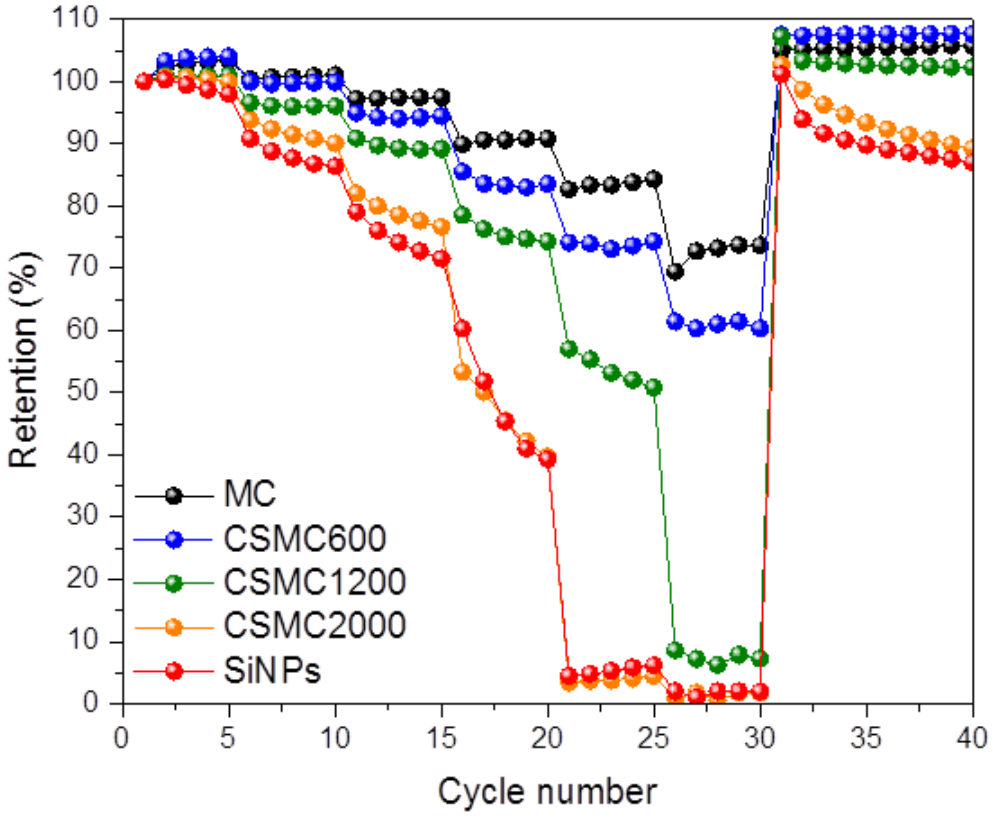

Figure 44. Comparison of CSMC series at same charge/discharge rate test.

Materials	Carbon in electrode composition	Reversible capacity (Current)	ICE	Retention at High rate charge (Current)	Refer
CSMC600	Super P (10 wt%)	623 mAh/g (0.1C) 545 mAh/g (0.5C)	73.5%	73% (10C), 61% (20C)	This work
CSMC1200	Super P (10 wt%)	1215 mAh/g (0.1C) 1125 mAh/g (0.5C)	83.3%	75% (5C), 53% (10C)	
CSMC2000	Super P (10 wt%)	2002 mAh/g (0.1C) 1914 mAh/g (0.5C)	91.2%	79% (2C), 46% (5C)	
Graphene-SiO_x	No additional Carbon	716.2 mAh/g (0.1C)	99.8% (Prelithiation)	33.6% (10C)	Nature Communicationsvolume 8, Article number: 1561 (2017)
Si-edge-plane-activated graphite	Carbon black (1 wt%)	525 mAh/g (0.1C)	93.8%	20% (3C)	Nature Communicationsvolume 8, Article number: 812 (2017)
Mesoporous Amorphous Silicon	Acetylene black (25 wt%)	1679 mAh/g (500 mAh/g;≒ 0.3C)	64.6%	781 mAh/g;≒ 47% (5 A/g;≒ 3C)	Angew. Chem. Int. Ed. 2016, 55, 14063–14066
Si embedded graphite	Super P (1 wt%)	517 mAh/g (0.1C)	92%	40~50% (5C)	Nature Energy volume 1, Article number: 16113 (2016)
SiNPs-Backboned-Graphene	No additional Carbon	2699 mAh/g (0.56 A/g; 0.2C)	92.5	1148 mAh/g;≒ 43% (28A/g; 10C)	*ACS Nano*, 2014, 8 (8), pp 8591–8599

Table 1. Rate capabilities comparison with CSMC series and previous papers

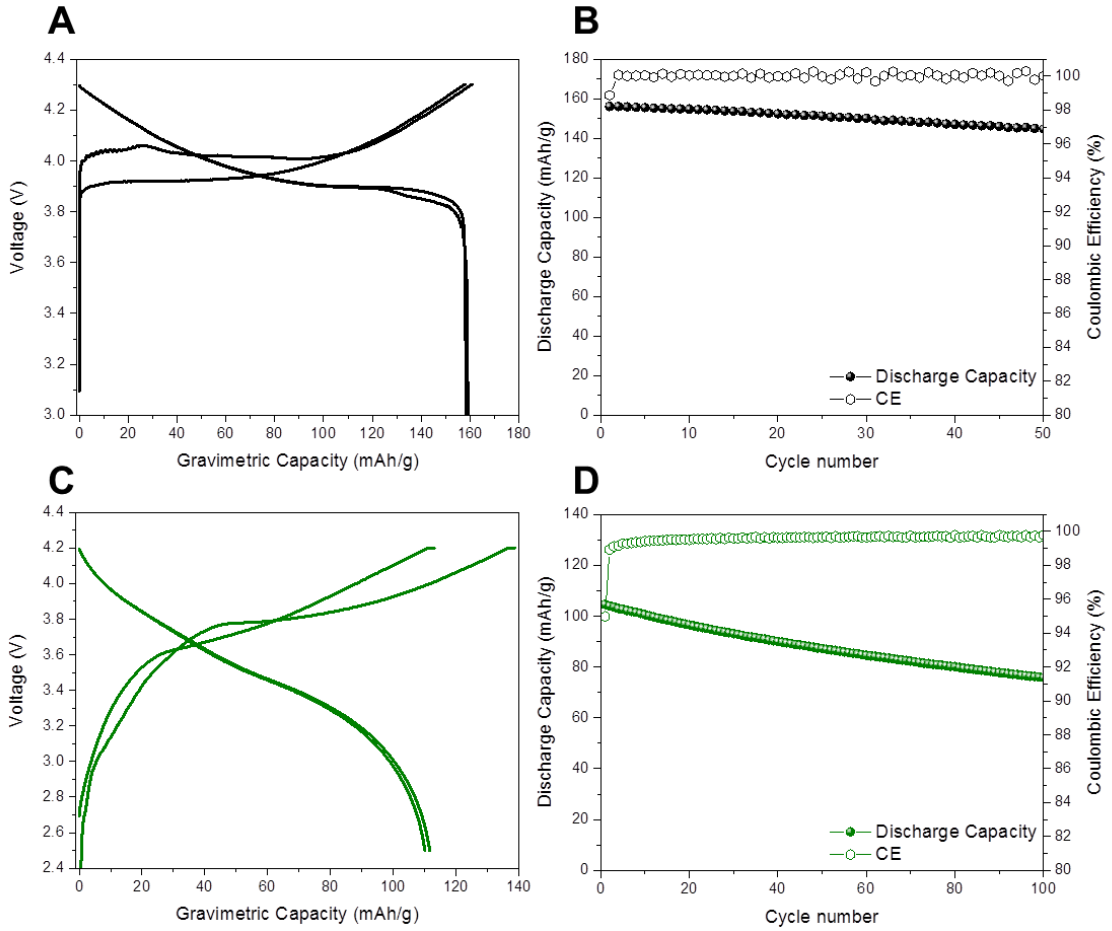

Material	1st Charge Q (mAh/g)	1st Discharge Q (mAh/g)	1st CE (%)	2nd Charge Q (mAh/g)	2nd Discharge Q (mAh/g)	2nd CE (%)
LCO	161	159	98.8	158	158	100
LCO CSMC1200 (Full cell)	139	112	80.6	113	110	97.3

Figure 45. Full cell test with lithium cobalt oxide (LCO) and CSMC1200. (A) formation voltage profiles of LCO (B) half cell 0.5C cycle test of LCO (C) formation voltage profiles of LCO-CSMC1200 full cell (D) full cell 0.5C cycle test.

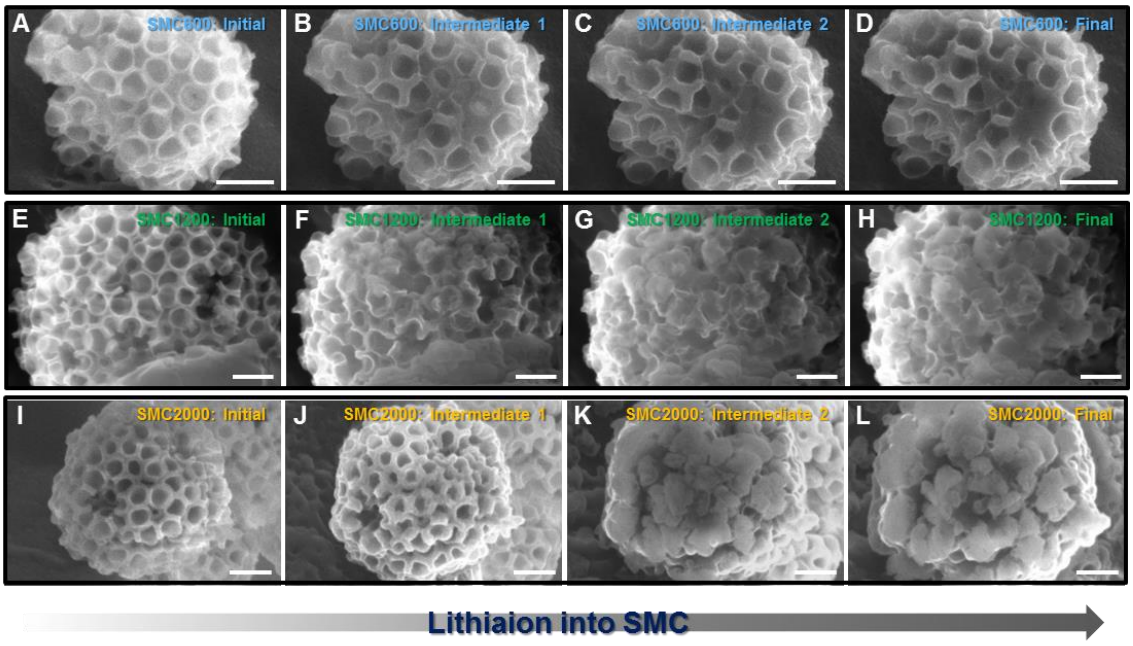

Figure 46. *In situ* SEM analysis of SMC series during lithiation. SEM images from time-lapse *in situ* SEM video of (A-D) SMC600 (supplementary movie 1), (E-H) SMC1200 (supplementary movie 2), and (I-L) SMC 2000 (supplementary movie 3). Initial state was right after contact between Si and Li. Final state was that there wasn't no further reactions. Intermediate 1, 2 were captured between initial and final state. Scale bar = 500 nm for (A-L)

To verify roles of void space in SMC, in situ SEM was carried out. Driving force of lithiation into Si was spontaneous alloying reaction between Li and Si [119,120]. The in situ set up was simply composed with two tips of nanomanipulators; one was for sample and the other was for lithium metal. Right after direct contact between Li and Si, Si expansion started. Depending on the particle size and Si nanolayer thickness, reaction time took about 30~120 minutes. The contact was maintained until there was no volume change of sample (detailed in situ method was described in supplementary information). Figure 46A-D showed in situ lithiation of SMC600. Even after full lithiation, void space of SMC600 was not completely filled. The void space of SMC1200 was almost filled in fully lithiated state; however there wasn't size change in particle scale (Figure 46E-H). In contrast, SMC2000 showed significant volume expansion (figure 46). Expanded Si nanolayer of SMC2000 induced diameter change of particle; from 2.08 to 2.60 μm. The SMC structure could accommodate the Si volume expansion up to ~1200 mAh/g, while > 2000 mAh/g materials suffer significant volume expansion, which is fading reason of cycling.

3.4 Conclusion

In conclusion, we developed unique cage structure of CSMC series for lithium batteries anode materials. CSMCs were composed with micron carbon cage, ultrathin Si nanolayer, and outmost wrapping carbon layer. CSMCs were divided into CSMC600, CSMC1200, and CSMC2000 depending on the gravimetric capacities. For the first time, pseudocapacitive properties of Si anode was investigated. 9 nm Si nanolayer showed 88% of pseudocapacitive capacity and pseudocapacitive ratio was decreased as Si nanolayer thickness increased. The rate capabilities of CSMC600 and CSMC1200 were exceptionally improved compared to previous works. The expansion accommodating role of void space in CSMC series was investigated via in situ SEM characterization. CSMC600 and CSMC1200 showed no volume change in particle scales although CSMC2000 showed 25% of length expansion. Our designed Si-C composite has advantages of high rate capability and volume expansion alleviating structure. Moreover according to kinds of applications, gravimetric capacities of CSMCs could be controlled. We believe these approaches might be immense support to develop higher energy and power LIBs.

Chapter 4

Challenges facing anode materials for lithium ion batteries

The application range of LIBs keeps growing. Every electronics which need electrical energy are adopting and trying to adopt LIBs because of its superior energy and power density compared to any other type of batteries. Currently most critical issue in usage of LIBs is electrical vehicles[128,129]. Several automobile companies declared to produce electrical vehicles adopting LIBs and many people look forward to the future that vehicle smoke will be disappeared. However, energy and power density of LIBs should be improved to totally replace the internal combustion engine locomotives and there will be also unexpected obstacles. In this context, here I summarized possible challenges facing anode materials of LIBs for future.

Electrochemical performance

First of all, electrochemical performance of anode materials should be improved. To increase electrical vehicles mileage with once charging, energy density of anode materials should be increased. However, if energy density of anode materials is increased by using Si materials, then cycle life of the anode will be dramatically decreased in current state. In other words, on the first day of using an electrical car, we can go from Seoul to Busan, but if we leave Busan again on the second day after fully charging of the electrical car, we could only go to Daejeon rather than Seoul. If so, then no one would want to use the electrical car. Therefore, the higher energy density of anode materials should be developed maintaining the cycle retention. In addition, among previous publications, many reports couldn't satisfy the commercial electrode conditions; high loading and density. The current state of high areal and volumetric capacities with graphite anode is ~3.0 mAh/cm^2 and ~550 mAh/cm^3 [28]. The reason why Si material is developing exceeds the current anode state of graphite anode. Hence, electrode test conditions of Si anode should be over ~3.0 mAh/cm^2 and ~550 mAh/cm^3. The developed Si anode which was testified with lower electrode condition compared to those has just little academic value and doesn't bring industrial advancement. In summary, the goals of electrochemical performance in Si dominant anode are surpass the areal and volumetric capacities of graphite anode and maintain its high capacities for long-term life.

Cost

It is not easy to expect production cost of Si anode materials because the cost of materials processing is larger than the cost of raw materials compared to graphite anode or cathode materials. In case of graphite anode, the post-treatment process of the raw material is simple. In case of cathode materials (lithium transition metal oxide), large scale production method (ex. co-precipitation) was already developed [9]. In contrast, Si raw materials need relatively complex processing to alleviate its intrinsic volume expansion properties. For example, bulk Si needs high energy ball-milling process to reduce particle size from micron to nano. To utilize silane CVD method, safe gas cabinet and scrubber system should be installed. To utilize melt spinning method, high temperature devices higher than the melting point of Si (1414 ℃) are needed. In this context, cost aspect as well as electrochemical performance should be considered for commercial usage of Si dominant anode materials and researchers should try to develop economical process for Si anode.

Sustainability

Suppose that electrochemical performance and cost problems of Si dominant anode are solved. Then, it will be faced the sustainability issue of already produced anode materials (graphite anode). In other words, recycling of produced anode materials should be considered. Actually, methods for recycling cathode materials (lithium transition metal oxide) are already being studied [130-132]. The cathode material extracted from the waste battery can be dissolved in an acidic solution and then extracted again as a raw material for cathode. This recycling is possible because the development of the cathode materials is conducted with compositional difference of the transition metal. For example, the cobalt precursor extracted from wasted conventional lithium cobalt oxide could be used for development of $LiNi_xCo_yMn_zO_2$ materials. In contrast, recycling of graphite anode is not simple because carbon is different from silicon. However, because graphite has high electronic conductivity, it might be utilized as coating materials or carbon additives. From this point of view, current research state on graphite anode recycling is very minor and many studies about that should be carried out from now on.

References

1 Bruce, P. G., Scrosati, B. & Tarascon, J. M. Nanomaterials for rechargeable lithium batteries. *Angewandte Chemie-International Edition* **47**, 2930-2946, doi:10.1002/anie.200702505 (2008).

2 Goodenough, J. B. & Kim, Y. Challenges for Rechargeable Li Batteries. *Chemistry of Materials* **22**, 587-603, doi:10.1021/cm901452z (2010).

3 Tarascon, J. M. & Armand, M. Issues and challenges facing rechargeable lithium batteries. *Nature* **414**, 359-367, doi:10.1038/35104644 (2001).

4 Cheng, F. Y. & Chen, J. Metal-air batteries: from oxygen reduction electrochemistry to cathode catalysts. *Chemical Society Reviews* **41**, 2172-2192, doi:10.1039/c1cs15228a (2012).

5 Kundu, D., Talaie, E., Duffort, V. & Nazar, L. F. The Emerging Chemistry of Sodium Ion Batteries for Electrochemical Energy Storage. *Angewandte Chemie-International Edition* **54**, 3431-3448, doi:10.1002/anie.201410376 (2015).

6 Lee, J. S. *et al.* Metal-Air Batteries with High Energy Density: Li-Air versus Zn-Air. *Advanced Energy Materials* **1**, 34-50, doi:10.1002/aenm.201000010 (2011).

7 Pan, H. L., Hu, Y. S. & Chen, L. Q. Room-temperature stationary sodium-ion batteries for large-scale electric energy storage. *Energy & Environmental Science* **6**, 2338-2360, doi:10.1039/c3ee40847g (2013).

8 Yabuuchi, N., Kubota, K., Dahbi, M. & Komaba, S. Research Development on Sodium-Ion Batteries. *Chemical Reviews* **114**, 11636-11682, doi:10.1021/cr500192f (2014).

9 Kim, J. *et al.* Prospect and Reality of Ni-Rich Cathode for Commercialization. *Advanced Energy Materials* **8**, doi:10.1002/aenm.201702028 (2018).

10 Zheng, J. M. *et al.* Li- and Mn-Rich Cathode Materials: Challenges to Commercialization. *Advanced Energy Materials* **7**, doi:10.1002/aenm.201601284 (2017).

11 Bruce, P. G., Freunberger, S. A., Hardwick, L. J. & Tarascon, J. M. Li-O-2 and Li-S batteries with high energy storage. *Nature Materials* **11**, 19-29, doi:10.1038/nmat3191 (2012).

12 Manthiram, A., Fu, Y. Z., Chung, S. H., Zu, C. X. & Su, Y. S. Rechargeable Lithium-Sulfur Batteries. *Chemical Reviews* **114**, 11751-11787, doi:10.1021/cr500062v (2014).

13 Yang, Y., Zheng, G. Y. & Cui, Y. Nanostructured sulfur cathodes. *Chemical Society Reviews* **42**, 3018-3032, doi:10.1039/c2cs35256g (2013).

14 Yin, Y. X., Xin, S., Guo, Y. G. & Wan, L. J. Lithium-Sulfur Batteries: Electrochemistry, Materials, and Prospects. *Angewandte Chemie-International Edition* **52**, 13186-13200, doi:10.1002/anie.201304762 (2013).

15 Goodenough, J. B. & Park, K. S. The Li-Ion Rechargeable Battery: A Perspective. *Journal of the American Chemical Society* **135**, 1167-1176, doi:10.1021/ja3091438 (2013).

16 Lee, S. M., Kang, D. S. & Roh, J. S. Bulk graphite: materials and manufacturing process. *Carbon Letters* **16**, 135-146, doi:10.5714/cl.2015.16.3.135 (2015).

17 Obrovac, M. N. & Chevrier, V. L. Alloy Negative Electrodes for Li-Ion Batteries. *Chemical Reviews* **114**, 11444-11502, doi:10.1021/cr500207g (2014).

18 Wu, H. & Cui, Y. Designing nanostructured Si anodes for high energy lithium ion batteries. *Nano Today* **7**, 414-429, doi:10.1016/j.nantod.2012.08.004 (2012).

19 Zhang, W. J. A review of the electrochemical performance of alloy anodes for lithium-ion batteries. *Journal of Power Sources* **196**, 13-24,

doi:10.1016/j.jpowsour.2010.07.020 (2011).

20 Chae, S., Ko, M., Kim, K., Ahn, K. & Cho, J. Confronting Issues of the Practical Implementation of Si Anode in High-Energy Lithium-Ion Batteries. *Joule* **1**, 47-60, doi:10.1016/j.joule.2017.07.006 (2017).

21 Chen, T., Wu, J., Zhang, Q. L. & Su, X. Recent advancement of SiOx, based anodes for lithium-ion batteries. *Journal of Power Sources* **363**, 126-144, doi:10.1016/j.jpowsour.2017.07.073 (2017).

22 Liu, X. *et al.* SiOx (0 < x <= 2) Based Anode Materials for Lithium-Ion Batteries. *Progress in Chemistry* **27**, 336-348, doi:10.7536/pc141010 (2015).

23 Chen, Y., Qian, J. F., Cao, Y. L., Yang, H. X. & Ai, X. P. Green Synthesis and Stable Li-Storage Performance of FeSi2/Si@C Nanocomposite for Lithium-Ion Batteries. *Acs Applied Materials & Interfaces* **4**, 3753-3758, doi:10.1021/am300952b (2012).

24 Dong, H., Ai, X. P. & Yang, H. X. Carbon/Ba-Fe-Si alloy composite as high capacity anode materials for Li-ion batteries. *Electrochemistry Communications* **5**, 952-957, doi:10.1016/j.elecom.2003.09.004 (2003).

25 Lee, H. Y. & Lee, S. M. Graphite-FeSi alloy composites as anode materials for rechargeable lithium batteries. *Journal of Power Sources* **112**, 649-654, doi:10.1016/s0378-7753(02)00461-5 (2002).

26 Piao, T., Park, S. M., Doh, C. H. & Moon, S. I. Intercalation of lithium ions into graphite electrodes studied by AC impedance measurements. *Journal of the Electrochemical Society* **146**, 2794-2798, doi:10.1149/1.1392010 (1999).

27 Ding, N. *et al.* Determination of the diffusion coefficient of lithium ions in nano-Si. *Solid State Ionics* **180**, 222-225, doi:10.1016/j.ssi.2008.12.015 (2009).

28 Son, I. H. *et al.* Silicon carbide-free graphene growth on silicon for lithium-ion

battery with high volumetric energy density. *Nature Communications* **6**, doi:10.1038/ncomms8393 (2015).

29 Wang, H. *et al.* A reversible dendrite-free high-areal-capacity lithium metal electrode. *Nature Communications* **8**, doi:10.1038/ncomms15106 (2017).

30 Liang, Z. *et al.* Composite lithium metal anode by melt infusion of lithium into a 3D conducting scaffold with lithiophilic coating. *Proceedings of the National Academy of Sciences of the United States of America* **113**, 2862-2867, doi:10.1073/pnas.1518188113 (2016).

31 Lin, D. C., Liu, Y. Y. & Cui, Y. Reviving the lithium metal anode for high-energy batteries. *Nature Nanotechnology* **12**, 194-206, doi:10.1038/nnano.2017.16 (2017).

32 Kubota, Y., Escano, M. C. S., Nakanishi, H. & Kasai, H. Crystal and electronic structure of Li15Si4. *Journal of Applied Physics* **102**, doi:10.1063/1.2775999 (2007).

33 Jin, Y. *et al.* Self-healing SEI enables full-cell cycling of a silicon-majority anode with a coulombic efficiency exceeding 99.9%. *Energy & Environmental Science* **10**, 580-592, doi:10.1039/c6ee02685k (2017).

34 Li, X. L. *et al.* Design of porous Si/C-graphite electrodes with long cycle stability and controlled swelling. *Energy & Environmental Science* **10**, 1427-1434, doi:10.1039/c7ee00838d (2017).

35 Ko, M. *et al.* Scalable synthesis of silicon-nanolayer-embedded graphite for high-energy lithium-ion batteries. *Nature Energy* **1**, doi:10.1038/nenergy.2016.113 (2016).

36 Li, Y. Z. *et al.* Growth of conformal graphene cages on micrometre-sized silicon particles as stable battery anodes. *Nature Energy* **1**, doi:10.1038/nenergy.2015.29

(2016).

37 Chen, D., Indris, S., Schulz, M., Gamer, B. & Monig, R. In situ scanning electron microscopy on lithium-ion battery electrodes using an ionic liquid. *Journal of Power Sources* **196**, 6382-6387, doi:10.1016/j.jpowsour.2011.04.009 (2011).

38 Liu, X. H. & Huang, J. Y. In situ TEM electrochemistry of anode materials in lithium ion batteries. *Energy & Environmental Science* **4**, 3844-3860, doi:10.1039/c1ee01918j (2011).

39 Son, Y., Sung, J., Son, Y. & Cho, J. Recent progress of analysis techniques for silicon-based anode of lithium-ion batteries. *Current Opinion in Electrochemistry* **6**, 77-83, doi:10.1016/j.coelec.2017.10.005 (2017).

40 Dupre, N. *et al.* Multiprobe Study of the Solid Electrolyte Interphase on Silicon-Based Electrodes in Full-Cell Configuration. *Chemistry of Materials* **28**, 2557-2572, doi:10.1021/acs.chemmater.5b04461 (2016).

41 McDowell, M. T., Lee, S. W., Nix, W. D. & Cui, Y. 25th Anniversary Article: Understanding the Lithiation of Silicon and Other Alloying Anodes for Lithium-Ion Batteries. *Advanced Materials* **25**, 4966-4984, doi:10.1002/adma.201301795 (2013).

42 McDowell, M. T. *et al.* In Situ TEM of Two-Phase Lithiation of Amorphous Silicon Nanospheres. *Nano Letters* **13**, 758-764, doi:10.1021/nl3044508 (2013).

43 Lee, S. W. *et al.* Kinetics and fracture resistance of lithiated silicon nanostructure pairs controlled by their mechanical interaction. *Nature Communications* **6**, doi:10.1038/ncomms8533 (2015).

44 Wang, X. J. *et al.* High damage tolerance of electrochemically lithiated silicon. *Nature Communications* **6**, doi:10.1038/ncomms9417 (2015).

45 Pietsch, P. *et al.* Quantifying microstructural dynamics and electrochemical activity of graphite and silicon-graphite lithium ion battery anodes. *Nature Communications* **7**, doi:10.1038/ncomms12909 (2016).

46 An, S. J. *et al.* The state of understanding of the lithium-ion-battery graphite solid electrolyte interphase (SEI) and its relationship to formation cycling. *Carbon* **105**, 52-76, doi:10.1016/j.carbon.2016.04.008 (2016).

47 Xiong, D. J., Burns, J. C., Smith, A. J., Sinha, N. & Dahn, J. R. A High Precision Study of the Effect of Vinylene Carbonate (VC) Additive in Li/Graphite Cells. *Journal of the Electrochemical Society* **158**, A1431-A1435, doi:10.1149/2.100112jes (2011).

48 Kumar, R. *et al.* In Situ and Operando Investigations of Failure Mechanisms of the Solid Electrolyte Interphase on Silicon Electrodes. *Acs Energy Letters* **1**, 689-697, doi:10.1021/acsenergylett.6b00284 (2016).

49 Michan, A. L. *et al.* Solid Electrolyte Interphase Growth and Capacity Loss in Silicon Electrodes. *Journal of the American Chemical Society* **138**, 7918-7931, doi:10.1021/jacs.6b02882 (2016).

50 Boniface, M. *et al.* Nanoscale Chemical Evolution of Silicon Negative Electrodes Characterized by Low-Loss STEM-EELS. *Nano Letters* **16**, 7381-7388, doi:10.1021/acs.nanolett.6b02883 (2016).

51 Hatchard, T. D. & Dahn, J. R. In situ XRD and electrochemical study of the reaction of lithium with amorphous silicon. *Journal of the Electrochemical Society* **151**, A838-A842, doi:10.1149/1.1739217 (2004).

52 Ogata, K. *et al.* Revealing lithium-silicide phase transformations in nano-structured silicon-based lithium ion batteries via in situ NMR spectroscopy. *Nature Communications* **5**, doi:10.1038/ncomms4217 (2014).

53 Seidlhofer, B. K. *et al.* Lithiation of Crystalline Silicon As Analyzed by Operando Neutron Reflectivity. *Acs Nano* **10**, 7458-7466, doi:10.1021/acsnano.6b02032 (2016).

54 Graetz, J., Ahn, C. C., Yazami, R. & Fultz, B. Highly reversible lithium storage in nanostructured silicon. *Electrochemical and Solid State Letters* **6**, A194-A197, doi:10.1149/1.1596917 (2003).

55 Chan, C. K. *et al.* High-performance lithium battery anodes using silicon nanowires. *Nature Nanotechnology* **3**, 31-35, doi:10.1038/nnano.2007.411 (2008).

56 Guo, Y. G., Hu, J. S. & Wan, L. J. Nanostructured materials for electrochemical energy conversion and storage devices. *Advanced Materials* **20**, 2878-2887, doi:10.1002/adma.200800627 (2008).

57 Manthiram, A. Materials Challenges and Opportunities of Lithium Ion Batteries. *Journal of Physical Chemistry Letters* **2**, 176-184, doi:10.1021/jz1015422 (2011).

58 Cui, L. F., Ruffo, R., Chan, C. K., Peng, H. L. & Cui, Y. Crystalline-Amorphous Core-Shell Silicon Nanowires for High Capacity and High Current Battery Electrodes. *Nano Letters* **9**, 491-495, doi:10.1021/nl8036323 (2009).

59 Cui, L. F., Yang, Y., Hsu, C. M. & Cui, Y. Carbon-Silicon Core-Shell Nanowires as High Capacity Electrode for Lithium Ion Batteries. *Nano Letters* **9**, 3370-3374, doi:10.1021/nl901670t (2009).

60 Liu, N. *et al.* A Yolk-Shell Design for Stabilized and Scalable Li-Ion Battery Alloy Anodes. *Nano Letters* **12**, 3315-3321, doi:10.1021/nl3014814 (2012).

61 Park, M. H. *et al.* Silicon Nanotube Battery Anodes. *Nano Letters* **9**, 3844-3847, doi:10.1021/nl902058c (2009).

62 Yao, Y. *et al.* Interconnected Silicon Hollow Nanospheres for Lithium-Ion Battery Anodes with Long Cycle Life. *Nano Letters* **11**, 2949-2954, doi:10.1021/nl201470j (2011).

63 Magasinski, A. *et al.* High-performance lithium-ion anodes using a hierarchical bottom-up approach. *Nature Materials* **9**, 353-358, doi:10.1038/nmat2725 (2010).

64 Liu, N. *et al.* A pomegranate-inspired nanoscale design for large-volume-change lithium battery anodes. *Nature Nanotechnology* **9**, 187-192, doi:10.1038/nnano.2014.6 (2014).

65 Wu, H. *et al.* Stable cycling of double-walled silicon nanotube battery anodes through solid-electrolyte interphase control. *Nature Nanotechnology* **7**, 309-314, doi:10.1038/nnano.2012.35 (2012).

66 Chae, S. *et al.* Micron-sized Fe-Cu-Si ternary composite anodes for high energy Li-ion batteries. *Energy & Environmental Science* **9**, 1251-1257, doi:10.1039/c6ee00023a (2016).

67 Kim, N., Chae, S., Ma, J., Ko, M. & Cho, J. Fast-charging high-energy lithium-ion batteries via implantation of amorphous silicon nanolayer in edge-plane activated graphite anodes. *Nature Communications* **8**, doi:10.1038/s41467-017-00973-y (2017).

68 Aravindan, V., Lee, Y. S. & Madhavi, S. Research Progress on Negative Electrodes for Practical Li-Ion Batteries: Beyond Carbonaceous Anodes. *Advanced Energy Materials* **5**, doi:10.1002/aenm.201402225 (2015).

69 Zhao, Y. *et al.* Recent Developments and Understanding of Novel Mixed Transition-Metal Oxides as Anodes in Lithium Ion Batteries. *Advanced Energy Materials* **6**, doi:10.1002/aenm.201502175 (2016).

70 Tang, Y. X., Zhang, Y. Y., Li, W. L., Ma, B. & Chen, X. D. Rational material design for ultrafast rechargeable lithium-ion batteries. *Chemical Society Reviews* **44**, 5926-5940, doi:10.1039/c4cs00442f (2015).

71 Roy, P. & Srivastava, S. K. Nanostructured anode materials for lithium ion batteries. *Journal of Materials Chemistry A* **3**, 2454-2484, doi:10.1039/c4ta04980b (2015).

72 Larcher, D. & Tarascon, J. M. Towards greener and more sustainable batteries for electrical energy storage. *Nature Chemistry* **7**, 19-29, doi:10.1038/nchem.2085 (2015).

73 Sun, Y. M., Liu, N. A. & Cui, Y. Promises and challenges of nanomaterials for lithium-based rechargeable batteries. *Nature Energy* **1**, doi:10.1038/nenergy.2016.71 (2016).

74 Choi, J. W. & Aurbach, D. Promise and reality of post-lithium-ion batteries with high energy densities. *Nature Reviews Materials* **1**, doi:10.1038/natrevmats.2016.13 (2016).

75 Ko, M., Chae, S. & Cho, J. Challenges in Accommodating Volume Change of Si Anodes for Li-Ion Batteries. *Chemelectrochem* **2**, 1645-1651, doi:10.1002/celc.201500254 (2015).

76 Du, F. H., Wang, K. X. & Chen, J. S. Strategies to succeed in improving the lithium-ion storage properties of silicon nanomaterials. *Journal of Materials Chemistry A* **4**, 32-50, doi:10.1039/c5ta06962a (2016).

77 Lee, J. K., Oh, C., Kim, N., Hwang, J. Y. & Sun, Y. K. Rational design of silicon-based composites for high-energy storage devices. *Journal of Materials Chemistry A* **4**, 5366-5384, doi:10.1039/c6ta00265j (2016).

78 Luo, F. *et al.* Review-Nano-Silicon/Carbon Composite Anode Materials Towards

Practical Application for Next Generation Li-Ion Batteries. *Journal of the Electrochemical Society* **162**, A2509-A2528, doi:10.1149/2.0131514jes (2015).

79 Casimir, A. *et al.* Silicon-based anodes for lithium-ion batteries: Effectiveness of materials synthesis and electrode preparation. *Nano Energy* **27**, 359-376, doi:10.1016/j.nanoen.2016.07.023 (2016).

80 Zuo, X. X., Zhu, J., Muller-Buschbaum, P. & Cheng, Y. J. Silicon based lithium-ion battery anodes: A chronicle perspective review. *Nano Energy* **31**, 113-143, doi:10.1016/j.nanoen.2016.11.013 (2017).

81 Ashuri, M., He, Q. R. & Shaw, L. L. Silicon as a potential anode material for Li-ion batteries: where size, geometry and structure matter. *Nanoscale* **8**, 74-103, doi:10.1039/c5nr05116a (2016).

82 Liu, L. H., Lyu, J., Li, T. H. & Zhao, T. K. Well-constructed silicon-based materials as high-performance lithium-ion battery anodes. *Nanoscale* **8**, 701-722, doi:10.1039/c5nr06278k (2016).

83 Jin, N. *et al.* Silicon-Based Anode Materials for Lithium-Ion Batteries. *Progress in Chemistry* **27**, 1275-1290, doi:10.7536/pc150155 (2015).

84 Ko, M., Oh, P., Chae, S., Cho, W. & Cho, J. Considering Critical Factors of Li-rich Cathode and Si Anode Materials for Practical Li-ion Cell Applications. *Small* **11**, 4058-4073, doi:10.1002/smll.201500474 (2015).

85 Yin, J. B., Deng, T. S. & Zhang, G. M. Preparation and size control of highly monodisperse vinyl functionalized silica spheres. *Applied Surface Science* **258**, 1910-1914, doi:10.1016/j.apsusc.2011.06.155 (2012).

86 Ma, J. J., Liu, Q. M., Chen, D. D., Wen, S. & Wang, T. H. Synthesis and characterisation of pore-expanded mesoporous silica materials. *Micro & Nano Letters* **10**, 140-144, doi:10.1049/mnl.2014.0413 (2015).

87 Tabuchi, H., Urita, K. & Moriguchi, I. Effect of Carbon Nanospace on Charge Discharge Properties of Si and SiOx, Nanoparticles-Embedded Nanoporous Carbons. *Bulletin of the Chemical Society of Japan* **88**, 1378-1384, doi:10.1246/bcsj.20150228 (2015).

88 Ma, X. M. *et al.* Mesoporous size controllable carbon microspheres and their electrochemical performances for supercapacitor electrodes. *Journal of Materials Chemistry A* **2**, 8407-8415, doi:10.1039/c4ta00333k (2014).

89 Zhao, L. L., Liu, H. R., Wang, F. W. & Zeng, L. Design of yolk-shell Fe3O4@PMAA composite microspheres for adsorption of metal ions and pH-controlled drug delivery. *Journal of Materials Chemistry A* **2**, 7065-7074, doi:10.1039/c4ta00976b (2014).

90 Choi, K. I., Lee, W., Lee, S. H. & Lim, C. Synthesis of hierarchical hollow electrospun TiO2 nanofibers. *Materials Letters* **158**, 36-39, doi:10.1016/j.matlet.2015.05.066 (2015).

91 Niu, J. *et al.* Towards Si@SiO2 core-shell, yolk-shell, and SiO2 hollow structures from Si nanoparticles through a self-templated etching-deposition process. *Rsc Advances* **4**, 29435-29438, doi:10.1039/c4ra02236j (2014).

92 Waldbott, G. L. & Lee, J. R. TOXICITY FROM REPEATED LOW-GRADE EXPOSURE TO HYDROGEN-FLUORIDE - CASE-REPORT. *Clinical Toxicology* **13**, 391-402, doi:10.3109/15563657808988247 (1978).

93 Dalbey, W. *et al.* Acute effects of 10-minute exposure to hydrogen fluoride in rats and derivation of a short-term exposure limit for humans. *Regulatory Toxicology and Pharmacology* **27**, 207-216, doi:10.1006/rtph.1998.1203 (1998).

94 Yang, X. Q. *et al.* Structural studies of the new carbon-coated silicon anode materials using synchrotron-based in situ XRD. *Electrochemistry*

Communications **4**, 893-897, doi:10.1016/s1388-2481(02)00483-6 (2002).

95 Li, H. *et al.* The crystal structural evolution of nano-Si anode caused by lithium insertion and extraction at room temperature. *Solid State Ionics* **135**, 181-191, doi:10.1016/s0167-2738(00)00362-3 (2000).

96 Muniz, F. T. L., Miranda, M. A. R., dos Santos, C. M. & Sasaki, J. M. The Scherrer equation and the dynamical theory of X-ray diffraction. *Acta Crystallographica a-Foundation and Advances* **72**, 385-390, doi:10.1107/s205327331600365x (2016).

97 He, K., Chen, N. F., Wang, C. J., Wei, L. S. & Chen, J. K. Method for Determining Crystal Grain Size by X-Ray Diffraction. *Crystal Research and Technology* **53**, doi:10.1002/crat.201700157 (2018).

98 Tan, C. C., Lu, L., See, A. & Chan, L. Effect of degree of amorphization of Si on the formation of titanium silicide. *Journal of Applied Physics* **91**, 2842-2846, doi:10.1063/1.1432768 (2002).

99 Yom, J. H., Cho, S. M. & Yoon, W. Y. Kinetic analysis of irreversible behavior in silicon monoxide anode by GITT, EIS and CV for lithium ion battery. *Abstracts of Papers of the American Chemical Society* **253** (2017).

100 Rui, X. H., Yesibolati, N., Li, S. R., Yuan, C. C. & Chen, C. H. Determination of the chemical diffusion coefficient of Li+ in intercalation-type Li3V2(PO4)(3) anode material. *Solid State Ionics* **187**, 58-63, doi:10.1016/j.ssi.2011.02.013 (2011).

101 Chen, Y. L. *et al.* Hollow core-shell structured silicon@carbon nanoparticles embed in carbon nanofibers as binder-free anodes for lithium-ion batteries. *Journal of Power Sources* **342**, 467-475, doi:10.1016/j.jpowsour.2016.12.089 (2017).

102 Sun, W. *et al.* Embedding nano-silicon in graphene nanosheets by plasma assisted milling for high capacity anode materials in lithium ion batteries. *Journal of Power Sources* **268**, 610-618, doi:10.1016/j.jpowsour.2014.06.039 (2014).

103 Waldmann, T., Kasper, M. & Wohlfahrt-Mehrens, M. Optimization of Charging Strategy by Prevention of Lithium Deposition on Anodes in high-energy Lithium-ion Batteries - Electrochemical Experiments. *Electrochimica Acta* **178**, 525-532, doi:10.1016/j.electacta.2015.08.056 (2015).

104 Eddahech, A., Briat, O. & Vinassa, J. M. Determination of lithium-ion battery state-of-health based on constant-voltage charge phase. *Journal of Power Sources* **258**, 218-227, doi:10.1016/j.jpowsour.2014.02.020 (2014).

105 Zhang, S. S., Xu, K. & Jow, T. R. Study of the charging process of a LiCoO(2)-based Li-ion battery. *Journal of Power Sources* **160**, 1349-1354, doi:10.1016/j.jpowsour.2006.02.087 (2006).

106 Gogotsi, Y. & Penner, R. M. Energy Storage in Nanomaterials - Capacitive Pseudocapacitive, or Battery-like? *Acs Nano* **12**, 2081-2083, doi:10.1021/acsnano.8b01914 (2018).

107 Ghodbane, O., Pascal, J. L. & Favier, F. Microstructural Effects on Charge-Storage Properties in MnO2-Based Electrochemical Supercapacitors. *Acs Applied Materials & Interfaces* **1**, 1130-1139, doi:10.1021/am900094e (2009).

108 Lukatskaya, M. R. *et al.* Cation Intercalation and High Volumetric Capacitance of Two-Dimensional Titanium Carbide. *Science* **341**, 1502-1505, doi:10.1126/science.1241488 (2013).

109 Zheng, J. P., Cygan, P. J. & Jow, T. R. HYDROUS RUTHENIUM OXIDE AS AN ELECTRODE MATERIAL FOR ELECTROCHEMICAL CAPACITORS.

Journal of the Electrochemical Society **142**, 2699-2703, doi:10.1149/1.2050077 (1995).

110 Augustyn, V. *et al.* High-rate electrochemical energy storage through Li+ intercalation pseudocapacitance. *Nature Materials* **12**, 518-522, doi:10.1038/nmat3601 (2013).

111 Jiang, Y. Z. *et al.* Ultrafast, Highly Reversible, and Cycle-Stable Lithium Storage Boosted by Pseudocapacitance in Sn-Based Alloying Anodes. *Advanced Materials* **29**, doi:10.1002/adma.201606499 (2017).

112 Lesel, B. K., Ko, J. S., Dunn, B. & Tolbert, S. H. Mesoporous LixMn2O4 Thin Film Cathodes for Lithium-Ion Pseudocapacitors. *Acs Nano* **10**, 7572-7581, doi:10.1021/acsnano.6b02608 (2016).

113 Yuan, T. Z., Jiang, Y. Z., Wang, Q. T., Pan, B. & Yan, M. Pseudocapacitance-Enhanced High-Rate Lithium Storage in "Honeycomb"-like Mn2O3 Anodes. *Chemelectrochem* **4**, 565-569, doi:10.1002/celc.201600588 (2017).

114 Liang, B., Liu, Y. P. & Xu, Y. H. Silicon-based materials as high capacity anodes for next generation lithium ion batteries. *Journal of Power Sources* **267**, 469-490, doi:10.1016/j.jpowsour.2014.05.096 (2014).

115 Ma, D. L., Cao, Z. Y. & Hu, A. M. Si-Based Anode Materials for Li-Ion Batteries: A Mini Review. *Nano-Micro Letters* **6**, 347-358, doi:10.1007/s40820-014-0008-2 (2014).

116 Terranova, M. L., Orlanducci, S., Tamburri, E., Guglielmotti, V. & Rossi, M. Si/C hybrid nanostructures for Li-ion anodes: An overview. *Journal of Power Sources* **246**, 167-177, doi:10.1016/j.jpowsour.2013.07.065 (2014).

117 Zhao, J. *et al.* Metallurgically lithiated SiOx anode with high capacity and ambient air compatibility. *Proceedings of the National Academy of Sciences of*

the United States of America **113**, 7408-7413, doi:10.1073/pnas.1603810113 (2016).

118 Wang, J., Polleux, J., Lim, J. & Dunn, B. Pseudocapacitive contributions to electrochemical energy storage in TiO2 (anatase) nanoparticles. *Journal of Physical Chemistry C* **111**, 14925-14931, doi:10.1021/jp074464w (2007).

119 Choi, Y. S., Byeon, Y. W., Ahn, J. P. & Lee, J. C. Formation of Zintl Ions and Their Configurational Change during Sodiation in Na-Sn Battery. *Nano Letters* **17**, 679-686, doi:10.1021/acs.nanolett.6b03690 (2017).

120 Stournara, M. E., Kumar, R., Qi, Y. & Sheldon, B. W. Ab initio diffuse-interface model for lithiated electrode interface evolution. *Physical Review E* **94**, doi:10.1103/PhysRevE.94.012802 (2016).

121 Augustyn, V., Simon, P. & Dunn, B. Pseudocapacitive oxide materials for high-rate electrochemical energy storage. *Energy & Environmental Science* **7**, 1597-1614, doi:10.1039/c3ee44164d (2014).

122 Lukatskaya, M. R., Dunn, B. & Gogotsi, Y. Multidimensional materials and device architectures for future hybrid energy storage. *Nature Communications* **7**, doi:10.1038/ncomms12647 (2016).

123 Liu, T. C., Pell, W. G., Conway, B. E. & Roberson, S. L. Behavior of molybdenum nitrides as materials for electrochemical capacitors - Comparison with ruthenium oxide. *Journal of the Electrochemical Society* **145**, 1882-1888, doi:10.1149/1.1838571 (1998).

124 Buiel, E. & Dahn, J. R. Li-insertion in hard carbon anode materials for Li-ion batteries. *Electrochimica Acta* **45**, 121-130, doi:10.1016/s0013-4686(99)00198-x (1999).

125 Ko, M., Chae, S., Jeong, S., Oh, P. & Cho, J. Elastic a-Silicon Nanoparticle

Backboned Graphene Hybrid as a Self-Compacting Anode for High-Rate Lithium Ion Batteries. *Acs Nano* **8**, 8591-8599, doi:10.1021/nn503294z (2014).

126 Lin, L. D., Xu, X. N., Chu, C. X., Majeed, M. K. & Yang, J. Mesoporous Amorphous Silicon: A Simple Synthesis of a High-Rate and Long-Life Anode Material for Lithium-Ion Batteries. *Angewandte Chemie-International Edition* **55**, 14063-14066, doi:10.1002/anie.201608146 (2016).

127 Son, I. H. *et al.* Graphene balls for lithium rechargeable batteries with fast charging and high volumetric energy densities. *Nature Communications* **8**, doi:10.1038/s41467-017-01823-7 (2017).

128 Svens, P., Lindstrom, J., Gelin, O., Behm, M. & Lindbergh, G. Novel Field Test Equipment for Lithium-Ion Batteries in Hybrid Electrical Vehicle Applications. *Energies* **4**, 741-757, doi:10.3390/en4050741 (2011).

129 Han, X. B. *et al.* A comparative study of commercial lithium ion battery cycle life in electrical vehicle: Aging mechanism identification. *Journal of Power Sources* **251**, 38-54, doi:10.1016/j.jpowsour.2013.11.029 (2014).

130 Fan, L. B. Recycling and Reuse of Cathode Material of Waste Ternary Lithium-Ion Power Battery. *Agro Food Industry Hi-Tech* **28**, 1543-1547 (2017).

131 Contestabile, M., Panero, S. & Scrosati, B. A laboratory-scale lithium-ion battery recycling process. *Journal of Power Sources* **92**, 65-69, doi:10.1016/s0378-7753(00)00523-1 (2001).

132 Ganter, M. J., Landi, B. J., Babbitt, C. W., Anctil, A. & Gaustad, G. Cathode refunctionalization as a lithium ion battery recycling alternative. *Journal of Power Sources* **256**, 274-280, doi:10.1016/j.jpowsour.2014.01.078 (2014).

* *Chapter 1.4 is reproduced in part with permission of "*Son, Y., Sung, J., Son, Y. & Cho, J. Recent progress of analysis techniques for silicon-based anode of lithium-ion

batteries. *Current Opinion in Electrochemistry* **6**, 77-83, doi:10.1016/j.coelec.2017.10.005 (2017).*". Copyright 2017 Current Opinion in Electrochemistry.*